Preparation and impedance characterization of all-solid-state thin film battery systems

Preparation und Impedanz Charakterisierung von Dünnschicht-Feststoffbatterie Systemen

dem Fachbereich 08 Biologie und Chemie der Justus-Liebig-Universität Giessen

vorgelegte Dissertation zur Erlangung des Grades
Doktor der Naturwissenschaften
- Dr. rer nat. -

eingereicht von
Patrick Schichtel

1. Reviewer/Gutachter Prof. Dr. Jürgen Janek
2. Reviewer/Gutachter Prof. Dr. Bernd Smarsly

Gießen, den 25. Januar 2018

Eidesstattliche Erklärung

Hiermit versichere ich, die vorgelegte Thesis selbstständig und ohne unerlaubte fremde Hilfe und nur mit den Hilfen angefertigt zu haben, die ich in der Thesis angegeben habe. Alle Textstellen, die wörtlich oder sinngemäß aus veröffentlichten Schriften entnommen sind, und alle Angaben die auf mündlichen Auskünften beruhen, sind als solche kenntlich gemacht. Bei den von mir durchgeführten und in der Thesis erwähnten Untersuchungen habe ich die Grundsätze guter wissenschaftlicher Praxis, wie sie in der "Satzung der JustusLiebig-Universität zur Sicherung guter wissenschaftlicher Praxis" niedergelegt sind, eingehalten. Gemäß § 25 Abs. 6 der Allgemeinen Bestimmungen für modularisierte Studiengänge dulde ich eine Überprüfung der Thesis mittels Anti-Plagiatssoftware

Gießen, den 25. Januar 2018

Danksagung

An dieser Stelle möchte ich mich bei allen bedanken, die zum Gelingen dieser Arbeit beigetragen haben, insbesondere

- Herrn Prof. Dr. Jürgen Janek für die Ermöglichung dieser Arbeit.
- Herrn Prof. Dr. Bernd Smarsly für die Zweitbegutachtung der Arbeit.
- Dr. Joachim Sann und Dr. Thomas Leichtweiß für die Betreung während der Arbeit
- Dr. Dominik Weber für die Hilfe und fachliche Diskussion während der Arbeit.
- Dr. Boris Mogwitz für die technische Unterstützung an der PLD-Anlage.
- Dr. Bjoern Luerßen für die Hilfe in allen Dingen in der Promotionszeit und davor.
- Matthias Geiß für seinen Beitrag zu dieser Arbeit durch die Herstellung vieler “LiPON” Schichten.
- Dr. Matthias Elm für die Unterstützung und Hilfe bei der Beurteilung physikalischer Kontaktphänomene.
- allen Mitarbeitern des technischen Personals und der Feinmechanikerwerkstatt ohne die ein Gelingen der Arbeit nicht möglich gewesen wäre.
- allen Mitarbeitern der Arbeitsgruppe für ihre Hilfsbereitschaft und die schöne Zeit.
- meinen Kommilitonen und Bürogenossen für ihre Hilfsbereitschaft bei offenen Fragen.
- meinen Eltern für die Unterstützung meines Studiums.

Contents

1 Inhalt der Arbeit

Innerhalb dieser Arbeit wurde das Verhalten und die Eigenschaften von Festkörperbatterien basierend auf zwei verschiedenen Elektrodenmaterialien untersucht. Zu diesem Zweck wurden Dünnschichtsysteme der relevanten Materialien hergestellt um Modellsysteme für die nähere Untersuchung der materialspezifischen Eigenschaften zu erhalten. Die Charakterisierung der Systeme erfolgte dabei neben den typischen physikalischen und elektrochemischen Methoden im Wesentlichen über Impedanzspektroskopie.

Zunächst wurde in der Arbeit Lithiumtitanat $Li_4Ti_5O_{12}$ untersucht, das aufgrund seiner geringen Volumenausdehnung beim Lithiumein- und -ausbau schon früh als idealer Kandidat für die Anodenseite einer Festkörperbatterie betrachtet wurde. Für dieses Material wird die Herstellung der Schichtsysteme sowie die Optimierung der Herstellungsparameter gezeigt und anschließend auf die speziellen Eigenschaften des Materials innerhalb des Systems eingegangen. Lithiumtitanat zeigt in der Praxis ein deutliches Zweiphasenverhalten wobei sich die Eigenschaften der geladenen und entladenen Phase mitunter stark voneinander unterscheiden. Die wesentlichen Unterschiede zeigen sich hierbei in der ionischen und elektronischen Leitfähigkeit. Die Eigenschaften der beiden Phasen werden in dieser Arbeit anhand der Impedanzspektren des Batteriesystems gezeigt und es werden Rückschlüsse über die Phasenumwandlung des Systems aus diesen Daten gezogen. Dabei wird vor allem diskutiert, ob es sich wirklich um einen Zweiphasenübergang oder eher um einen Übergang über eine feste Lösung handelt.

Neben der Phasenumwandlung des System werden auch weitere Eigenschaften des Systems insbesondere in der Wechselwirkung des Elektrodenmaterials mit dem Elektrolyten und dem Substratmaterial erläutert. Dabei zeigte sich vor allem, dass der Widerstand zwischen Elektrode und Elektrolyt vernachlässigbar ist, jedoch je nach verwendetem Substratmaterial der elektronische Übergang gestört werden kann. Dies liegt in der halbleitenden bis isolierenden Natur des Lithiumtitanates begründet, was im Kontakt zu halbleitenden Materialien zu störenden Raumladungszonen innerhalb des Materials führt. Diese Raumladungszonen liegen auch im Kontakt mit Metallen vor und können bei sehr dünnen Schichten das Zellverhalten stören.

Im zweiten Teil der Arbeit werden ähnliche Untersuchungen an einem zweiten Elektrodenmaterial, dem Lithium-Nickel-Manganoxid durchgeführt. Dieses Material ist aufgrund seiner hohen Arbeitsspannung als Kathodenmaterial interessant. Die Untersuchungen beschäftigen sich dabei im Wesentlichen mit den Problemen bei der Herstellung und Hafteigenschaften des Systems und mit der Beurteilung des Verhaltens an den Grenzfläche. Hierbei wird vor allem der Vergleich zum Lithiumtitanatsystem betrachtet und Gemeinsamkeiten sowie Unterschiede diskutiert. Zudem beschäftigt sich die Arbeit mit der Frage welche Phase des Materials abgeschieden wird und wie sich die Grenzfläche zwischen Kathode und Festelektrolyt in Abhängigkeit des Herstellungsprozesses verhält.

2 Contents of the Thesis

In this thesis the behavior and properties of solid-state batteries based on multiple electrodes are analysed. For this purpose thin film systems of the relevant materials are prepared to achieve model system for more detailed analysis of the material specific properties. The characterisation of the systems is carried out with typical physical and electrochemical methods and especially using impedance spectroscopy.

The first material analysed in this thesis is $Li_4Ti_5O_{12}$ which was recognized early on as an interesting candidate for an anode material for solid-state batteries due to its miniscule volume expansion during lithium insertion and extraction. For this material the preparation of thin film systems and the optimisation of preparation parameter is shown and special properties of the material in the system are discussed. Lithium titanate shows a clear two-phase behavior and the properties of the charged and discharged phase are vastly different. The main difference here is the ionic and electronic conductivity. The properties of the two phases are evaluated using impedance spectroscopy and conclusions about the phase transition are drawn from this data. The main point of discussion is between a phase transition based on a two-phase system or a solid solution system.

Aside from the phase transition other properties of the system like the interaction between electrode and electrolyte are explained. It is shown that the resistance between electrode and electrolyte is miniscule but an additional electronic charge transfer between electrode and substrate material can form under certain circumstances. This phenomenon occurs due to the semiconducting, almost insulating nature of lithium titanate, which leads to extended space charge layers in the material. These space charge layers can also appear in contact with metal substrates and can hinder the cell performance for very thin electrode layers.

In the second part of the thesis similar experiments are performed on another electrode material using lithium nickel manganese oxide. This material is of interest as cathode material due to its high working potential versus lithium metal. The work is mostly focused on the problems in electrode preparation, especially film adhesion, and evaluation of the interface between cathode and electrolyte. The data is interpreted in comparison to the data of lithium titanate and differences and similarities are highlighted. Additional the question of which phase of the material is deposited is exploded and how the interface between cathode and electrolyte changes in dependence of the utilized deposition method.

3 Introduction and Motivation

The current trend in politics and society towards renewable energy sources has caused a renewed interest in the advancement of energy storage for stationary applications as well as for automotive implementations. In addition to that the market for Li-ion batteries for mobile devices remains strong since its initial inception in the 1990s. In the wake of these developments the scientific community has tried to expand the Li-ion battery beyond the traditional materials and concepts towards more promising or cheaper alternatives often regarded as “next generation batteries”. Aside from the economically interesting lithium sulfur battery and the ever promising lithium oxygen battery the concept of the all-solid-state battery has shown remarkable development in the past years. By exchanging the liquid electrolyte used in traditional Li-ion batteries with a solid phase the concept offers in principle a solution to many safety issues arising from flammable electrolytes as well as advantages regarding voltage stability and dendrite suppression. With the application of very thin electrolyte layers additionally the production of very thin and possibly flexible microbatteries for medical or other specific use cases is possible.[1,2]

Despite this promising outlook the production and utilization of all-solid-state cells has extended beyond the realm that is thoroughly understood by the scientific community. For quite some time one of the foremost goals of solid-state battery research was improving the Li-ion conductivity of solid electrolytes. In this regard great progress has been achieved and the conductivity of some solid electrolytes now even surpasses those of liquid electrolytes. The field now focuses more and more on the material interaction and inter-phase transport effects found in all-solid-state batteries. Especially the interaction between solid electrolytes and the various cathode materials is still an active field of research. Additionally, the implementation of lithium metal as anode is typically desired in all-solid-state cells due to the possible increase in energy density, yet again the stability and interactions of lithium metal with solid electrolytes is often problematic.

To study the interface interaction as well as the resistances and problems involved, impedance spectroscopy is a powerful tool since it allows monitoring of all relevant system processes simultaneously and *in situ* without the need of special sample constructions like it would be necessary for *in situ* photoelectron spectroscopy or secondary ion mass spectrometry. The method though relies in practice on empirical comparison and prior knowledge of parts of the system which has not yet been thoroughly established in the all-solid-state battery field (section 8).

This thesis aims to achieve two things: Firstly to thoroughly establish a comprehensive impedance model for an all-solid-state battery based on the rather well understood lithium titanate (LTO) material in order to form a basis for further research and secondly, use this basis to explore the limitations of lithium nickel manganese oxide (LNMO) in the same system to compare both materials in regards of similarities and differences. To achieve this the thesis will initially discuss the steps necessary to prepare functional LTO-based thin film batteries and in the following the impedance model of the resulting batteries will be established and connected to characteristic material properties of the different LTO phases (see section 6, 11). Afterwards, the deposition of the LNMO system similar in construction is discussed and the previously established impedance model is used to probe the interaction of LNMO with the solid electrolyte, the influence of surface coatings, deposition method and dendritic growth in the electrolyte on the battery performance and behavior (section 7, 13).

In this regard thin film systems have always been the primary model system to study interface phenomena due to their defined geometry and interface as well as their generally high surface/bulk ratio. One of the primary electrolytes used for thin film all-solid-state systems is lithium phosphorus oxynitride ("LiPON"; the abbreviation is given in quotation marks to not confuse it with a stoichiometric formula) which can be rather easily deposited via magnetron sputtering.[3] Despite the material being used since the early nineties rather recent studies have shown previously unknown interactions between the material and lithium metal, just to give an example of the partially lacking understanding in this field (see section 4). The other two materials studied in this thesis, lithium titanate (LTO) and lithium nickel manganese oxide (LNMO) are of particular interest due to the miniscule volume expansion LTO offers and the high operating voltage LNMO offers (section 4, 6, 7). LTO is a material employed for quite some time in the community and is rather well understood outside of the solid-state application. It can serve as a type of reference electrode from which the properties and phenomena of the all-solid-state thin film system can be explored. LNMO on the other hand has had some problems in the past when applied in this kind of system and one of the reasons theorized is the large charge transfer resistance between LNMO and "LiPON".

4 The significance of the thesis in the current literature

Some of the materials discussed in this thesis and their application in batteries, for example lithium manganese oxide and its spinel phase as well as lithium titanate (LTO), can be traced to the early works of Goodenough *et al.* as well as Tarascon *et al.*, Ohzuku *et al.* and others.[4–8] They therefore have a long standing history in the battery community and the literature relevant to these materials is quite vast. This section will therefore be focused on giving a literature overview more directly related to those aspects of these materials discussed in this thesis.

Lithium titanate introduced by Ohzuku *et al.*[6] as a zero strain material has since been of interest in the community due to its miniscule volume change during lithium insertion, although the material itself had previously been known.[8–11] Early on it was evidenced through XRD studies by Scharner *et al.* that, despite spinel systems had been known till that point as single phase random insertion materials, lithium titanate was indeed a two phase material as was previously already suggested from electrochemical results from other authors.[6,12] This was further detailed by Wagemaker *et al.*[13,14] and the two phase separation was shown to not be stable at room temperature and instead kinetically induced during cycling. The equilibrium state at room temperature was shown to actually be a solid solution. For liquid systems several aspects of cell behavior for LTO based batteries have since been attributed to and explained by this behavior with the two phase separation generally being the more observed or used explanation.[15–20]

Due to the recently increased interest in solid-state batteries the zero strain properties of LTO are of particular merit in these systems and even more so in thin film applications. For the specific system that is discussed in this thesis, the LTO/“LiPON” system, it is necessary to understand the phase change kinetics and processes of the material since, as will be shown in section 11, the phase change is inseparably connected to the characteristic impedance phenomena observed. Data on this specific system already exist in the literature (Iriyama *et al.*[21] as well as Nakazawa *et al.*[22]). Both of these works are focused on a more general electrochemical characterization of the respective systems measured and do not provide a detailed analysis of material interactions inside the all-solid-state cell. Iriyama *et al.* did argue though that the charge transfer resistance between the two materials is likely very small, which makes LTO even more interesting for impedance studies in all-solid-state cells, especially in comparison to materials with high charge transfer resistances.

Most work regarding lithiation and delithiation of LTO in the literature is done in liquid systems and therefore not directly comparable to the solid-state system.[15,16,23–25] The

behavior in thin solid systems with their specific geometric and kinetic conditions is not explored yet but these parameters are likely relevant for the overall behavior (see section 8).
The impedance characterization in this thesis can be considered closely related to a report of Larfaillou *et al.*[26] that offers a similar approach to a complete analysis of a solid-state system. The authors explored the more common Li/"LiPON"/Lithium cobalt oxide system and arrived at a rather similar data set.

The solid electrolyte used ("LiPON") has – since it was initially introduced by Bates *et al.*[3] – for a long time been assumed to be stable in a wide voltage range.[27] Only rather recently this has been shown to be false.[28–31] The interface degradation that is evidenced in the cited works is typically not directly observed in the impedance data and is often interpreted as simply a charge transfer resistance.[26,32,33] This in and of itself is not directly problematic but it can lead to erroneous assumptions once details of process interactions are discussed. Most of the work regarding "LiPON" is focused on its interaction with a multitude of battery materials and a lesser degree of interest exists in understanding the phase itself or improving its transport properties (which for thin film application is not as necessary). Work regarding the material interface is often either focused on the charge transfer between the electrolyte and other materials[21,32,34–38] or focused on space charge layer phenomena inside the electrolyte itself.[29,39–43]

In this regard, the research field has overlapped with the current developments for lithium nickel manganese oxide (LNMO) in thin film all-solid-state batteries. While for the pure manganese-based spinel data in combination with "LiPON" have already been reported[34,44] the application of the nickel containing analogue is rare due to its often mentioned high charge transfer resistance in contact with "LiPON".[40] An analogue of this system based on iron substitution has been demonstrated by Eftekhari[36] but none of the same problems were mentioned and the material itself is not explored much in literature. As with LTO the works utilizing the material in liquid systems are not comparable to the solid-state environment since the problems and difficulties are vastly different. In the liquid system the main problem of LNMO is the dissolution of manganese species in the liquid electrolyte and the high voltage of the material combined with the electrochemical window of most liquid electrolytes.[45–50]

Functional Li/"LiPON"/$LiNi_{0.5}Mn_{1.5}O_4$ thin film cells are only reported by Yada. *et al.*[40] as well as Li *et al.*[51] and both show somewhat contradicting results. While Yada *et al.* report that the material itself is only usable with surface coatings, Li *et al.* demonstrated that no such coating was necessary to produce highly stable cells. Thai and Lee[52] also suggested that the coating of Yada *et al.* might have a different impact on the interface behavior than the authors expected, for example on the mechanical strain within the cell. No deeper understanding of the problems and differences of the material studied in these works has yet been gained so that the conflicting results between these authors are not yet clearly explained.

This thesis further demonstrates that preparation of functioning battery cells based on the LNMO system is possible, in agreement with Li *et al.* but also demonstrates that results achieved by pulsed laser deposition are in agreement with Yada *et al.*. This suggests that the preparation method likely has an effect on the interface or the system in general and that not yet fully understood phenomena are important for the material compatibility.

In regard to the LTO material the thesis offers insight into the impedance behavior of thin film all-solid-state cells and connects various material interactions to the LTO phase change in dependance of the state of charge. A distinction between the applicable models for phase transition is made and their relevance for the thin film system is evaluated. Furthermore, differences and similarities between the LTO and LNMO system are presented and their significance for the electrochemical behavior of the resulting batteries are discussed.

5 Experimental Setup

5.1 Powder preparation

For the deposition of lithium titanate commercially available powder from Süd-Chemie AG (99.98 %) was used. To prepare the PLD targets the powder was pressed with a diameter of 25 mm and a force of 20 kN for approx. 30 min uniaxially and subsequently for 6 h at 3000 bar isostatically. No additional sinter process or heat treatment of the target was employed and the pressed target was used directly.

For the deposition of lithium nickel manganese oxide two different powder materials were used. Commercially available powder was purchased from Sigma-Aldrich Co. LLC ($>$ 99 %) and used for the initial samples. Powder material was also prepared by solid state reaction between stoichiometric amounts of $Mn(NO_3)_2 \cdot 4\ H_2O$, $Ni(NO_3)_2 \cdot 6\ H_2O$ and 5 % excess Li_2NO_3 (all materials 99.99 % purity purchased from Sigma-Aldrich) with a synthesis route taken from previous work of Mareike Falk based on a synthesis by Annalena Schlifke at the University of Hamburg.[50,53] The metal nitrates were dissolved in demineralized water to produce a clear green solution. The solution was rotary dried at 80 °C and 5 mbar vacuum and subsequently freeze dried at 0.02 mbar using liquid nitrogen. The resulting highly viscous mass was calcinated at 400 °C for 3 h and crystallized at 700 °C for 5 h. Targets were pressed from both powders identical to the lithium titanate but additionally the target pellets were embedded in unpressed powder and sintered at 700 °C for 5 h.

5.2 Spin coating

Spin coating solutions were prepared according to a synthesis route by Gellert *et al.*[54] based on a PVP (polyvinyl pyrrolidone) route. $LiAc \cdot 2\ H_2O$, $NiAc \cdot 4\ H_2O$ and $MnAc \cdot 2\ H_2O$ (all $>$ 99 %, Sigma-Aldrich, Ac = acetate) were mixed in molar ratios of 0.68, 0.32 and 0.95 respectively and subsequently dissolved in a mixture of HAc, isopropyl alcohol and demineralized water with molar ratios of 20, 28.2 and 43.8 respectively. Additionally a molar ratio of 0.94 polyvinyl pyrrolidone (PVP) (average weight 40.000 g/mol, VWR, dry) was added. The solution was stirred at 50 °C until a clear, light green solution was obtained. Since the solution tended to partly precipitate again after a few hours the solution was also stirred and kept at 50 °C during the spin coating process. Individual layers of the thin film were deposited by dropping 10 µl of the solution onto a spinning substrate at 50 Hz and waiting for 30 seconds. The substrate was then moved into a preheated oven at 600 °C for 4 minutes to dry and calcinate the layer. Before depositing the next layer the sample was removed from the oven and cooled for 1 minute which was generally enough to reduce the temperature to normal levels. The process was repeated between 5 and 20 times according to the desired layer thickness and finally the sample was placed in a preheated oven at 700 °C for 8 min to crystallize the thin film.

5.3 Dip coating and other layer depositions

Dip coating of LTO was performed from a solution of LiAc and titanium isopropoxide in molar ratios of 6 to 5 to account for lithium loss in a mixture of 0.5 ml ethanol, 1.5 ml 2-methoxyethanol and 0.15 ml acetic acid. The ratio of ethanol and methoxyethanol serves to control the evaporation speed of the solution from the sample. Samples were dipped with a pull speed of 5 mm/s and 2 mm/s, dried in air for 10 min and in an oven for 1 hour at 400 °C before crystallization at 650 °C for 4 hours.[55,56] PLD deposition of lithium titanate and lithium niobate interface layers was performed with the deposition parameters of LTO electrode layers in both cases but with reduced pulse count of only 100 pulses. For ion beam deposition a Ar sputter gun with 600 V, 10 mA emmision beam at 0.3 Pa and an argon flow of 4 sccm through the ion gun was used. To prepare the interface films the deposition was performed for 15 minutes using a stoichiometric target of the relevant material which produces films approx. 20 nm thick.

Substrate polishing for the spin coating deposition was done using a “Phoenix 4000” (Bühler) polishing machine in four steps. Before polishing the samples were submerged for approx. 1 minute in concentrated HCl and washed with demineralised water and isopropyl alcohol to remove residues from the industrial process and surface coatings. In the first polishing step the sample was polished with P1000 sandpaper to flatten the surface uniformly. In the following two steps the samples were polished with 9 µm and 3 µm diamond polishing solution on “TexMet” cloths at 200 rpm and 25 kN sample pressure for 5 minutes per step. The final polishing step consisted of 0.05 µm Al_2O_3 particles or 0.02 µm (SiO2) particles on a micro cloth with 150 rpm, 25 kN sample pressure for 5 minutes. Polishing steps were repeated when necessary. Between polishing steps the samples were washed with demineralised water and dish soap. After the polishing steps the wax used to hold the samples in place was dissolved in acetone and the samples were washed with dichlormethane, isopropyl alcohol and demineralised water in that order to remove residual wax, oils, fats and salts. (Practical note: Samples have to be transferred from the organic solvents into the demineralised water quickly or else surface contaminations form on the sample that are difficult to remove once dried in.)

5.4 Pulsed laser deposition

Pulsed laser deposition was carried out with a KrF-excimer laser with a wavelength of 248 nm (Coherent Inc.). The typical deposition parameters for the materials (unless specified differently) were for lithium titanate: a substrate temperature of 650 °C, chamber pressure of 0.3 Pa pure oxygen, target substrate distance of 40 mm, ablation energy of 0.7 J/cm^2, laser repetition rate of 10 Hz and pulse count according to the desired film thickness (typically 10.000 pulses for films about 700 nm thick).[57] For lithium nickel manganese oxide the typical parameters were 550 °C, 20 Pa pure oxygen, 0.7 J/cm^2, target substrate distance of 40 mm, 5000 pulses (ca. 350 nm to 400 nm) and 5 Hz. These parameters given are only for general overview, please refer to the physical characterization for the discussion of the PLD deposition process. Regarding the more general processing the vacuum chamber was initially pumped below 10^{-5} mbar before the deposition pressure was regulated through constant gas flow. Heating and cooling of the substrate was carried out with a rate of 10 K/minute and after deposition the chamber was flooded with 2 mbar Argon to enable reasonable cooling rates below 200 °C. Platinum and titanium layers were also deposited via PLD at 400 °C, 0.2 Pa H_2/Ar (Noxal), 40 mm, 10 Hz, 4 J/cm^{-2}, 1500 pulses (about 20 nm) for titanium and 400 °C, 0.2 Pa Ar, 40 mm, 10 Hz, 4 J/cm^{-2}, 8000 pulses (about 50 nm) for platinum. Titanium was used only for silicon substrates to prevent silicon/platinum alloy formation. Otherwise platinum was used directly as current collector. In some cases platinum was also deposited at 0.2 Pa Ar, 40 mm, 10 Hz, 4 J/cm^{-2}, 8000 pulses at room temperature and subsequently heated in an oven at 400 °C for 4 hours but this was only done due to processing reasons for higher sample throughput and the resulting thin films exhibit no relevant differences.

5.5 Sputter deposition of the “LiPON” solid electrolyte

The “LiPON” solid electrolyte used in this thesis was deposited partly by Matthias Geiß using the setup of the 1st Institute of Physics of JLU and partly using our own setup. For the system used in the physics department the deposition parameters consisted of a chamber pressure of 0.15 Pa pure N_2 with a flow rate of 16 sccm, a RF-magnetron power of 100 W for 120 min with a RF bias of 110 V at a target/substrate distance of 53 mm using a 3 inch diameter Li_3PO_4 target (99.95 %, Kurt J. Lesker company). On our own system a 4 inch Li_3PO_4 target was used at 0.5 Pa pure N_2 with a flowrate of 30 sccm. The RF-magnetron power was 200 W and deposition was generally carried out for about 5 hours. Magnetron power was automatically regulated with RF-bias voltages between 430 V and 230 V depending on target age due to the decreasing target thickness after multiple depositions. The target substrate distance was 65 mm and as opposed to the setup in the physics department the substrate was rotated during deposition. The film thickness was about 1.5 µm for both machine setups signifying a vastly increased deposition rate in the physics department as opposed to our own setup. Since in both setups the substrate could not be cooled, the samples heated up during deposition to about 150 °C even without additional heating.

5.6 Physical characterization methods

X-ray diffraction measurements (XRD) were carried out on an “Empyrean” system (PANAnalytical) for general thin film and powder measurements and on a “X’pert Pro MRD” (PANAnalytical) thin film diffractometer with three dimensional sample stage for grazing incidence film characterisation). For lithium nickel manganese oxide samples the lower and upper energy range percentage of the detector was changed to 49 % and 70 % respectively to reduce the amount of fluorescence from these samples. The standard energy range also used for the lithium titanate was 25 % and 100 %. Individual angle range and measurement times depend on the given material, substrate and crystallinity of the sample but samples directly compared for the deposition characterization were measured with identical measurement parameters. Temperature dependent XRD measurements were carried out in a specialized vacuum/gas flow chamber with X-ray transmissive beryllium windows that allowed to measure the sample *in situ* during temperature treatment (XRK chamber). The X-ray source in both cases was copper K-alpha radiation with 0.154 nm wavelength, extraction current of 40 mA and 40 kV acceleration voltage.

Raman spectroscopy was carried out on a “Senterra” system from Bruker Optik GmbH with a green 532 nm excitation laser. Typical measurement parameters were 20 times magnification and an apperture of 50 µm with a laser power of 2 mW, a resolution of 9 cm^{-1} to 15 cm^{-1} with 3 second measurement time and 30 co-additions for quick probing measurements and 3 seconds 300 co-additions for detail spectra. The wavenumber range in this setup was 55 cm^{-1} to 4000 cm^{-1}. This setup represents the lower possible resolution of the system but at higher grid resolution the intensity of the measurement is generally lower. This often requires either a longer measurement time per spectrum or an increase in laser power. For both systems measured in this thesis general spectrum intensity was a larger problem than wavenumber resolution and increasing the energy load on the sample through higher exposition time or laser power had adverse effects on the sample as shown in section 12. For this reason lower spectra resolution was favored also because for the materials sampled here the fine resolution was of secondary importance. The size of the measurement spot was approx. 10 µm.

High resolution scanning electron microscopy (HSEM) was carried out on a “Merlin” system from Carl Zeiss. To keep the current load on the sample comparatively low samples were generally measured at currents of 100 pA and acceleration voltages of 2 kV. No additional platinum coating for conductivity was used.

5.7 Electrochemical characterization methods

Battery cycling and impedance spectroscopy were carried out on a galvanostat/potentiostat systems from Bio-Logic SA models “VMP3”, “SP300” and “VMP300”. Cycling was generally carried out galvanostatically at 1 µA (3.5 µA/cm^2) for most samples and cyclic voltamograms were measured at sweep rates of 0.05 mV/s. Individual changes to voltage regions and currents are described for the individual samples. Parameters mentioned here are general values used for a majority of samples but for example for thinner films cycling currents have to be reduced proportionally to achieve comparable C-rates and therefore cycling kinetics.

For the charge dependent impedance characterization cells were cycled at (3.5 µA/cm^2) initially for 5 cycles to equillibrate the cells and eliminate possible early cycle effects from the impedance characterization. Afterwards the current rate was maintained but the cycling was interrupted at given time intervals to measure an impedance spectrum. The time between impedance measurements depends on the individual cell performance and the desired measurement point granularity. In general the mentioned current represents a C-rate of approx. 1/6 C to 1/10 C for most cells so in most cases a time interval of 30 min cycling was chosen leading to 10 to 20 impedance points per charge and discharge cycle and changes in SOC between 5 % and 10 % between these data points. Because the specific state of charge varies from cell to cell due to their different overall capacity evaluating the specific state of charge is not feasible and instead the general change in data with progressing state of charge is evaluated. As an alternative to this approach it is theoretically possible to connect the state of charge with the cell potential and measure the impedance at specific cell potentials. This would in theory lead to a comparable state of charge at the same cell potential for all cells regardless of capacity but the problem that emerges is twofold. For one since the resistances of the cells vary as does the capacity, the overvoltages necessary to cycle the cells also vary causing individual cells to once again require individual measurement setups. Additionally, for lithium titanate the charge and discharge plateaus at low current rates tend to be very flat and especially since voltage drops occur after the end of the impedance measurement it is not possible due to voltage variations while cycling to define distinguishable voltage points at which to perform impedance measurements.

The impedance measurement is performed at constant potential around the last voltage point of the cycling step that comes before. The impedance therefore is not strictly speaking measured under cycling conditions. A way to circumvent this is to measure the impedance galvanostatically while overlaying a sinusoidal excitation current. For the cells tested in this thesis though the amplitude of the excitation current necessary to produce even remotely usable impedance spectra was to high to consider the experiment still under linear response conditions. The spectra produced this way also showed superficially similar behavior as well as overall lower quality and will therefore not be further addressed in this thesis. Experimental settings of the impedance measurements were generally an excitation voltage of 20 mV in a range of 0.1 Hz to 1-6 MHz with 10 measurement points per decade and averaging of 3 measurements per point. A waiting period of 0.1 s was used for each measurement frequency. An additional note regarding the depiction of some of the data: For the visualization of the phase angle plots it was often necessary to depict multiple data sets in the same graph to show changes during state of charge or polarization. For these depictions it was chosen to omit the actual data points and instead use a line graph of the data. This was done to retain visual clarity in the graph but can cause problems by suggesting erroneous data trends in regions of data noise. For the Nyquist data this was often not necessary because the data is better distinguishable with data points only being shown.

5.8 Battery cell systems and setup

For the battery cells used in this thesis two basic types of cells were assembled. One system was used for electronically conductive substrate materials and the other was used for insulating substrates. For the conductive substrates the substrate itself was typically used as current collector and contacted directly while for non conductive samples additional current collector layers were employed that had to partly be exempt from further film deposition so that after all layers were deposited the current collector was still accessible for measurement contact. Fig. 1 shows a schematic representation of both contacting methods for a) electronically conducting and b) non conductive substrates. For the electronically conductive silicon the Ti/Pt layer is optional and will be discussed in section 11. The methods shown here are dubbed “back contact” method for case a) since the back of the substrate is electronically contacted and “front contact” for b) since the contact is on top of the substrate.

The preparation of the front contact samples provides some additional challenge since part of the sample has to be masked in all deposition steps which is one of the reasons that this method could not be employed for the spin coating samples since partial masking of the sample was not possible for the conditions during the spin coating process. For the vacuum deposition based techniques this was achieved with a metal mask that was screwed on top of the substrates but for spin coating samples this is not feasible. Other possible masking techniques involve adhesive tape or laquer which would both not be stable against the temperature treatment between spin coating layers. Spin coating samples used in battery cells therefore always had to be deposited on electronically conducting substrates. Lithium metal was applied using lithium foil with a thickness of approx. 500

µm that was pressed on top of the sample.

For contacting the layer systems two different cell setups were used. In the well-type linear assembly the substrate was pressed between two steel stamps and pressure was applied through the use of small springs. For this a custom made well-type cell system that could fit the 10 mm · 10 mm square substrates was used. For the spin coating samples on 12 mm diameter round steel substrates standard Swagelock type linear configuration cells could be used which employ the same principle but are assembled in linear Swagelock piping components. Both cell types are functionally identical but the Swagelock design is somewhat easier to assemble and provides better long term sealing against the atmosphere. For the front contact cells initially a pouch bag design was chosen and the layer system was contacted using Ni metal strips partly coated with a polymer that could be heat sealed inside a polymer bag to prevent exposing the sample to atmosphere while the metal tabs allow contact from the outside of the bag. One tab had to be placed on top of the Li electrode while a second tab had to be placed in contact with the metallic current collector layer. Since all cells had to be assembled in a glove box environment the placement and processing of these small samples using the cumbersome gloves was prone to error. Because of this front contact cells were at later stages of the work assembled using the well-type custom cells mentioned for type a) back contact cells. To achieve this samples on non conductive substrates were placed in the cell system and contact between the metal layer on top and the steel surface at the back of the sample was established using a conductive silver solution to bridge the gap between the front and the back of the substrate. The second stamp that was placed on top afterward did not short circuit with the metal layer or the conductive silver because the Li foil served as a spacer between

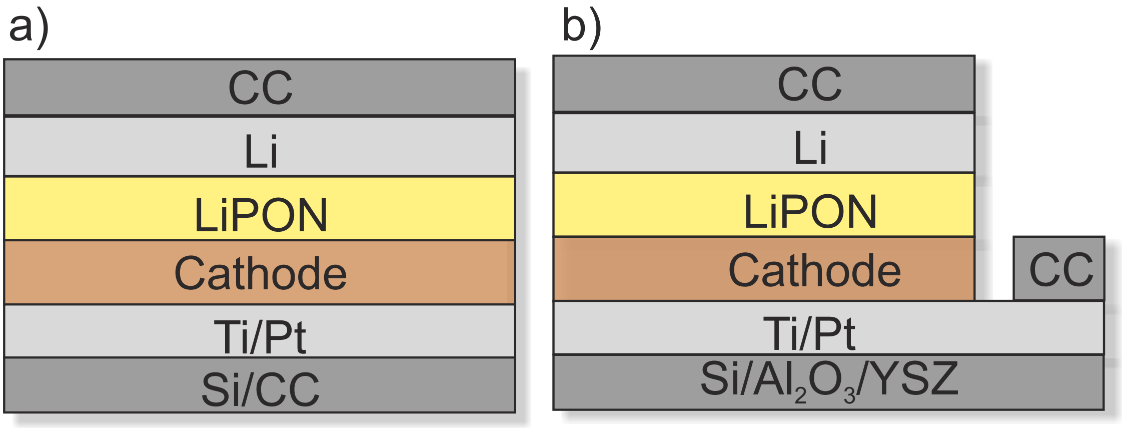

Figure 1: Schematic representation of the battery layer system with a) conducting substrates (Ti/Pt layer optional) and b) non conducting substrates. For the purpose of the lithium titanate impedance characterization the assembly shown in a) is dubbed "back contact" due to the backside of the substrate being contacted and assembly b) is dubbed "front contact" due to the current collector layer on top of the substrate being contacted. (YSZ = Yttria-stabilized zirconia)[58]

the metal stamp and the metal layers. For additional description of the electrochemically active cell geometry refer to section 10.

Both methods of assembly yielded identical cell performance and impedance data (as would be expected since the impact of the electronic transport through the metal contacts and the metal/metal contact resistances are quite small) but the later design was significantly easier to assemble and less prone to error. To apply the silver conductive paste the samples had to be removed from the glovebox for a few seconds after “LiPON” deposition but this did not have a measurable impact on cell performance or impedance data. Since the impedance data of the “LiPON”/Li contact is probed extensively in section 11 effects of the short atmospheric exposition can be neglected. Considerations about the cell design in this thesis are always limited to mechanical and engineering difficulties since the cell type used never had effects on the battery performance of the layer system outside of specific effects caused by the electronic conduction path addressed in section 11. Failure rate of the assembled cells was always the main factor in these considerations.

6 Lithiumtitanate $Li_4Ti_5O_{12}$ (LTO)

6.1 General material properties

Lithiumtitanate (LTO) is, compared to other battery materials, a rather late addition to the pool of anode materials for lithium ion batteries. It was introduced by Ohzuku *et al.* in 1994[6] as a “zero strain” insertion material due to is minimal lattice expansion during lithium insertion and extraction. This very minor lattice expansion makes the material interesting for solid state batteries despite is rather high equilibrium potential (for an anode) of 1.5 V vs. lithium metal. Lattice change in the battery materials can lead to strain inside the battery during cycling and to preemptive cell failure due to loss of contact or rupturing of the separator or even of the entire cell. Under ideal conditions the material delivers a theoretical capacity of about 175 mAh/g.

The main reason for the insignificant volume change of the material during lithium insertion and extraction is the spinel type cubic structure in which the lithium occupies the tetrahedrally coordinated 8*a* Wyckoff positions and 1/6 of the octahedrally coordinated 16*d* position which it shares with titanium (see fig. 2). During lithium insertion lithium is moved from the 8*a* to the 16*c* positions and 3 additional lithium per stoichiometric unit are added to form the rock salt like cubic $Li_7Ti_5O_4$ phase in which the 16*c* positions are occupied while the 8*a* positions remain empty. During insertion ions can move via hopping between the partially occupied 8*a* and 16*c* position since the tetrahedral and octahedral

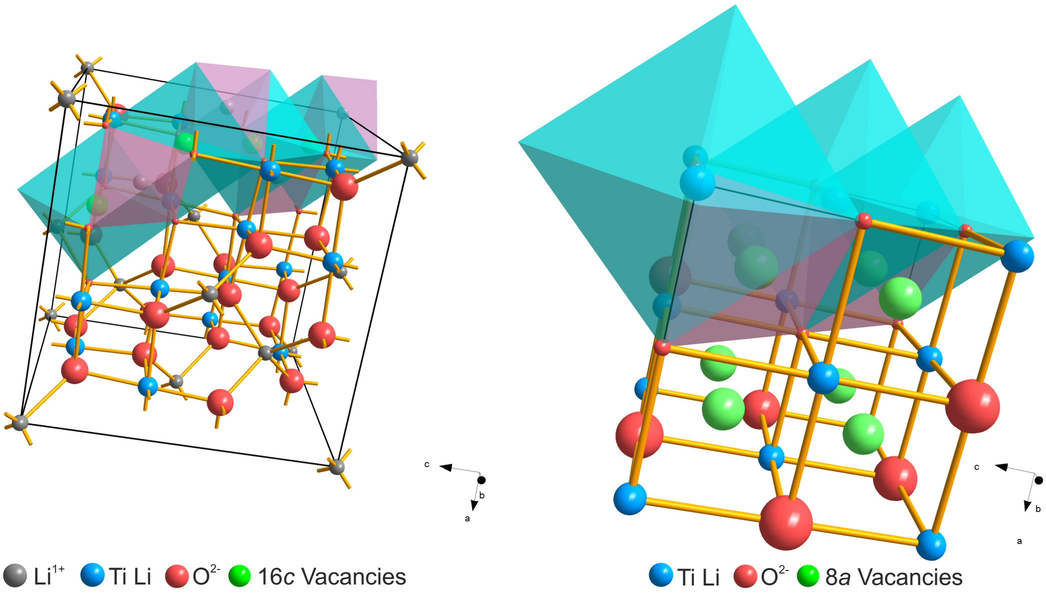

Figure 2: Crystal structure of $Li_4Ti_5O_{12}$ with marked polyhedra for lithium 8*a* tetrahedral sites and 16*c* vacancy positions

positions are face sharing. Despite this seemingly easy conduction path the ionic conductivity of the material is rather low with values around 10^{-9} S/cm to 10^{-7} S/cm reported for the mixed conductivity of the spinel phase with a lithium ion transfer coefficient of 0.97.[59–65]

Data on the lithium rich rock salt phase is more sparse since the material is not stable in atmosphere and can only be synthesized by charging the LTO material. The diffusion coefficient of the rock salt phase is accessible through battery cell measurements and is generally reported to be about two orders of magnitude lower than for the spinel. Values reported range between 10^{-12} cm^2/s for the rock salt and 10^{-10} cm^2/s for the spinel phase which likely leads to a lowered ionic conductivity of the rock salt phase as well. Contrasting this, the electronic conduction behavior of the material changes in the opposite direction. While the spinel phase is a electronic semiconductor bordering on insulating properties with a electronic conductivity of around 10^{-11} S/cm the lithiated rock salt phase shows significantly higher electronic conductivity in the order of 10^{-2} S/cm. This behavior is attributed to the very large band gap of the spinel material leading to the miniscule electronic conductivity.[12,23,66–69] In the lithiated phase due to the reduction of the Ti atoms the Fermi level is elevated into the Ti $3d$ conduction band causing very high conductivity of the material.[59,67,69,70] This difference is also easily visible in the material itself with the spinel phase being a colorless/transparent film and the rock salt phase having a blue tint due to the reduced titanium and light absorption in the visible range.

6.2 Phase change properties and models

The vast changes in the conduction properties and electronic structure of the material lead to a strong dependence on the state of charge (SOC) for the kinetic behavior of the final cell and lead to an asymmetric behavior of the cell during the charge and discharge cycle . This has previously been investigated for liquid based battery systems and several different models of phase transition have been proposed.[15–20] Typically the asymmetry is observed in a larger overpotential during the discharge cycle and deviation of the ideal flat voltage plateau that is expected from a two phase electrode material like LTO. One of the most common explanations is a core shell model of phase transition that assumes phase change of a electrode particle from the outside. In this model, since the outside of the particle (shell) consists of different materials depending on if the cell is currently charged or discharged, the different phase parameters are dominant for the conducting behavior of the particle.[15,16,18,71] This model though is difficult to translate into thin film all-solid-state batteries because some of the assumptions made are no longer true when dealing with a strictly one dimensional geometry of lithium transport. Firstly, the lithium insertion and electronic contact of the particle in a liquid cell are located at the outside of the particle, i.e. both ions and electrons are inserted from the same direction, secondly liquid cells almost always contain additional carbon to facilitate electronic transport which reduces the limitations of the electronic conductivity to the dimensions of a single particle and thirdldy, particle size can vary across a wide range but is often reduced to nanometer sized particles to enhance battery performance, limiting the diffusion length of the occurring lithium ion transport.

In a thin film all-solid-state cell it is typically not easily possible to add additional electronic conduction agents to enhance electronic transport. Furthermore, the length of diffusion for this type of cell is typically identical to the film thickness since the films are often very dense (for PLD films specifically) and contact to the solid electrolyte only exists on the electrode surface. This leads to a comparatively higher length of diffusion of several hundred nanometers. Electronic and ionic insertion are strictly separated due to cell geometry with electronic insertion occurring on the substrate side of the film while ionic insertion occurs at the electrolyte side of the film. Assuming that phase changes occur in the thin film in a mechanism similar to a core shell model (a growing layer mechanism from one side of the thin film) both transport types are now no longer occurring within the same phase.
The phase change of the material itself is quite interesting since it shows all characteristics of a two phase transition which is most prominently displayed in the flat voltage plateau during charge and discharge. In the literature it is shown that the two-phase separation of the material is only thermodynamically fully stable below 80 K with micro domains of the different phases forming between 80 K and 300 K and a solid solution is expected above 300 K.[13,14,72–74] During cycling the two phase separation is only kinetically induced and will relax into a solid solution given enough time and might not even occur at all if the cycling current is sufficiently low. In the thin film cell the film thicknesses, i.e. crystal size, in the range of 300 nm to 1 µm is very close to the size of the expected two phase domains between 80 K and 300 K.

Given these changes in boundary conditions it is not clear if traditional models for phase change in electrode particles are applicable to thin film cells and how the phase change might influence the performance of a all-solid-state batteries based on LTO. In theory phase change might occur similar to a core shell mechanism wherein initial phase change occurs at the substrate or electrolyte interface depending on which transport mechanisms are dominant and a subsequent phase boundary moves through the entire thin film. Should the ionic conduction prove to be a large limiting factor in this case an easy solution to the problem for solid state systems might not be possible.

7 Lithium nickel manganese oxide $LiNi_{0.5}Mn_{1.5}O_4$ (LNMO)

After the initial surge of lithium ion batteries based on the $LiCoO_2$ cathode the quest for higher power and energy densities shifted towards the utilization of cathode materials with increased cell voltage which delivers an easy way to increase the performance data of a given battery cell. Among these high voltage materials the spinel family of manganese based oxides stands out as being easy to prepare, low cost and with Mn being of high abundance.[75] The base material $LiMn_2O_4$ has been intensively studied and today many different derivatives of the base system are known and utilized in active research.[5,7,76,77]
Similiar to LTO the base framework of the system consists of a cubic spinel system in which manganese occupies the octahedral $16d$ and lithium the $8a$ tetrahedral sites. As with LTO some $8a$ sites and the surrounding $16c$ sites remain vacant. In comparison to the layered type material $LiMnO_2$, which is comparable to the $LiCoO_2$ structure, the material features a higher working potential of about 4 V vs Li as opposed to 3 V for the layered material which is also hindered by diffusion limitations orthogonal to the Li layers inside the crystal structure.[78–80]

7.1 General material properties

The average oxidation state of manganese in the spinel material is +3.5 and the voltage plateau describes oxidation/reduction of half the manganese atoms between Mn^{3+} and Mn^{4+}. By introducing nickel into the structure and replacing 1/4 of the manganese the oxidation state of manganese can ideally be shifted to +4 completely in which case the Ni^{2+}/Ni^{3+} and Ni^{3+}/Ni^{4+} oxidation/reduction at around 4.7 V vs. lithium is the only active redox couple in the system. In this case the ideal $LiNi_{0.5}Mn_{1.5}O_4$ ordered phase is formed in which Ni occupies the $4a$, Mn the $12d$, Li the $8c$ and O the $8c$ and $24e$ positions in a primitive simple cubic structure of space group $P4_332$. If the preparation conditions are not controlled precisely the formation of a non-stoichiometric disordered $LiNi_{0.5}Mn_{1.5}O_{4\text{-}\delta}$ phase is also possible. In this disordered phase the space group of $Fd\text{-}3m$ is formed and both nickel and manganese are randomly distributed across the $16d$ octahedral sites which means small amounts of Mn^{3+} remain inside the structure leading to an additional redox couple around 4 V. The formation of the disordered spinel phase occurs mostly at temperatures above 700 °C or in reducing environments during synthesis due to the formation of a oxygen deficiency. This phase is often accompanied by a rock salt-type impurity phase which has mainly be identified as Ni_xO, $Li_xNi_{1\text{-}x}O$ or $(LiNiMn)_xO$. This makes labeling the phase as disordered polymorph of $LiNi_{0.5}Mn_{1.5}O_4$ difficult since the composition is no longer the same as in the ordered phase due to the oxygen and nickel deficiency.[81–83]
For liquid based system it has often been found that the disordered phase offers superior electrochemical performance and for both phases a theoretical capacity of about 147

mAh/g can be calculated assuming all available lithium can be utilized for the cell reaction. The capacity is split across multiple redox processes in the case of the disordered phase. The main limitation of the material in liquid based systems is its rather high working potential which is very close to the decomposition potential of most common organic electrolytes and the tendency of Mn^{3+} to disproportionate into tetra and divalent states forming MnO which is soluble in most electrolytes and leads to loss of active material inside the cell and eventually cathode destruction.[45–48] Both these problems were expected to be trivially solved by the utilization of solid electrolytes since decomposition voltages were expected to be much higher and dissolution of the various forming manganese oxides is not easily possible. In fact the utilization of a high voltage cathode material is necessary if LTO is to be utilized as an anode material because of its rather high working potential of 1.5 V vs. lithium which leads to a significant reduction of the overall cell potential.

7.2 Application in solid cells

Currently one of the main limiting factors of LNMO in all-solid-state cells is the seemingly high charge transfer resistance that is often observed when utilizing the material in contact with common solid electrolytes. Multiple theories about the reason for the high charge transfer resistance exist ranging from space charge layer explanations that result from the large potential drop at the LNMO/SE interface to the formation of degradation layers with low ionic conduction.[34,36,39,84–87] In the same vein different approaches have been proposed to fix this problem by either introducing intermediary layers to improve chemical compatibility, prevent electrolyte degradation or enhance ionic transport through the contact layer.[35,54,86] Another approach proposed by Yada *et al.*[40] and Braun *et al.*[39] suggests that the strong polarization at the interface and therefore the formation of large space charge layers hinders ionic transport through the interface. Yada *et al.* suggested the introduction of a dielectric material with high permittivity (barium titanate in their case) as nanoparticles at the interface to counteract the space charge layer and allow transport along the dielectric particles due to a local electric counter field. In most of these studies improvements can empirically be determined but often the understanding of the underlying mechanisms remains unclear. Thai and Lee for example suggest that the modification could also influence the surface strain and improvement of battery performance might be due to this effect.[52] Recently another publication by Li *et al.*[51] suggested that no additional surface treatment is necessary for the LNMO/“LiPON” system and that rather high performance cells can be deposited by sputter deposition. Their results suggest that the low performance of commonly prepared solid state systems based on LNMO might be based on different factors and that other preparation parameters could be more important for the final behavior than the modification of the interface.

Another problem the LNMO solid state system faces is that often in the first cycle a substantial loss of cell capacity is observed. This is often attributed to the formation of a lithium rich tetragonal LNMO phase. Mancini *et al.*[88] demonstrated that additional lithium can be incorporated into the material in a stochiometry of $Li_{1+x}Ni_{0.5}Mn_{1.5}O_4$ with x ranging from 0 up to a maximum of about 1. The introduction of additional lithium causes the change in symmetry and the additional lithium is inserted and extracted around 3.0 V into the material up to a x value of approx. 0.4 with additional lithium (up to $x = 1$) being inserted/extracted at even lower voltages. Since insertion of this additional lithium happens at low voltage it is often assumed that LNMO cathodes are prepared in a lithium enriched state and in the first cycle the additional lithium is extracted. Because the cells are not cycled below 3.0 V the additional lithium is never reinserted leading to a large irreversible capacity in the first cycle. This concept has some problems when applied to the data of real cells though which will be shown in section 13. In general the material has a multitude of questions that have yet to be conclusively answered and its application in solid-state cells while often desired due to its high working potential is still problematic. It is still unclear if even the right questions are asked regarding this material at the moment.

8 Impedance spectroscopy

Impedance spectroscopy is a widespread electrical analysis technique that relies on frequency dependent impedance response of a electrical system when exposed to a alternating current or voltage signal. When AC conditions are applied to a system the resistive behavior of a system is expanded by an additional component corresponding to the phase relation of the resistance to the applied AC signal. The resistance is therefore split into a component in phase with the signal and out of phase with the signal both of which combined are given as the impedance. The impedance is therefore commonly described as vector in a two dimensional plane and mathematically expressed by a complex number which leads to the description of parts of the impedance being “imaginary” due to the involvement of i but this is of course slightly misleading since the impedance is in fact not “imaginary” but just out of phase to the given AC signal. Depending on the nature of the electrical circuit element probed the impedance response changes depending on the frequency. A simple resistor has no dependence on the measured frequency and its impedance response is always in phase to the applied signal. Its impedance is therefore constant and simply consists of a real part with a magnitude corresponding to the resistance of the resistor. For a simple capacitor though it is readily apparent why the resistive behavior is expected to change depending on AC frequency. For high frequencies the capacitance is not exhausted leading to a simple charge and discharge of the capacitor which has no inherent real impedance while at lower frequencies the capacitance is exhausted leading to full blocking behavior and the impedance becoming essentially infinite. The relation between current and voltage at the capacitor is phase shifted with the current being shifted -90 ° in respect to the voltage and therefore the impedance is out of phase to the AC signal i.e “imaginary”. The same is true in an opposite way for an inductance. From these simple considerations and their mathematical descriptions the impedance of simple circuit elements can be derived according to tab. 1 with the frequency of the AC signal being expressed as ω.[89–92]

Table 1: Basic circuit elements and their impedance.[91]

Component	Equivalent element	Current vs. Voltage	Impedance
Resistor	R [Ω]	$V = IR$	R
Capacitor	C [F, or Ω^{-1} s]	$I = C\mathrm{d}V/dt$	$1/i\omega C$
Inductor	L [H, or Ω s]	$V = L\mathrm{d}I/\mathrm{d}t$	$i\omega L$

In the real world analysis of impedance data for a complex system these equivalent elements are used to describe the electrical behavior of various system processes through meaningful combination of the single elements into combined equivalent circuits describing the observed system process phenomenologically. A simple example is a parallel R/C

combination circuit that describes the behavior of a electrolytic double layer capacitance that has both capacitive properties due to the ionic double layer and resistive properties due to the ionic transport through the double layer. As long as a system is considered ideal it can be described through simple combinations of the three base components listed above. In reality though a system can seldom be considered ideal. For example the R/C element describing the conductive/capacitive behavior of a solid sample (typical conductivity measurements) features resistive and capacitive processes that are influenced by a number of non ideal factors like:

- electrode inhomogenity and surface roughness
- electrode porosity
- variability in thickness and conductivity of surface layers
- nonuniform potential and current distribution at the surface
- grain boundary distribution and phase inhomogenity

To describe this non ideal behavior an additional element is introduced the "constant phase element" (CPE) designated as such because its phase angle part of the impedance is frequency independent and not bound by the strict -90°, 0° and +90 ° phase shift of the capacitor, resistance and inductance respectively. The impedance of this element is given by equation 1.[91]

$$Z_{\mathrm{CPE}} = \frac{1}{Q(i\omega)^{\alpha}} = \frac{1}{Q\omega^{\alpha}}[\cos(\alpha\,\pi/2) - i\sin(\alpha\,\pi/2)] \tag{1}$$

The introduction of an additional factor α allows for the modification of the phase response of this element. It is apparent that for $\alpha = 1$ the impedance takes the form of a capacitor with $Q = C$ while for $\alpha = 0$ the CPE describes an ideal resistor with $Q = 1/R$. Depending on the process measured several possible explanations exist on the exact nature of what the factor α represents but as a first approximation it is best to treat the factor as an empirical constant that allows the inclusion of non-ideal effects.[91] Since the CPE can describe a wide range of possible impedance responses care has to be taken in where it is used and how far the mathematical approximation deviates from the physical reality. Further common derivations of the above ideal circuits and the CPE can be developed for special cases for example for $\alpha = 0.5$ which describes the Warburg element of infinite diffusion. Tab. 2 list a few derivative circuit elements based on the diffusion of a given species. The form of these equations is dependent on the mathematical derivation and the exact conditions used for the boundaries. It is quite common to group various parameters into constants or express them differently leading to some confusion with seemingly different equations for these processes. It is also important to note that several assumptions

Table 2: Derived circuit elements arising for special conditions from the base elements. (with l being the diffusion length, D the diffusion coefficient and $\sigma' = \sqrt{2}\sigma$ the mass transfer coefficient equal to the sum of contributions of Ox. and Red. forms.[89]

Component	Equivalent Element	Impedance
Infinite diffusion (Warburg)	Z_w [Ω]	$\frac{\sigma'}{\sqrt{i\omega}}$
Finite diffusion with transmissive boundaries (Warburg short)	Z_ws [Ω]	$\frac{\sigma'}{\sqrt{i\omega}}\tanh(\sqrt{\frac{i\omega}{D}}l)$
Finite diffusion with reflective boundaries (Warburg open)	Z_wo [Ω]	$\frac{\sigma'}{\sqrt{i\omega}}\coth(\sqrt{\frac{i\omega}{D}}l)$

are made in the derivation of these impedance formula which pertain for example to the boundary conditions and in the case of the finite diffusion that the diffusion coefficients of the oxidized and reduced species are the same. These assumptions made can and have to vary for each system analyzed. The equations listed are intended for use in specific cases where a lot about the system is already known. This is the case for most of the more complex impedance elements common in the field where due to the known system parameters it was possible to reduce the α factor or factors to more tangible physical parameters. In the case of an unknown system the equivalent circuit should be kept as simple as possible as long as not enough about the system is known to justify the assumptions made in the derivation of more complex elements since an impedance spectrum can always be described with a multitude of different equivalent circuits. The fact that an equivalent circuit can describe an observed phenomenon is never indicative for the fact that it is based on correct assumptions.

Another important mathematical relation exists between the CPE and the capacitor capacitance if the CPE is sufficiently similar to a capacitor i.e. the α factor is close to 1. For a single R-CPE or R/CPE element the effective capacitance is given by equation 2, note that the equation changes if another preliminary resistance exists in the circuit and the derivation is technically only valid for a single element. Again different equations for the effective capacitance have been proposed but eq. 2 is the most commonly used.[93]

$$C_\mathrm{eff} = (\frac{Q}{R^{\alpha-1}})^{1/\alpha} \tag{2}$$

Because the derivation of the effective capacitance is rather specific it can also be argued that it is “more” correct to refer to the complex capacitance plot and read the value of the capacitance at the given process frequency from there for more complex systems. If the α factor is close to 1 the difference in capacitance is only minor when compared to the raw Q value extracted from the CPE impedance and if the factor significantly deviates from 1 the concept of capacitance to describe Q becomes very vague. This introduces an inherent vagueness into the capacitance extracted from CPE elements of complex systems on top of the mathematical fitting error.

Because of the strictness of the required assumptions in resolving impedance data mathematically in the real world application impedance data is often analyzed by comparison of measured data to similar systems and empirical values in the literature. In most cases this is a reasonable approach because the basic principles of which processes govern the behavior of a system often are consistent within a given field. For battery research (liquid system) for example the impedance is often governed by the electrolytic double layer forming at the cathode/electrolyte interface or the solid electrolyte interface that exists there as well as diffusion effects. The conductivity of the electrolyte is often too high for the ionic transport to be resolved in common electrochemical frequency ranges (up to several MHz) and the anode/electrolyte interface is often of negligible contribution. In other fields though, dielectric characterization for example, interface effects are often suppressed (mostly intentionally due to experimental design) and the bulk effects of the probed material are of significant importance. This can also lead to some confusion in the language of analysis when for example battery researchers speak about characteristic frequencies and peak frequencies to describe the frequency of a R/C element where impedance behavior switches from mostly imaginary to mostly real contribution, while this frequency is known as relaxation frequency or characteristic relaxation time in dielectric characterization because of the relaxation behavior of electric dipoles in the changing electric field.

The issue arises because fundamentally identical impedance principles are interpreted in a empirical way suited to the given application. The problem facing all-solid-state battery research and thin-film systems especially is that the empirical knowledge is not yet deeply developed and the systems often exhibit a mix of contributions that are not typically observed in other fields because both the interfaces and the dielectric properties of the bulk phases are important in the analysis. Since the prior knowledge of the experimentalist is the main factor in the determination of a suiting equivalent circuit this can lead to misinterpretations because impedance data can always be represented by multiple equivalent circuits. In an unknown system it is necessary to reevaluate these prior assumptions with changes to the experimental setup and to verify the nature of assumed processes in order to produce reliable conclusions.

9 Preparation and characterization of LTO thin films

In order to prepare functioning and reliable thin films for the impedance characterization a wide array of parameters for thin film deposition and film processing were explored. In the following the analysis will be focused on a selected few parameters and mostly the properties of the found "ideal" parameters will be showcased since the influence of most other parameters was negligible. The starting parameters for deposition optimization was adapted from Hirayama *et al.*[57] and were quite applicable to the given machine setup which is not typical since PLD setups tend to not retain identical deposition parameters between different machines.

9.1 PLD parameter overview

To give some context for the chosen parameters and variations, initially variation of the temperature is the most straightforward approach to manipulate the properties of the thin film. According to the phase diagram shown in fig. 3 the LTO phase is stable up to about 1015 °C so in the chosen temperature range between 650 °C and 800 °C no degradation of the material is expected (adapted from[94]). In that range the most likely possibility for

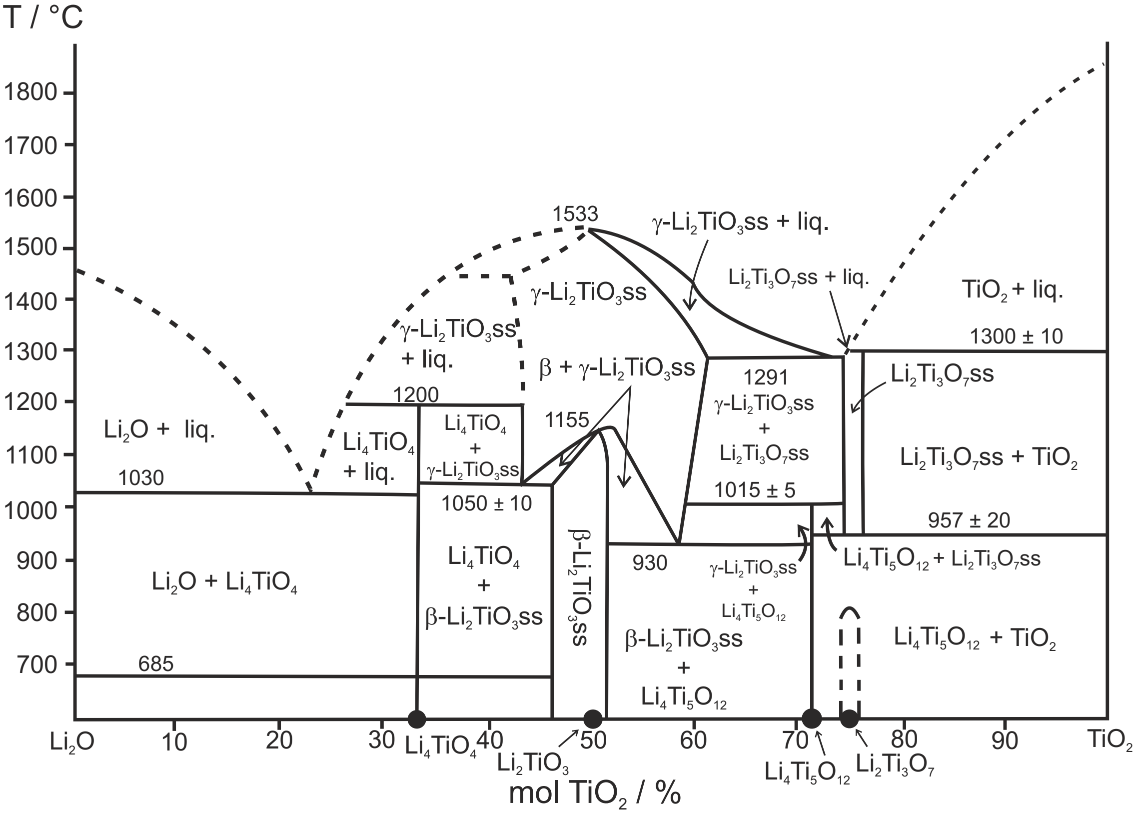

Figure 3: Quasi-binary phase diagram of lithium oxide and titanium dioxide (adapted from[94]).

an impurity phase is titanium dioxide since during the PLD process a loss of lithium or lithium dioxide seems more likely than an excess of those. The loss of lighter components during the PLD process is a common problem. Even in the case of excess lithium the lithium is not necessarily incorporated as lithium oxide as depicted in the phase diagram but could also be incorporated into the spinel structure like expected for the electrochemical insertion. This again can be dependent on the oxygen partial pressure during deposition since the availability of oxygen can influence formation of oxygen deficiencies and possible non stoichiometric phase compositions. Another feature typical for PLD thin film deposition is a strong preferential orientation of the resulting films. This orientation is mostly governed by combination of the surface energies of the substrate versus the energy of the relevant crystal plane and the surface energies between the crystal surface and the PLD atmosphere. The pressure during deposition therefore can have an impact on the film orientation. Due to the rather tight window of variation for this parameter of only about 2 - 3 decades limited by the utilized system a significant impact is rarely observed though. In this thesis the pressure was varied between 0.3 Pa and 20 Pa partly because the machine setup would not allow for a much larger variation with pure oxygen alone and partly because favorable results were already obtained in this pressure region as will be shown in the following. In the case of surface kinetics substituting a higher chamber pressure with an increase in the working distance is feasible since the increased travel distance of particles leads to more particle collisions in the gas phase and therefore lower kinetic energy at the surface. The increased distance has no influence on the surface energy itself though.

The influence of the working distance (WD) is mostly felt in the deposition rate since the plasma cone becomes less dense the higher the distance to the origin point gets (and the higher the chamber pressure is but again to a lesser degree). Additionally, a higher working distance can help to reduce macroscopic target particles (droplets) that form when either large parts of the target are ablated due to tearing because of the explosive formation of the plasma cone or due to “splashing” of molten target material. These droplets though are rarely completely avoidable in PLD deposition and are often the main contribution to overall surface roughness of the thin film. Since for this material the number of droplets formed was already quite low and no significant further reduction with increased working distance was observed it was decided to keep the deposition rate at a reasonable level by utilizing a distance of 40 mm.

The energy needed to bring the target material into the plasma phase can vary but is typically somewhat tied to the thermal conductivity of the material. Metals typically require quite high ablation energy because of their high thermal conductivity while other anorganic compounds (e.g. oxides) generally require less. Organic compounds are often very difficult to deposit because they easily degrade and can only be ablated with very low energies and typically only in the IR wavelength region. Since after the minimum ablation energy is reached higher energies only introduce the risk of more droplet formation, material degradation or kinetic impact damage on the substrate (since the particle energy after ablation is already quite high), the energy is typically kept at the lowest level possible to allow sufficient ablation. In the case of LTO while starting out a energy of about 2.5 J/cm^2 was utilized but as was also shown by Hirayama *et al.*[57] a lower energy of 0.7 J/cm^2 is enough for material ablation.

9.2 X-Ray diffraction analysis

Fig. 4 depicts XRD patterns for LTO thin films deposited on silicon (100) substrates at varying temperatures with otherwise constant deposition parameters. A reference pattern measured from the bulk material is also given. As can be seen the LTO phase forms at all tested temperatures and the visible reflexes can be indexed as the (111), (222) and (115) reflex indicating a strong preferential orientation along the (111) direction. This orientation is also typically observed in the literature if not specifically grown otherwise.[24,57,95,96] Aside from the reflexes typical for LTO some additional impurity phases can also be iden-

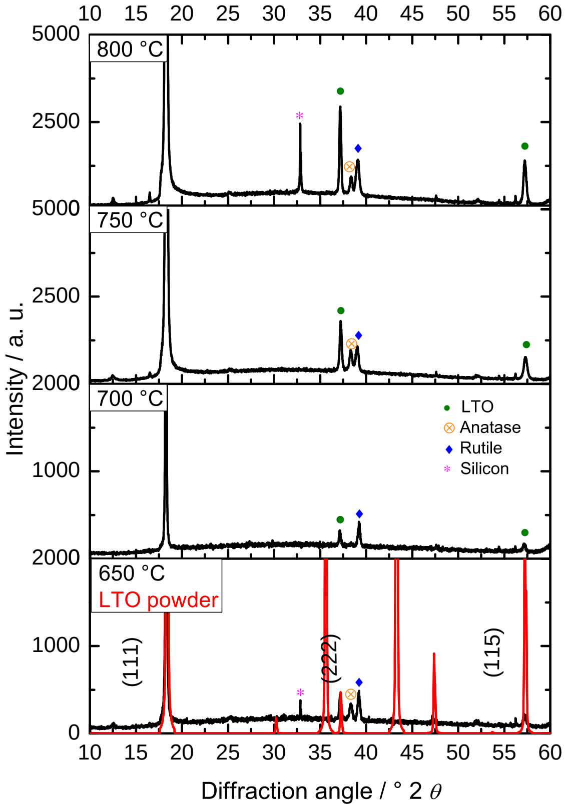

Figure 4: XRD pattern of LTO thin films on silicon (100) substrates deposited with varying substrate temperatures. (constant parameters: 0.3 Pa oxygen pressure, 40 mm WD, 2.5 J/cm^2, 10 Hz, 10k pulses)[58]

tified. Referring back to the phase diagramm shown in fig. 3 the two reflexes near about 40 ° can be attributed to the titanium dioxide rutile and anatase phases. With the temperature ranging above 600 °C rutile would be expected to form but since PLD deposition is not a equilibrium process formation of anatase is not impossible. The reflexes are the (020) for rutile and (112) for anatase which typically have low intensity in the bulk material but are the only ones visible here due to the orientation. An increase in temperature has seemingly no impact on these impurity phases under the given conditions although the anatase reflex disappears at 700 °C this is more of a random effect of the film growth since across multiple samples the ratio between anatase and rutile would vary. The pattern was included here to showcase this effect.

The crystallinity of the thin film increases with higher deposition temperature as expected which is seen in the pattern as increased reflex intensity mostly notable for the smaller reflexes since the (111) reflex is scaled out of the visible area. Note here that the intensity scale for the two highest temperatures is scaled differently to keep a consistent comparable image. Lastly the reflex around 33 ° indexed as a silicon reflex has to be discussed. The substrate used as mentioned was a (111) oriented silicon single crystal substrate that has a very high intensity main reflex around 70 ° but also some smaller side reflexes that can appear due to small crystal imperfections and the position of the sample in the measurement setup. These side reflexes have typically a very low intensity compared to the main reflex but compared to the thin film reflexes the intensity can be quite high. They can be easily identified due to the sharpness of the reflex. One of these reflexes often appears around 61 ° and considering the main reflex at 70 ° has a broad base due to its high intensity the display range of the pattern here is limited to 60 °. The reflex around 33 ° is also a side reflex of the silicon substrate and thus appears and disappears in the pattern randomly as explained above. Overall the influence of deposition temperature in the given range is quite small and most importantly has no impact on the impurity phases as would be expected considering the phase diagram since the impurity is based on composition and not temperature dependent in this range.

Fig. 5 depicts XRD patterns of LTO thin films on silicon (100) substrates deposited with varying oxygen chamber pressures. The temperature in this case was kept at 650 °C and note that the ablation energy for this data set was changed to 0.7 J/cm^2. To address the change in ablation energy first: since the temperature dependent data set shows that the main impurity phase was TiO_2 the composition of the thin film is skewed towards lowered lithium stoichiometry i.e. lithium or lithium dioxide loss occurs during deposition. As mentioned in the initial parameter overview the ablation energy modifies the kinetic energy of the plasma particles and if the kinetic energy becomes to high particles can be

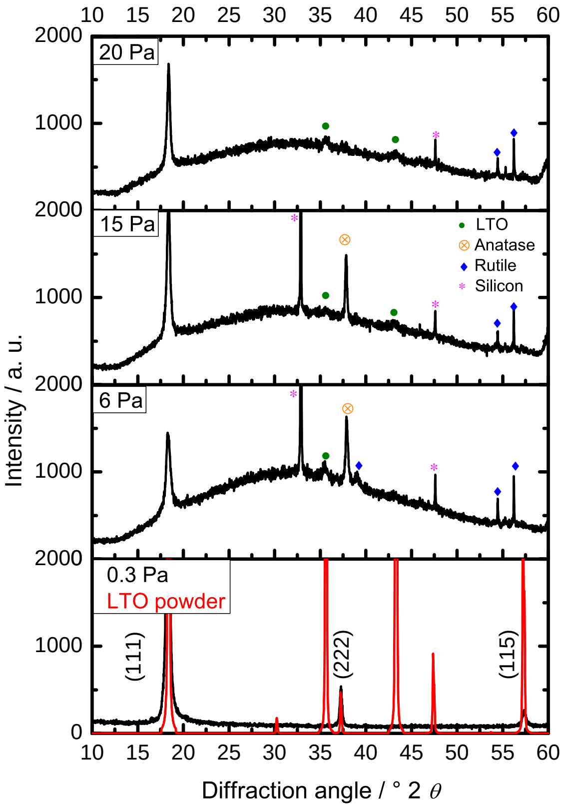

Figure 5: XRD pattern of LTO thin films on silicon (111) substrates deposited with varying oxygen chamber pressures. (constant parameters 650 °C, 40 mm WD, 0.7 J/cm^2, 10 Hz, 10k pulses)

reflected from the substrate. Since the kinetic energy of the lighter components is higher than of the heavier components this is one of the main reasons for the often observed loss of lighter components. By decreasing the ablation energy this effect can be mitigated to some degree which is why, as mentioned in the overview, the ablation energy should in most cases be kept as low as possible. The full data set for the determination of the optimal ablation energy is not shown since the most significant result can be seen when comparing the bottom pattern of fig. 4 and 5 which are deposited with identical parameters aside from the ablation energy. The sample deposited with lower energy shown in fig. 5 only displays reflexes attributed to the LTO phase while the previously observed rutile and anatase impurities have disappeared. Higher ablation energies still showed impurity phases and lowering the energy further is not possible due to the experimental setup and power limits of the laser itself.

Raising the chamber pressure during deposition leads to an immediate reduction of film crystallinity as is apparent in the strong decrease of reflex intensity and also in the appearance of a more pronounced underground signal. Additionally very small reflexes for the LTO (113) and (004) orientation start to appear which might indicate that the (111) film orientation becomes less energetically favorable towards higher deposition pressures because of changes in the surface energy relations. The loss in crystallinity probably stems from the reduced kinetic energy of the plasma particles due to the higher amount of particle collisions in the gas phase. Since the kinetic energy of the particles is already lowered by reducing the ablation energy the partial formation of an amorphous phase might be possible even at 650 ° C since the temperature is only held for about 20 min during the deposition. Reflexes of titanium dioxide start to reappear as soon as the chamber pressure is raised although those suffer from low crystallinity as well. An additional reflex of the LTO phase at about 43 ° is attributed to the (004) direction and indicates a diminishing of the preferential orientation but due to the overall decrease in reflex intensity the reflex is very small. The increase of the impurity phases can once again be explained by the shift of film composition through the kinetic energy of the plasma since the increased gas density in the chamber affects the heavier plasma components (mainly titanium) more than the light components (lithium) shifting the reflection rates again in the favor of lithium loss since even at this rather low ablation energy the plasma tends to be quite big indicating a high ablation and therefore high particle energies.

Some of the reflexes attributed to rutile seem to be quite sharp and could also possibly be attributed to minor reflexes of the silicon substrate that can appear at the same diffraction angle. Since, as mentioned above, the silicon reflexes tend to appear and disappear depending on the substrate position during the measurement a scan with an omega offset of 2 ° was performed on a sample with optimized deposition parameters in order to eliminate possible substrate influences and to allow for a larger range of diffraction angle measured (see remarks about angle limitations above). Fig. 6 depicts the XRD pattern of this optimized sample (650 °C, 0.3 Pa O_2, 40 mm WD, 0.7 J/cm^2, 10 Hz, 10k pulses) as well as a LTO powder pattern simulation for reference. With the increased range of diffraction angle measured an additional reflex at ca. 79 ° is visible that is indexed as the (444) reflex and is expected considering the strong preferential orientation of the sample. The intensity proportions between the (111), (222), and (444) reflexes (100 % to roughly 3% and 6%) are similar to the powder pattern with the (115) reflex obviously differing from the expected proportion due to it not belonging to the preferential orientation (1.4 % as opposed to 17 % in the powder pattern). The broad signal around 70 ° is attributed to some remaining reflex intensity of the silicon single crystal reflex that could not be entirely suppressed without losing significant intensity in the thin film reflexes. Aside from the reflexes attributed to the LTO no further reflexes are visible indicating that these parameters allow the deposition of phase pure LTO with strong (111) preferential orientation.

To further evaluate the crystalline properties of the material Raman spectroscopy was employed. Since the XRD technique is not very sensitive to lithium ordering and positioning inside the material there is no significant difference between the $Li_4Ti_5O_{12}$ phase

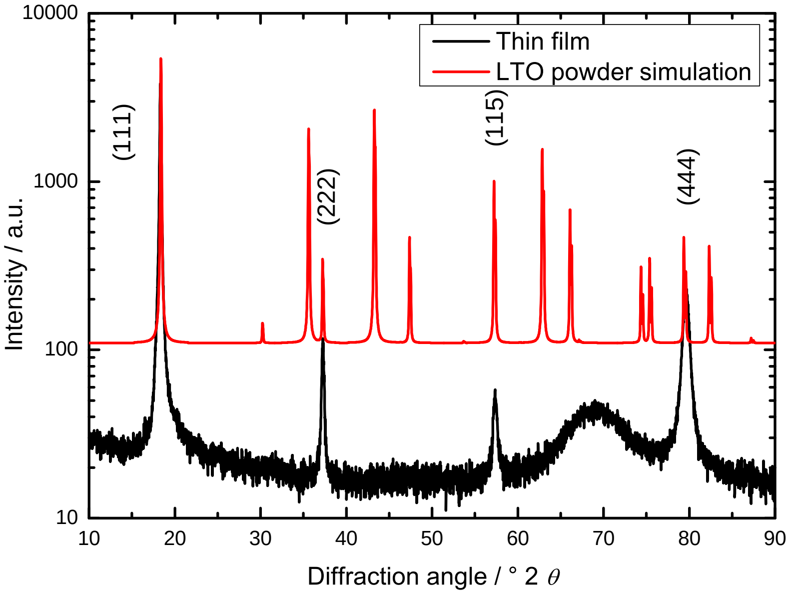

Figure 6: XRD pattern of a LTO thin film deposited on a silicon (111) substrate measured with an omega offset of 2 °. LTO deposition parameters were optimized to 650 °C, 0.3 Pa O_2, 40 mm WD, 0.7 J/cm^2, 10 Hz, 10k pulses

and the more lithium rich compositions towards $Li_7Ti_5O_{12}$. The low spacial expansion of the material during lithium insertion is also problematic when trying to discern differences between the pure and lithiated phase since no significant difference in the lattice parameters leads to only minor differences in the XRD pattern at very high diffraction angles (around 160 ° to 180 °) not easily measurable with common setups.[12]

9.3 Raman spectroscopy analysis

Fig. 7 shows Raman spectra for the LTO thin film on a Pt/YSZ substrate as well as the utilized target material. Also given are comparative spectra for rutile and anatase taken from the RRUFF database. The substrate was chosen since typically when operating on pure silicon the strong bands of the substrate make interpretation of the thin film bands difficult. The main bands visible in the LTO spectrum are the Li-O bending and stretching modes at 165 cm^{-1}, 345 cm^{-1} and 425 cm^{-1} as well as the Ti-O bending and octahedral vibration modes at 230 cm^{-1}, 670 cm^{-1} and 745 cm^{-1}.[56,63,97,98] For the thin film the intensity and quality of the measured bands is significantly decreased compared to the powder material. Some of the intensity reduction can be explained since less material is measured in the thin film as opposed to the powdered material but increasing measurement time or excitation energy only leads to a higher overall intensity not a qualitatively different spectrum. The broadening of the bands appears to be more prevalent for the Li-O vibrations as opposed to the Ti-O vibrations that remain relatively sharp. As outlined in section 6 in the stoichiometric $Li_4Ti_5O_{12}$ phase lithium exists in the the 8a tetrahe-

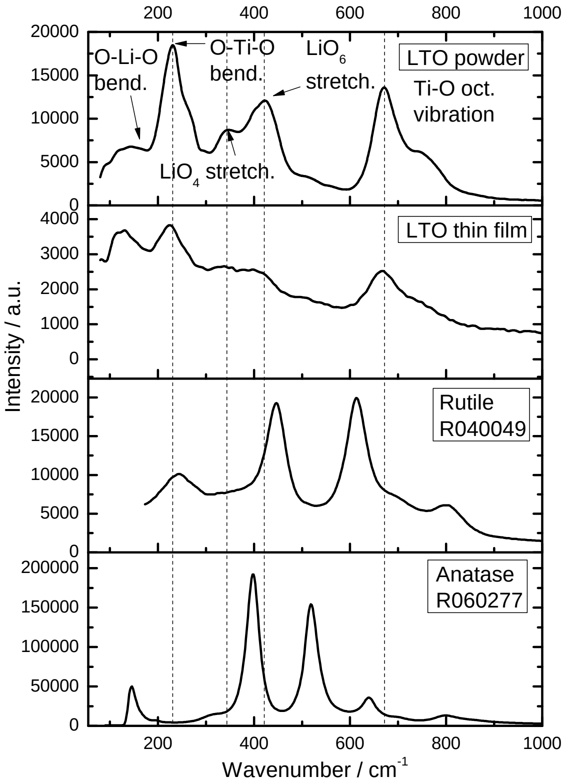

Figure 7: Raman spectra of LTO thin films on Pt/YSZ substrates and spectra for the target material as well as comparative spectra for anatase and rutile taken from the RRUFF database.

dral positions and the $16d$ octahedral positions together with titanium. When additional lithium is inserted, lithium is moved from the $8a$ to the $16c$ positions and the $16c$ positions are filled to achieve rock salt structure in $Li_7Ti_5O_{12}$. Leonidov *et al.*[63] have shown that the Raman spectrum of LTO changes depending on the temperature during measurement since the lithium in the $8a$ position becomes mobile and the lithium positions (and therefore the vibration energies of the Li-O bond) become blurred. This is essentially the same as the shuffling of lithium positions that occurs when additional lithium is inserted during the electrochemical phase transition. It is possible since the film stoichiometry was manipulated to incorporate more lithium as opposed to titanium to reduce the prevalence of TiO_2 impurity phases, that the film now has a slight lithium excess. This would cause shuffling of the lithium positions as described above and broadening of the bands. Note here that the titanium vibrations are not expected to be independent from the lithium ordering since introduction of additional lithium into the $16c$ octahedral sublattice causes Ti positions to become non-equivalent. Indeed a broadening of the titanium bands can bee seen when compared to the powdered material similar to the results of Leonidov *et al.* In regards to the phase purity similar results to the XRD patterns were observed. The thin film shows no significant features of the rutile and anatase impurity phases granted that the characteristic bands for those phases are rather close to the LTO bands and might be present beneath the LTO features. The absence of the strong anatase feature around 510 cm^{-1} and rutile feature at 612 cm^{-1} though indicates that the amount of impurity phase, if present, is very low.

9.4 Surface and film morphology

Fig. 8 a,b and c shows HSEM images of the produced LTO thin films deposited at different oxygen pressures. The images further indicate the possibility of a slight lithium excess at lower deposition pressures. While the overall appearance of the films does not differ much the surface of the film deposited at 0.3 Pa appears blurred as if covered with a thin layer of amorphous material. The crystal structure beneath is still visible as it appears for the 6 Pa and 15 Pa film. When the deposition pressure is increased this amorphous film is visibly reduced and vanishes for the sample prepared at 15 Pa. Since the samples were all handled in air the thin layer might form if excess lithium from the film is drawn towards the surface to form lithiumoxide and lithiumcarbonate which is a often observed phenomenon for lithium rich materials. With increasing chamber pressure during deposition the lithium content in the film is reduced and excess lithium can no longer form

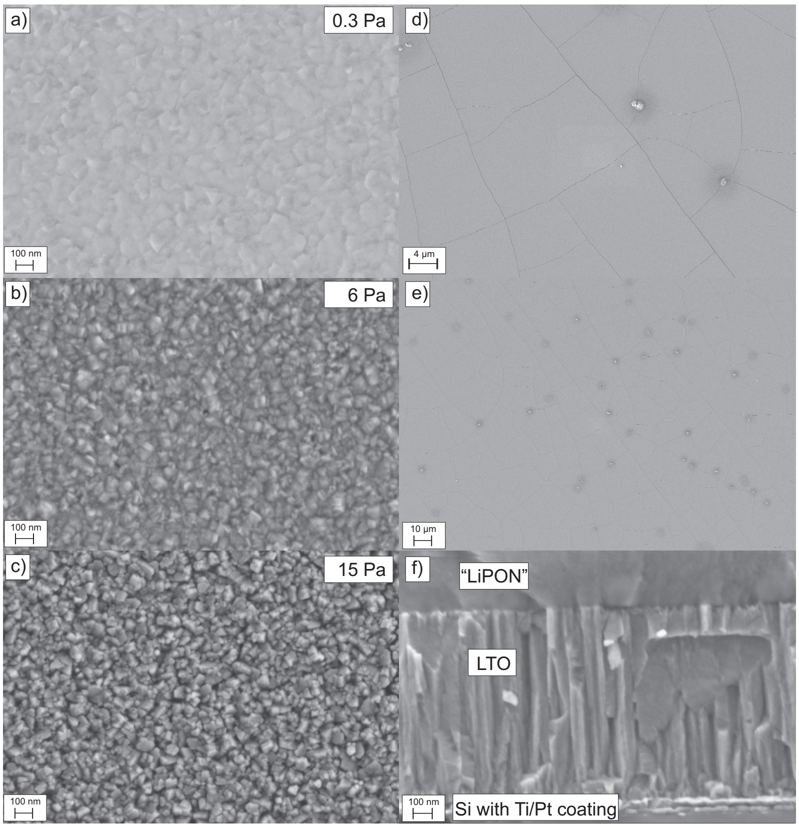

Figure 8: HSEM images of the LTO thin films deposited at varying chamber pressures (a,b,c) , the LTO film surface for droplet analysis (d,e) and a cross section of the film in an assembled all-solid-state battery (f).

this layer at the sample surface. Since in the later electrochemical characterization no ill effects of this surface layer were observed it is either sufficiently thin to not impact the measurement or is destroyed during further processing ("LiPON" sputtering). It might also be dissolved once the cell is cycled or be incorporated in the formation of an interphase. X-ray photoelectron spectroscopy (XPS) and secondary ion mass spectrometry (SIMS) measurements show indication of these lithiumoxide and lithiumcarbonate species at the sample surface but as mentioned this is typical for lithium rich materials. Depth profiling showed no clear difference between the samples either because the films are very thin or because surface mixing due to ion bombardment during the depth etching obscured the exact film thickness.

Regardless all films appear relatively smooth with crystal diameters in the range of 20 nm to 100 nm. The surface overview in fig. 8d shows that despite the smoothness in the microstructure the films exhibits cracks and particles at the surface. The cracks are likely formed due to thermal strain while cooling the sample after deposition. The cracks are generally more prevalent in samples deposited on silicon due to its low thermal expansion coefficient and are reduced when utilizing Ti/Pt interlayers while mostly disappearing if the material is deposited on YSZ/Pt or sapphire/Pt. It is assumed that in the final cell these cracks are filled or covered when the solid electrolyte is deposited on top since short-circuiting or delamination was not typically observed. The particles visible are typical PLD artifacts ("droplets") formed by scattering or splashing of the target material. The broader overview in fig. 8e shows that these particles appear randomly across the surface with a general particle size of about 1 µm. Most cracks in the film seem to originate or correlate with the impact sites of the droplets due to the additional strain/film defects at these positions. Droplet number and size could be reduced by increasing the working distance but the simultaneous decrease in deposition rate and the formation of impurity phases out weigh this improvement.

The cross section in fig. 8f shows the expected strong columnary growth behavior of the thin film with most crystals stretching across the entire film thickness. The smaller layers at the bottom are the Ti/Pt interlayers deposited and the layer on top is the sputtered "LiPON" solid electrolyte. The contact between all layers appears to be uniform and no delamination or easily determinable interface defects seem to form. No indication of the before mentioned lithiumoxide/lithiumcarbonate layer is present at the top of he LTO thin film possibly because it was removed during sputtering of the solid electrolyte or simply because it is too thin to be visible in the cross section.

In summary it was possible to deposit phase pure LTO thin films with the optimized parameter set (650 °C, 0.3 Pa O_2 40 mm WD, 0.7 J/cm^2, 10 Hz, 10k pulses) but slight variation causes formation of impurity phases. The main cause is likely the lithium/titanium stoichiometry of the thin film that can be controlled through the kinetic energy of the plasma particles i.e. the ablation energy and the chamber pressure/working distance. Lithium reflection from the substrate due to high kinetic energy is likely the most important factor for the stoichiometry. Ablation energy has to be kept low since the low thermal conductivity of the target causes a high efficiency in energy transference into the plasma and chamber pressure equally needs to be low as to not obstruct titanium deposition too much. Under optimal parameters formation of impurity phases could be prevented but the thin films likely feature a minute excess of lithium indicated by Raman and HSEM data. The films appeared smooth but when utilizing pure silicon formation of cracks due to thermal strain could be observed.

10 Electrochemical characterization and processing setup for LTO based batteries

To characterize the electrochemical behavior of the LTO thin films galvanostatic cycling and cyclic voltammetry was performed. Since the thin films were intended for model studies in the impedance measurements the focus while preparing the system was not set on optimizing the battery performance from a capacity or cycle life point of view. Most of the electrochemical and kinetic limitations that influence the data shown in this section are explained due to either high resistances involved in the cell setup or in inherent properties of the LTO material that will be discussed in depth in the impedance data. This section serves to illustrate the basic properties of the cells studied.

10.1 Cell design basis and development

Since a lot of the early problems in the performance of the cells were rooted in the experimental setup and cell processing a short overview of various attempts and decisions made will be given that resulted in negative measurement results themselves but lead to the final method of cell assembly and processing. Fig. 9 depicts an early cell test of a LTO thin film (800 °C, 0.3 Pa O_2, 2.5 J/cm^2, WD 40 mm, 10 Hz, 10000 pulses) in liquid electrolyte (ethylene carbonate, diethyl carbonate 3:1 with 1 mol/l $LiPF_6$) with lithium metal as anode and a constant current of 10 µA/cm^2. Initially the cell delivers a reversible

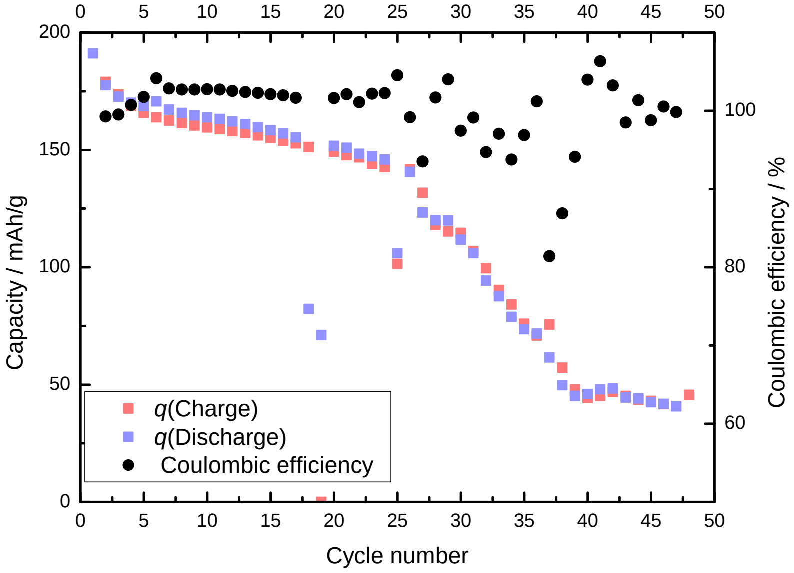

Figure 9: Early thin film test in liquid electrolyte (EC:DEC / 3:1, 1 mol/L $LiPF_6$, 10 µA/cm^2). Early cycles appear close to the expected behavior but the cell experiences rapid capacity fading after approx. 25 cycles.

capacity close to the theoretical capacity of 175 mAh/g. In the first cycle the theoretical capacity is exceeded which can be an indication of initial SEI formation at the Li anode but since the mass of active material is estimated through the thin film dimensions, which will be discussed further during the impedance characterization, the value lies within the margin of error. Note also that the cell has no initial charge cycle since the material is deposited in the charged state. A strong capacity fading is evident even during the first 25 cycles that increases rapidly after the 25th leading to cell failure. Post mortem analysis of the sample revealed partial dissolution of the LTO thin film. It is well known that $LiPF_6$ in the electrolyte can form HF with trace amounts of water which can lead to a dissolution of active material in a liquid cell. This is especially harmful for very thin films since the amount of active material is very low. The properties of the thin film itself seemed reasonable considering problems in this setup were likely caused by interactions with the liquid electrolyte. Since the performance and optimization of the liquid system is not the focus of this thesis it was decided to skip straight into the solid state system without addressing the problems in the liquid system first.

In order to maximize the chance of a functioning cell, since short circuiting is commonly a problem with thin solid electrolyte films, early cells featured an array of four 4 mm^2 electrodes on top of a 1 cm^2 substrate. This was supposed to allow the utilization of different electrodes in case one or more featured a short circuit. It was quickly evident though that the resistances of those small electrodes were too high and the capacities of the resulting micro batteries too low to allow a reasonable cycling behavior since the absolute currents necessary to cycle these cells were in the 10 nA range and therefore difficult to measure. Overpotentials were vastly increased due to the high current density applied to the samples. The electrode area therefore was increased to 68 mm^2 in order to allow a small strip of the 100 mm^2 substrate around the thin film to remain free. This was to ensure full coverage of the thin film when the “LiPON” solid electrolyte was deposited in the following step since otherwise mixing of the different layers or contact to the current collector tabs in the pouch cell assembly would have been possible at the edge of the sample. The cell was then completed with a round piece of lithium foil with 6 mm diameter on top of the 8 mm · 8 mm thin film electrode to allow for some leniency during cell assembly since positioning the electrodes perfectly is hindered due to the glovebox working conditions. This lead to the final cell geometry with an active area of 0.2827 cm^2. Later the cell system was switched from mainly pouch cell assembly to mainly well type assembly which meant that the LTO electrode was no longer required to be only 68 mm^2 since contact of the current collectors at the sample edge was impossible. To keep the measurement results comparable to earlier results though the active areas of the cells was kept at 0.2827 cm^2.

10.2 Electrolyte impurity

After the initial problems with cell geometry reasonably functional all-solid-state thin film batteries could be prepared. Fig. 10 depicts cycling data of early all-solid-state cells. The cells operate quite stable across 50 cycles with minor capacity fading after 5 cycles but exhibit rather low Coulombic efficiencies. The solid electrolyte utilized in these cells was deposited with the, at that time, newly acquired sputter deposition setup. As was later discovered in collaboration with Martin Busche, Thomas Leichtweiß and Matthias Geiß the electrolyte had significant iron impurities that were caused by ablation of the anode ring that was part of the sputter source setup. This iron impurity led to a increased electronic conductivity of the solid electrolyte causing the cell to self discharge at a relatively fast rate. Fig. 11 depicts a self discharge profile for such a cell. The cell was initially charged to 2 V and displayed in the graph is the following OCV behavior. It is evident that the cell discharge is nearly complete after about 40 hours. Considering the typical LTO thin film deposited with the optimized parameter set contains about 12 µAh of charge capacity this equates to a absolute self discharge current of 0.3 µA or roughly 1 µA/cm^2. Since the self discharge leads to increased net charge capacities and decreased net discharge capacities the efficiency of the cell is reduced. From the current values given above the expected efficiency is about 55 % for the applied absolute cycling current of 1 µA which was exactly what was measured for this particular cell. Typically the efficiency for these cells would vary between about 60 % to 80 % indicating that the induced electronic conductivity of the electrolyte was not constant. With the dimensions of the electrolyte (area 0.2827 cm^2,

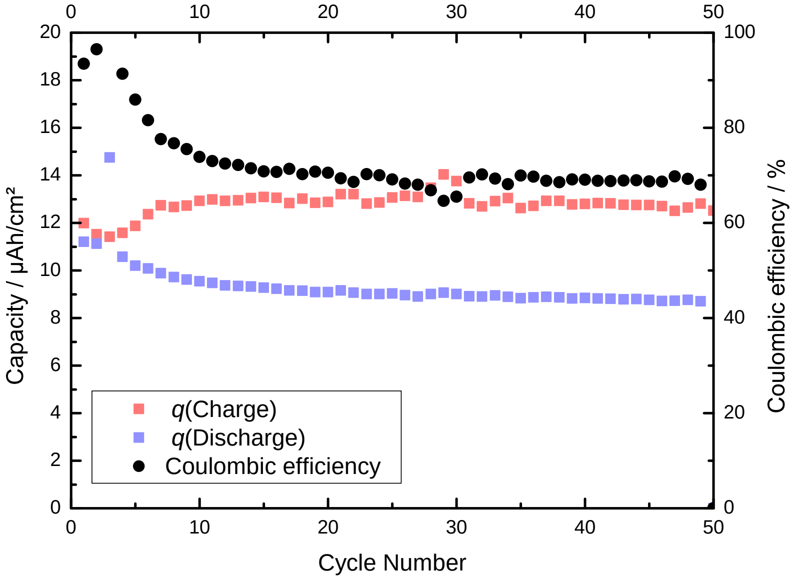

Figure 10: Early all-solid-state thin film cells deposited with optimized parameters on a silicon substrate. Clearly visible is the low Coulombic efficiency caused by impurities in the solid electrolyte.

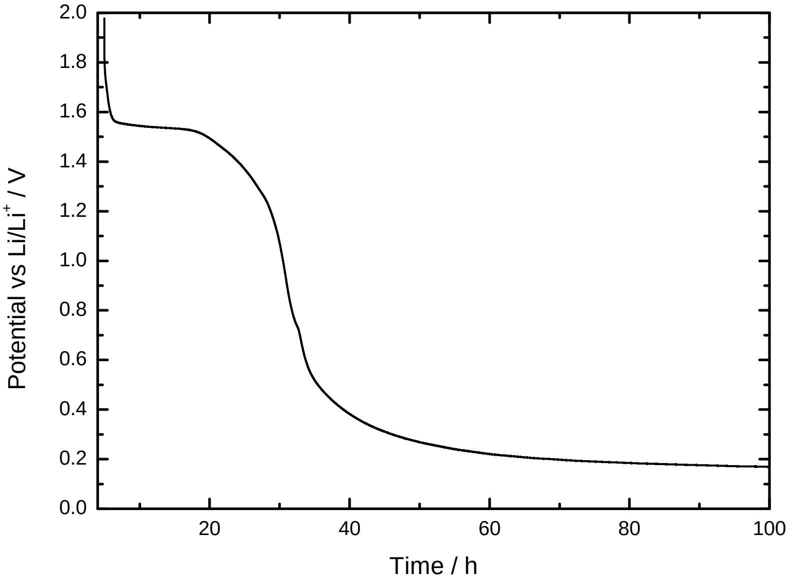

Figure 11: Self discharge profile of a LTO thin film all-solid-state battery with impure electrolyte.

thickness 1.5 µm) this leads to an electronic conductivity in the range of 10^{-10} S/cm. The presence of iron was also confirmed by SIMS depth profiles (fig. 12a) and XPS measurements (work of Martin Busche and Thomas Leichtweiß not shown here). Though quantification is difficult the SIMS depth profile clearly shows the presence of iron inside the "LiPON" film and the signal disappears as soon as the glass substrate is reached. The relatively high intensity of the silicon signal in the thin film is also caused by the sputtering impurities since the anode ring consist of industrial steel and therefore not only iron is deposited onto the substrate.

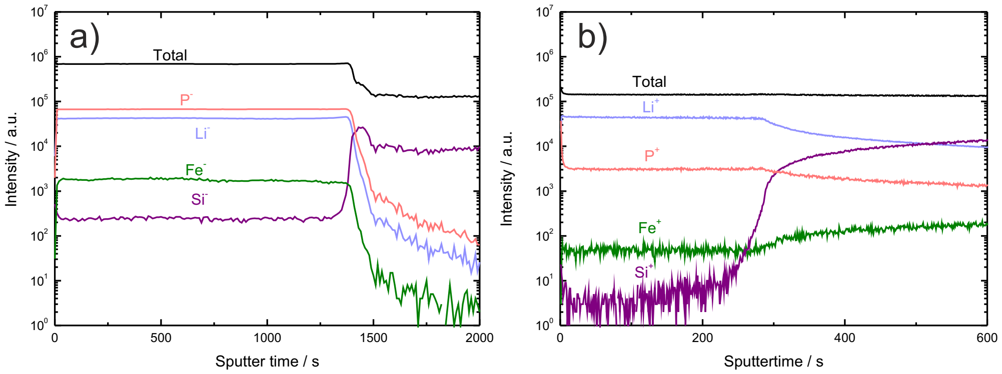

Figure 12: SIMS depth profile of a "LiPON" thin film deposited with different machine setups on float glass. The early samples a) show significant iron impurities (measured in negative mode) after the setup was changed b) only a base level of iron is detectable (measured in positive mode to increase iron sensitivity by Matthias Geiß). (Bi^+ 25kV analysis beam (1 pA), Cs^+ 1kV sputter beam (130 nA), $m/\Delta m = 6000$ for $m = 55.84$ (iron), 50 µm · 50 µm analysis field)

The iron impurities necessitated a reconstruction of parts of the sputtering setup and therefore in the intermittent time the sputtering setup of the physics department (AG Meyer/AG Polity) was utilized. This is the reason two different machine parameters for the "LiPON" deposition are given in the experimental part. The "LiPON" produced with their setup and later on our own machine after the necessary changes were implemented did not show the same impurities as is evident in fig. 12b and the efficiency of the produced LTO thin film cells was no longer hindered by the solid electrolyte. The samples show only a base level of iron which can be explained by the increased sensitivity for iron when measuring in positive mode. The signal is comparable but slightly less than measured inside the glass substrate. Further negative impacts on the cell performance by the choice of the substrate will be discussed in depth in the impedance characterization.

10.3 Finalized setup and properties

The performance of the final cells used for most of the impedance characterization is depicted in fig. 13. The data depicts a typical experimental setup in which the cells were cycled with 3.5 µAh/cm^2 for five cycles to equilibrate the cell chemistry before an additional five cycles with intermittent impedance measurements were measured. The equilibration assured that no early cycle irregularities were measured in the impedance. The growth of interphases or formation of space charge layers is possible in these cycles. Instead the behavior of the cell under stable conditions could be probed in the impedance cycles. Impedance cycles were measured by charging and discharging like in the first cycles but dividing the charge and discharge cycles into multiple steps with interjected

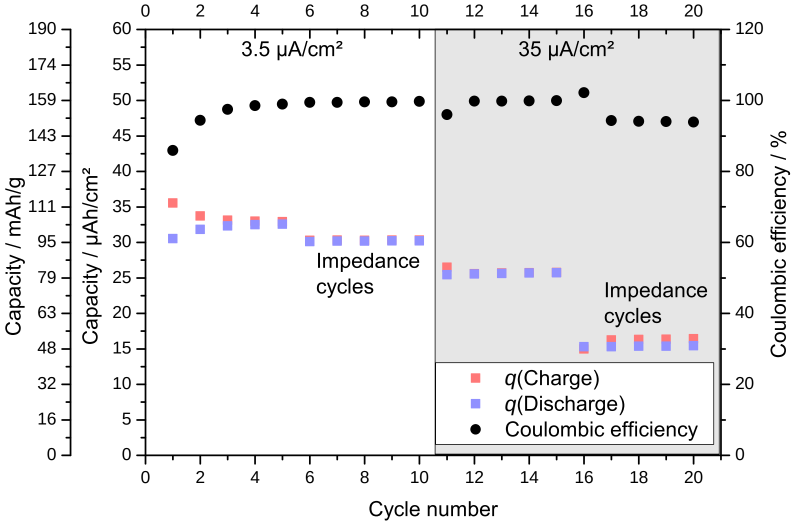

Figure 13: Cycling data of the final cells used for most of the impedance characterization. The typical experiment is shown where the cells were cycled at 3.5 µA/cm^2 for five cycles before cycles with intermittent impedance spectroscopy were measured. Additionally the experiment repeated with 35 µA/cm^2 is given.

impedance measurements. Since the cycling was performed galvanostatically this allowed for the charge inserted or extracted between each impedance measurement to be controlled through the time for each step. As can be seen when comparing the data to earlier results the efficiency is now greater than 95 % after the third cycle with a somewhat lower efficiency during the first cycles that can be explained by equilibration processes mentioned above. The high efficiency further indicates that the main problem of the earlier experimental setups was the electronic conductivity of the electrolyte.

The cell performance is generally somewhat lower in the impedance cycles since the cell currents are no longer controlled and partial charging and discharging occurs due to the voltage amplitude necessary for the impedance measurement. This effect is more pronounced when the cycling current is increased. Since the impedance measurement requires a fixed amount of time to measure the necessary frequencies (roughly 7 minutes with the utilized settings) the proportion of galvanostatic cycling time versus impedance measurement is skewed towards the latter for increased cycling currents i.e. a larger percentage of the overall cycling experiment is no longer under galvanostatic conditions. The data shows a reversible capacity of about 32 µAh/cm^2 after the initial equilibration (about 100 mAh/g) which equates to ca. 57 % of the theoretical capacity. The capacity is reduced by about 20 % down to roughly 25 µAh/cm^2 when the cycling current is increased to 35 µA/cm^2. The overall rather low capacity of the cells is partially caused by the calculation of the specific capacity. Since measuring thickness of each individual film was not feasible due to the films being further processed (“LiPON” deposition) immediately to avoid surface degradation under environmental conditions, the film thicknesses were estimated from the deposition parameters. Initial screening of the deposition rates showed that the film growth was approximately 0.7 nm per pulse equating to about 700 nm thickness for the typical 10000 pulses used. Note here though that a variation of about 50 nm can be expected even for films deposited identically. Further uncertainty is introduced into the capacity estimate by the nature of the lithium anode. As mentioned in the experimental setup the Li foil was pressed mechanically onto the electrolyte with a diameter of 6 mm. While the foil is pressed by a spring inside the cell complete coverage of the surface is not guaranteed. The estimation for the variation in contact area is about 10 %. The final factor necessary for the calculation of the specific capacity is the density of the film. For this the density of the bulk material was assumed since the film did not appear to be porous but the density of the thin film might still vary slightly. Assuming again an error of about 10 % for the density this leads to a calculation error of about 37 % in the specific capacity of the thin films which is why they are only given as estimated values.

Fig. 14 depicts charge and discharge profiles of the final LTO cells at two different current densities. For the lower current density the overpotential of the cell is very small in the

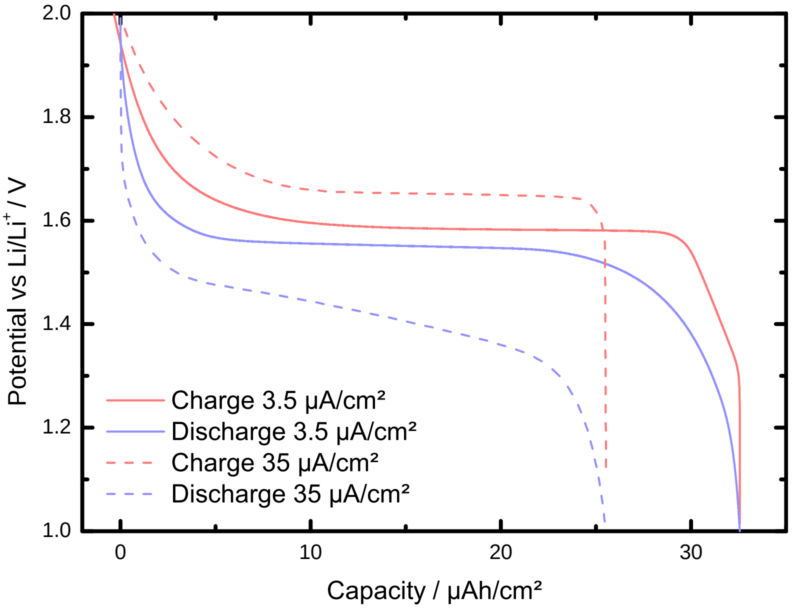

Figure 14: Charge and discharge profiles of the final cells. The profile is given for two cycling currents to emphasize the difference in kinetic behavior between the charge and the discharge cycle.

range of 20 mV - 30 mV with both charge and discharge profile exhibiting the flat voltage plateau that is typical for a two phase reaction. If the current density is increased the overpotential also increases to about 100 mV. As mentioned above the reversible capacity of the cell is also reduced under these conditions. Both these phenomena are expected side effects of an increased current density but additionally for this material there is a change in the kinetic behavior between the charge and discharge step. While the charge plateau increases in potential it retains its flat characteristic in contrast to the discharge plateau that exhibits a clear decline with the overpotenial increasing linear with the extracted charge. As outlined in section 6 this behavior in the literature is often attributed to a core shell mechanism of phase change that causes the individual conductivities of the phases involved to become limiting. The rising potential drop across one specific phase then increase the overvoltage. In the typical situation described in the literature the system consists of a particle where the outer shell is transformed into $Li_7Ti_5O_{12}$. As described in section 6 the lithium ion conductivity of the $Li_7Ti_5O_{12}$ phase is lower than that of the $Li_4Ti_5O_{12}$ phase so the resistance of this “outer shell” is increased. Since the “shell” keeps growing the resistance is further increased leading to a larger potential drop under galvanostatic conditions and therefore to an increase in overpotential. This behavior will be discussed in more detail in the impedance characterization since the considerations proposed for particle based electrodes in liquid systems are not directly applicable to the all-solid-state system. It is also notable that this behavior might change depending on the applied current since the phase separation of the material is kinetically induced during cycling. At lower currents the phase separation therefore might be less stabilized than at

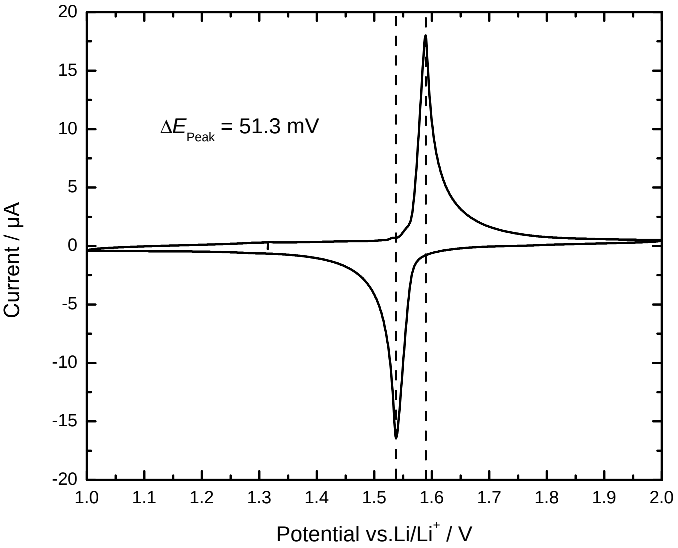

Figure 15: Cyclic voltamogram of the final cells measured with a scan rate of 0.05 mV/s resulting in the nearly ideal reversible redox couple around 1.55 V.

higher currents and its effects therefore lessened.

The cyclic voltamogramm of the final cells depicted in fig. 15 shows a nearly ideal reversibility of the Ti^{3+}/Ti^{4+} redox couple. The peak shape appears almost symmetrical for the anodic and cathodic process with a slight reduction of the peak current for the cathodic process with the cathodic peak current equating to 90 % of the anodic peak current. No additional processes are observed in the given voltage range. The reversible peak currents resulting from the measurement are in the range of 15 $\mu A/cm^2$ to 20 $\mu A/cm^2$ indicating that the typically utilized current density of 3.5 $\mu A/cm^2$ for the equilibration and impedance cycles are well within the reversible range of the cells which is a confirmation of the conclusions already drawn from the low overvoltage present in the cycle profiles and the high Coulombic efficiency of the cell.

In summary the preparation of well functioning Li/“LiPON”/LTO all-solid-state cells is possible with the utilized LTO deposition parameters (650 °C, 0.3 Pa O_2, WD 40 mm, 0.7 J/cm^2, 10 Hz, 10000 pulses). Most of the early difficulties in cycling the cells resulted from the experimental setup and not from the material properties of the thin film. The material itself shows good reversibility in cycling although the capacity of the cells might be rather low compared to the theoretical capacity. Due to the difficulty in accurately determining the amount of active material though the specific capacity of the cells has a relatively high inherent error of about 37 %. The influence of the phase change kinetics of the material is visible in the cycling data which necessitates an evaluation of the model of phase transition applicable to this system specifically. Some of the concepts described in this section will be explored in more detail during the impedance characterization since a lot of the overall cell behavior during cycling is connected to specific processes observed in the impedance and therefore have to be explained in context with the relevant data.

11 LTO impedance characterization

In order to characterize the exact processes responsible for certain cell behaviors and limitations electrochemical impedance spectroscopy was employed. The technique allows for all major impedance contributors of a cell to be monitored simultaneously if their time constants are sufficiently different from one another. Initially the technique was supposed to identify the charge transfer resistance between the cathode material and the “LiPON” solid electrolyte since this resistance is often claimed to be the major resistive contributor to the overall cell kinetic. LTO thin film cells were supposed to serve as a reference material since earlier work by Iriyama *et al.*[21,32,34] had already shown that the charge transfer resistance of the material was quite low. The material was therefore ideal to compare to the LNMO thin films that are expected to display a much higher charge transfer resistance. After initial measurements though it became apparent that the impedance spectrum for these all-solid-state cells was more complicated than typically observed for systems based on liquid electrolytes and a thorough exploration and definition of the spectrum and the processes involved was necessary. In order to adequately discuss the impedance characteristic of the system, the final result, the electrochemical equivalent circuit representing the cell processes, has to be given here initially to serve as a reference while the contributions of the individual processes and the steps in determining those are laid out.

Theoretically every process that happens inside the cell contributes to the overall cell impedance from typically major contributors like conduction through the solid electrolyte to small contributions like contact resistance between metal contacts. The nature of the final impedance spectrum depends on which of those processes are dominant (i.e. have the biggest contribution to the impedance) and how much they dominate the other processes. The contribution of a given process is both dependent on intrinsic process parameters (e.g. how high the conductivity of a material is) and extrinsic parameters (e.g. how thick a certain layer is). If extrinsic parameters are shifted enough, for example by using very thin films of a material, processes that are dominant under typical conditions might become less relevant and other processes might begin to influence the overall spectrum. An easy to grasp example is the difference in behavior between solid and liquid electrolytes. In liquid based systems the contribution of electrolyte conductance is often given as a preliminary resistor in the impedance evaluation while in a solid state system the electrolyte is mostly described as a semicircle due to its behavior similar to an RC or RQ element. There is of course no difference in the nature of the conduction between the two electrolytes as far as the equivalent circuit is concerned. The equivalent circuit representation of a liquid electrolyte also has to be a RC or RQ element in theory but since the electrolyte resistance is rather low and the capacitance of the idealized plate capacitor involved rather low too, the characteristic frequency of the process is shifted deep into the high frequency range

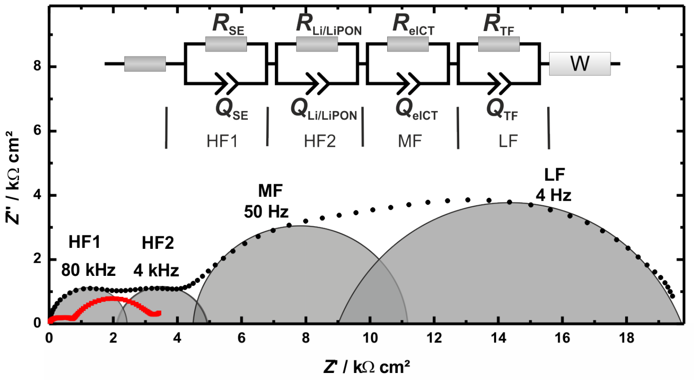

Figure 16: Equivalent circuit and typical impedance spectrum for a Li/“LiPON”/LTO cell deposited on a silicon substrate.

and therefore often impossible to measure with common equipment. What is visible in the impedance spectrum is basically the DC resistance of the solid electrolyte. Approximating this to a resistive behavior is fine for these systems, the problem arises when this kind of “rule of thumb” is applied to systems that are not well explored. Judging the impedance spectrum of a previously unexplored system both in materials employed as well as dimensions chosen by simply comparing it to the impedance characteristic of a system varying greatly in any of those parameters is not advised. In the case of the electrolyte conduction this is fairly straight forward because the scenario described above is common knowledge but every other process involved might become dominant in a new system and has to be considered while formulating an equivalent circuit and either ruled out or verified by either experimental results or logical consideration.

Fig. 16 depicts a typical impedance spectrum for a Li/“LiPON”/LTO cell deposited onto a silicon substrate. Four distinct processes/semicircles can be identified indicated by the grey areas. Note here that the semicircles shown only serve as a guide to the eye and do not represent the actual fitted semicircles. The visible processes can be grouped by the characteristic frequency at which they appear. There are two processes appearing at high frequencies of 80 kHz and 4 kHz labeled as high frequency process 1 (HF1) and similarly HF2, one process in a medium frequency range of about 50 Hz (MF) and one process in the low frequency range (LF).

As will be shown in the following chapter these processes represent:

HF1: The electronic conduction of the silicon wafer or in later samples not shown yet the ionic conduction of the solid electrolyte after the influence of the silicon substrate was eliminated.

HF2: The charge transfer resistance between the lithium anode and the "LiPON" solid electrolyte or the transport through a degradation layer forming at this interface.

MF: An electronic charge transfer resistance between the substrate material (mostly silicon) and the LTO thin film.

LF: The mixed conductivity of the LTO thin film.

Notably absent is the charge transfer between the LTO thin film and the solid electrolyte. As mentioned before it was already described by Iriyama *et al.*[21] that this resistances is quite small so it does not appear in this experimental setup. It can still be measured but this will be discussed in detail further below. Two of these processes are not often observed in liquid systems namely the electronic charge transfer to the thin film and the charge transfer between Li and the solid electrolyte which is often assumed to be minor. In the following it will be described how these processes were identified and how they impact the overall cell behavior.

11.1 The choice of substrate (HF1 and MF)

11.1.1 Substrate conduction and properties of the experimental setup

Since the impedance data was measured dependent on the state of charge (SOC) of the cell some processes are easily identifiable to be dependent on the state of charge while others appear not affected. Fig. 17 depicts the phase angle of the impedance measured for a Li/"LiPON"/LTO thin film cell for different states of charge. This is similar to a Bode plot depiction except the absolute value of the impedance has been omitted to not clutter the graph. The four processes visible in the Nyquist plot fig. 16 are marked and the arrows show the change in the data with decreasing state of charge since this particular data set is extracted from a discharge cycle. The data clearly shows that processes HF1 and HF2 are not affected by the state of charge of the cell indicating that these processes are likely not involved with the LTO thin film electrode since significant change of electrode properties with the state of charge are expected as outlined in section 6.

The fitted capacitances for process HF1 and HF2 are around $3 \cdot 10^{-11}$ F to 10^{-10} F and $2 \cdot 10^{-8}$ F respectively and also do not show any major change during cycling. Judging the capacitance values of unknown processes can be quite difficult since knowledge of the relative permittivity is necessary to calculate the ideal capacitance of a plate capacitor. Typically though the permittivity of a material is dependent on the measurement frequency and in this frequency range is mostly low due to slow dipole relaxation time in solids. Especially the capacitance of process HF1 is interesting since it is relatively low compared to the other processes observed. Considering that the relative permittivity cannot become less than 1 the only way to further decrease the capacitance of the imagined plate capacitor is by changing its geometry. Since the area for the system is ideally identical for all processes this means the length scale of the process i.e. the thickness of the layer involved is the only factor capable of reducing the capacitance to these low values. This is not entirely true since while the area of the active battery cell is governed by the size of the Li anode the electronic conduction through the silicon is not necessarily limited by the thin film setup on top simply because the electronic conductivity is relatively high and the silicon is roughly 500 times thicker than the remaining cell components. By calculating the expected capacitance of the different layers sufficiently low values of capacitance to explain process HF1 can only be obtained when using the parameters of the silicon substrate. Assuming the relative permittivity of silicon of 11.7 at ca. 1 MHz[99] the active cell area of 0.2827 cm^2 (ref. section 10) and the thickness of the silicon wafer (500 µm) the resulting capacitance is in the 10^{-12} F range which is two order of magnitude below the measured value. As mentioned though the area of the silicon is not necessarily limited by the Li anode so assuming the full substrate area of 1 cm^2 the capacitance calculated lies in the 10^{-11} F range so still not exactly as measured. Assuming reasonable parameters for the other layers involved it its not possible to reach this low value range by calculation

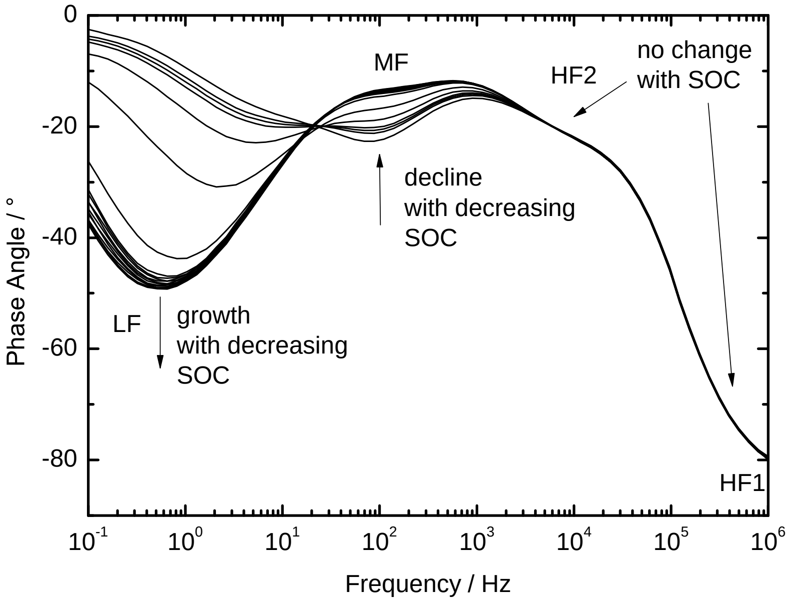

Figure 17: Phase angle of the impedance measured in dependency of the state of charge for a Li/“LiPON”/LTO thin film cell on a silicon substrate.

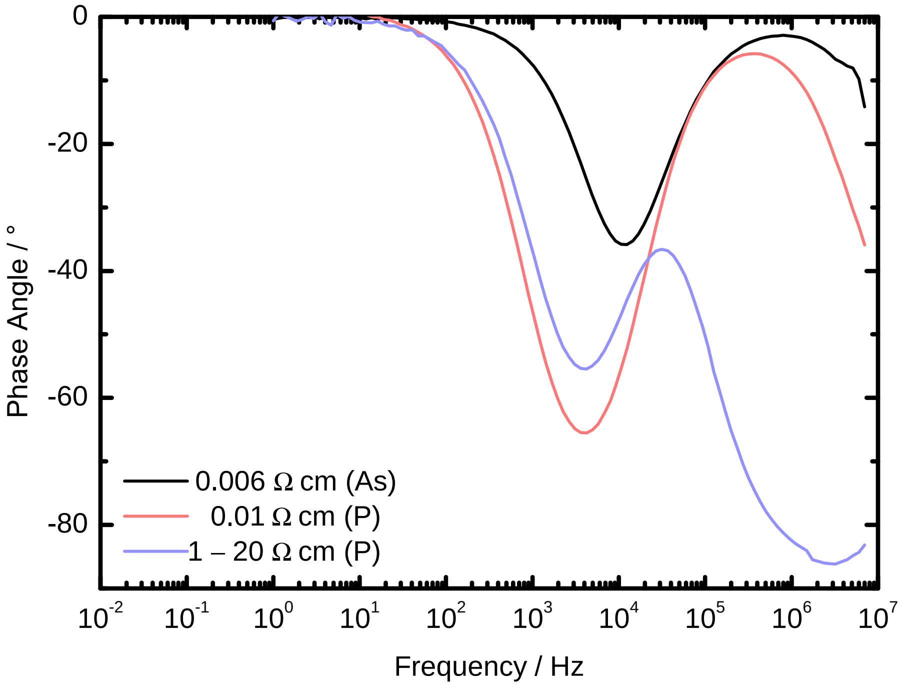

Figure 18: Phase angle of the impedance measured for silicon substrates with different conductivities in an identical cell setup to the all-solid-state cells. A 6 mm diameter gold electrode was used to contact the silicon surface.

for these layers either. Theoretical considerations for the capacitance are not enough to fully explain this process since the geometry of the silicon conduction is not sufficiently defined.

To verify if the silicon wafer is involved with process HF1 the layer was isolated in the setup by depositing a 6 mm diameter gold electrode (same dimensions as the active are in the all-solid-state cell) directly onto different silicon substrates and then measuring within the same cell setup.

Fig. 18 depicts the phase angle of the impedance measured for these samples. Silicon wafers with varying conductivities were chosen and the specific resistance as well as the dopant element is given in the graphic. Two processes can be identified in these measurements with one process appearing at very high frequencies similar to process HF1 in the all-solid-state cell and another process appearing at slightly lower medium frequencies that has no readily apparent equivalent in the battery system. Referring to tab. 3, the first process scales in resistance according to the conductivity of the silicon wafers utilized while the capacitance remains unchanged (considering the confidence in fitting this value). The second process scales in both resistance and capacitance according to the change in conductivity of the substrate. The behavior of the first process is in agreement with the process being the conduction through the silicon substrate. Furthermore the capacitance measured is about the same as the capacitance measured for the all-solid-state cell. The

Table 3: Fitted values for resistance and capacitance for samples on silicon substrate depicted in fig. 18.

Fitted parameters for the mid-frequency process

Wafer Type	Resistance / Ohm	Capacitance / F
0.006 As	131.2	$2.7 \cdot 10^{-7}$
0.01 P	2301.2	$8.1 \cdot 10^{-8}$
1-20 P	75537	$2.1 \cdot 10^{-9}$

Fitted parameters for the high-frequency process

Wafer Type	Resistance / Ohm	Capacitance / F
0.006 As	42.8	$1.1 \cdot 10^{-10}$
0.01 P	111.1	$1.8 \cdot 10^{-10}$
1-20 P	6714.1	$2.3 \cdot 10^{-10}$

resistance measured for this process is higher than expected considering the specific resistances given for the silicon substrates. Fig. 19 explains this behavior. Depicted is the same experimental setup as in fig. 18 but for two identical silicon substrates. One of the substrates was fixed with silver paste to the steel cell to improve the contact between silicon and the cell housing. The resistance of the high frequency process is visibly reduced and the capacity measured now lies in the range of 10^{-11} F as would be expected through calculation for the silicon conduction. This indicates that the contact between the silicon and the measurement cell is poor under typical experimental conditions which is probably related to the roughness of the unpolished side of the silicon substrate that is in contact with the steel casing. The poor contact causes the area of the electronic conduction to be ill defined as well as increasing the measured resistance of the setup explaining the inconsistency of the values obtained by impedance spectroscopy to the values theoretically expected. The poor contact was one of the major reasons pure silicon was no longer used as substrate material in the later all-solid-state cells since even with the silver paste the resistance is still not as expected.

The second process visible in the medium frequency range in fig. 18 and fig. 19 can be attributed to the electronic charge transfer between silicon and the gold electrode or more precisely the silicon and varying metal contact. The process has a capacitance orders of magnitude higher than the high frequency process indicating that it is probably a interface process. Both the resistance and the capacitance scale with the conductivity of the silicon. For the charge transfer or contact resistance it is expected to occur across the space charge layer forming in the semiconductor in contact with the metal when a potential is applied or that exists purely based on the contact potential. The width of this space charge layer is inversely proportional to the charge carrier density of the semiconductor and therefore indirectly to the conductivity. In the data a decrease of capacitance

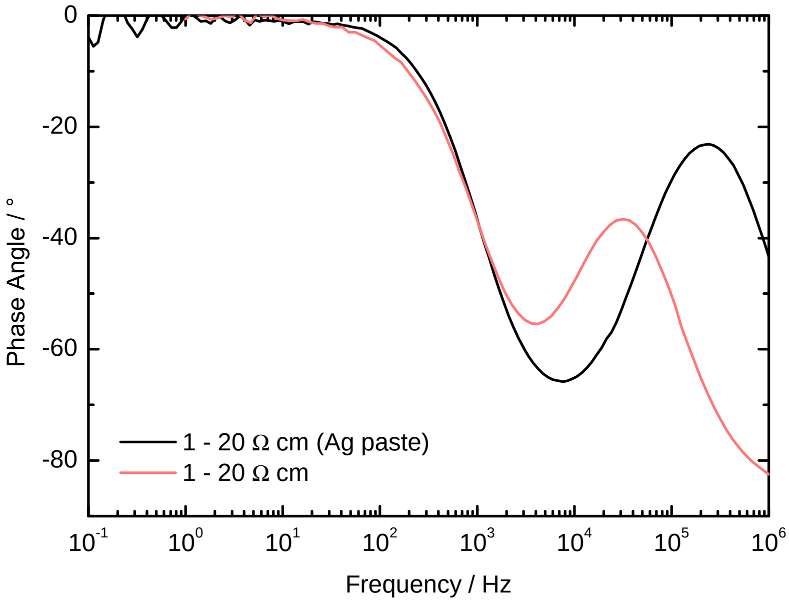

Figure 19: Phase angle of the impedance measured for two silicon substrates contacted via gold electrodes in the typical cell setup. One sample was fixed inside the cell with silver paste to improve the contact between the steel cell and the silicon.

for the process with decreasing silicon conductivity is visible due to the space charge layer becoming wider and therefore the length of the imagined plate capacitor becoming longer, decreasing the capacitance.

In theory more than just the silicon gold contact could be relevant since the silicon is also in direct contact with the steel cell and, in case of fig. 19, silver. Indeed the process changes when silver paste is used which is not expected if the process was purely located at the gold/silicon contact since this contact should remain unchanged. In reality this process is probably a combination of the different contact phenomena with the gold/silicon contact likely being the major contributor and the steel/silicon contact being less important since the process is not directly visible for the all-solid-state cell where the steel/silicon contact is still present. Note here that an influence of the steel/silicon contact on process HF2 was never completely ruled out in this thesis but results shown further below strongly indicated the prevalence of the Li/“LiPON” contact in this frequency region. This uncertainty though is another reason why silicon is not a suitable substrate for the impedance analysis of all-solid-state cells.

11.1.2 Substrate contact behavior

Returning to the impedance data shown in fig. 17 process HF1 can now be identified as the conduction through the silicon wafer. Suspecting the influence of the substrate on process HF2 too the Li/“LiPON”/LTO cell was deposited onto a silicon wafer with higher conductivity. Fig. 20a depicts this cell. As suspected process HF1 has a significantly reduced resistance due to the higher silicon conductivity so the phase signal at the high frequency region is reduced. Process HF2 is difficult to discern since the neighboring HF1 process was reduced in size but is still present as a shoulder in the signal. In the fitting data the process appears as before so the change in substrate seemingly has no or a very minor influence on process HF2. Looking at the data though the process in the medium frequency region now appears to be influenced by the substrate change. While the process showed a strong dependence on the state of charge in fig. 17 it now shows a much lower dependence on the SOC and also has a lowered resistance in general. Comparing this with fig. 20b the process MF now has completely disappeared. Fig. 20b depicts the impedance of a battery cell deposited onto the standard silicon wafer (20 Ω cm) but with a Ti/Pt metal layer between the silicon and the battery. Process HF1 is increased for this system again since the silicon has lower conductivity and process HF2 appears as before unchanged by the variation in substrate. Since process MF clearly shows dependence on the SOC as well as on the electronic properties of the substrate material it has to be located at the LTO/substrate interface. The capacitance values for this process are in the range of 10^{-8} F further indicating that this is an interface process. The electronic charge transfer between the thin film and the substrate seems to be the most reasonable explanation for this process.

As described in section 6 LTO undergoes a change in electronic conductivity during charge and discharge but in its charged state ($Li_4Ti_5O_{12}$) it is a semiconductor bordering on insulating behavior. In contact silicon and LTO are therefore expected to form a heterojunction with varying activation barriers depending on the degree of lithiation of LTO since the Fermi energy in LTO changes. For the lithiated phase it is expected that the Ti $3d$ con-

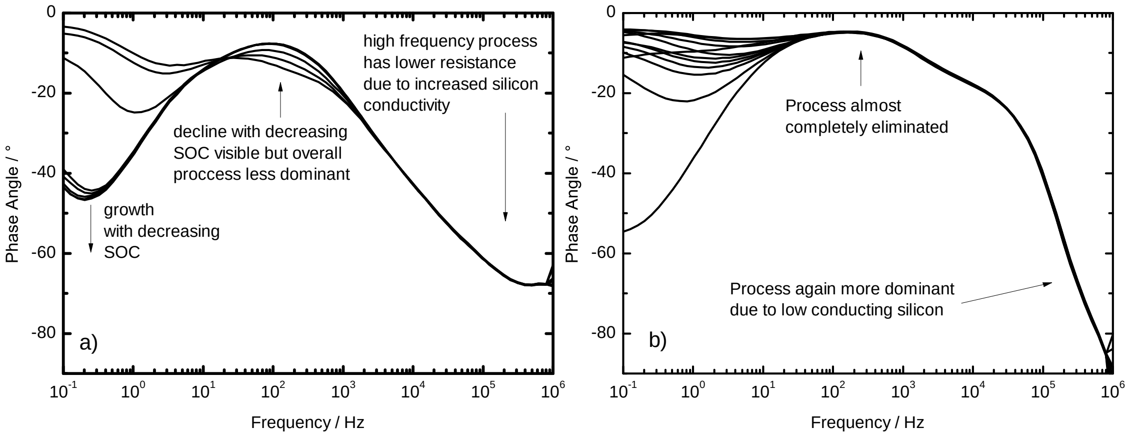

Figure 20: Phase angle of the impedance of a Li/“LiPON”/LTO cell measured on a silicon substrate with specific resistance of 0.006 Ω cm (As doped) (a) and deposited onto standard silicon with a Ti/Pt metal layer between the silicon substrate and the battery cell (b).

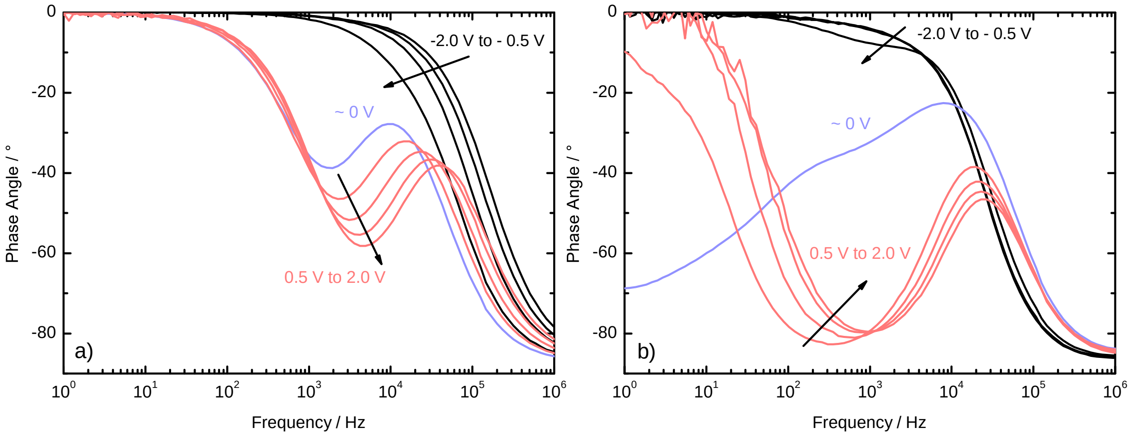

Figure 21: Polarization measurements of the electronic contact behavior of a) gold deposited on a pure Si wafer and b) gold deposited on a LTO thin film on top of a Si wafer. The process in the medium frequency range only appears when positive potentials are applied.

duction band overlaps with the Fermi level and therefore the band gap disappears and the material reaches very high electronic conductivities. Since the lithiation states at the interface and therefore the electronic structure is not exactly known for most of the battery cycle it is difficult to formulate a band model of the contact. Wu *et al.*[71] described similar problems in their work for the LTO contact with conductive carbon additives.

Fig. 21 depicts the phase angle of the impedance measured on Si/Au and Si/LTO/Au samples at varying external potentials with the gold electrode being the reference electrode at 0 V. For the Si/Au sample fig. 21a the process in the medium frequency range only appears when positive potentials are applied and the local minimum shifts towards higher frequencies while the area of the feature increases. If the process is attributed to the band transfer between silicon and gold this would indicate an increase of the band difference between Si and Au since the resistance of the process increases (larger area). The shift towards higher frequencies can only be explained by a decrease of capacitance which would result from a widening of the space charge layer. The fact that the process only appears in one direction of net electron transport strongly indicates that this process is a band transfer process.

For the Si/LTO/Au sample fig. 21b a similar result is obtained with the medium frequency process only being visible at positive potentials but the resistance of the process is much higher leading to an increased area for the visible feature in the phase angle plot. The frequency shift of this sample is not as readily explained as for fig. 21a since the resistance decreases and therefore might cause the high frequency shift. Fitting of the data is inconclusive due to the quality of the data (difficulty in measuring high impedance samples) but it indicates that no significant capacitance changes occur. Overall the process occurs at slightly lower frequencies than the Si/Au contact and therefore matches the observed MF process for the full cells much more closely. The system in this case is more complicated since now both the Si/LTO and the LTO/Au contact have to be considered. Considering the equilibrium work functions of the materials involved (about 4.8 eV for Si[100], 5.3 eV for Au[100] and around 6 eV for LTO (derived from density of states plots[67,70,101]) silicon and gold can be considered rather similar when compared to LTO for this simple argument (in respect to the phenomenological effect of both work functions being lower than the work function of LTO and therefore the band distortion occurring in similar ways). Since the charge carrier density in the conduction band of LTO is very low due to the high band gap (approx. 3.8 eV[67,70,101]) it is assumed that a majority of the band distortion occurs in the LTO. In this case the energy diagram is similar on both contacts under equilibrium conditions for the Si/LTO/Au contact due to the similar work functions of Si and Au in relation to LTO. It is not readily apparent why the medium frequency process is only visible at positive polarization since upon reversal of the polarization in theory band transfer limitations of one contact should be mirrored by the other contact in this configuration. The limiting contact at positive polarization should be the Au/LTO contact while at negative polarization the Si/LTO contact should be limiting. In reality though as mentioned before the applied potentials at the interfaces are unknown and therefore the position of the individual bands at the interface is unknown so it is not possible to determine from this measurement if the observed process is the Si/LTO or the LTO/gold contact. Furthermore the Si surface might be covered by a thin oxide layer changing the work function properties at the interface further. In full cell application a applied potential difference between LTO and silicon does not necessarily exist since the cell potential difference exists between lithium and LTO and is not artificially applied at the electrodes. Silicon can be assumed to be at the same external potential as the LTO electrode and only the equilibrium band difference is important. Since the impedance measurement probes both negative and positive current flow directions due to the sinusoidal excitation signal a barrier existing only in one direction will still be visible in the data. Unfortunately the potential dependence of the contact in a full cell cannot be measured in both polarization directions because if the cell is polarized to 0 V or even negative potentials lithium is deposited on the cathode side leading to fast dendrite growth and short circuiting of the cell. The potential dependence is therefore limited to the window given by the charge/discharge chemistry and simultaneously masked in that region by the property changes of LTO.

11.1.3 Beyond silicon substrates

The points mentioned above serve to illustrate why a detailed description of the electron transfer is difficult and cannot conclusively be given in this thesis. Since all of the observed band transfer phenomena appeared around the same frequency range and a clear

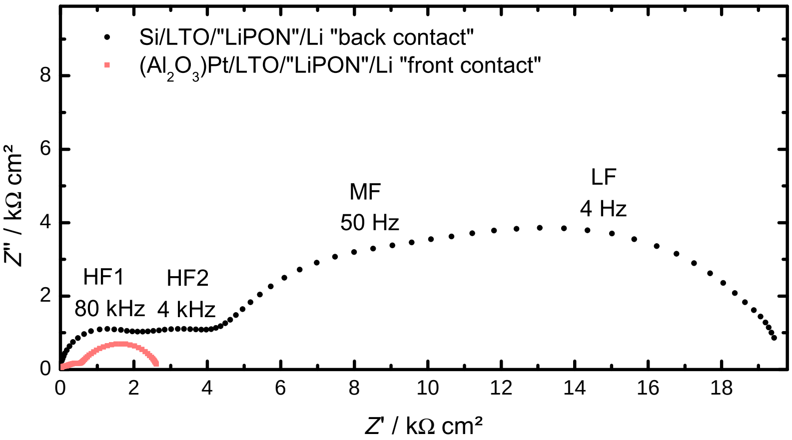

Figure 22: Nyquist plots of two identical LTO all-solid-solid-state cells on different substrates and with different contact setups. A large reduction of overall resistance is achieved by eliminating the poor Si mechanical contact and the MF process is eliminated due to the avoidance of the Si/LTO electronic contact.

connection between both SOC and electronic properties of the substrate could be measured the conclusion that this process is indeed the electron transfer substrate/LTO was drawn despite the details of the process remaining undefined. The process is inversely proportional to the electronic conductivity of the silicon substrate or more precisely to the charge carrier concentration yet even in the highest doped substrates the process could not be eliminated. Substituting a metallic contact layer (Ti/Pt) can reduce this resistance and in theory an ohmic contact is expected between Si and Ti due to the work function of Ti (ca. 4.3 eV[100]) being smaller than of silicon (ca 4.8 eV[100]). Note that this is not the case for platinum (approx. 5.6 eV[100]) and is another reason beside the alloying behavior it should not be used directly on silicon. Due to the many processing steps involved in producing a full thin film cell the ideally expected contact behavior of Si and Ti is not guaranteed. Considering the other problems silicon as a substrate and current collector already showed it was discontinued as a substrate for further cells. The substrate was changed to nonconducting sapphire and YSZ in order to retain the smooth surface offered by single crystal substrates.

Fig. 22 depicts the change in overall impedance achieved when not utilizing silicon as substrate material. The resistance of every cell process is reduced due to a better mechanical contact between the Pt thin film layer and the metallic cell tab (“front contact”) as opposed to the Si wafer and the steel cell housing (“back contact”) that essentially reduces the geometrical cell area. Furthermore the MF process is eliminated from the impedance by the direct contact of Pt and LTO and only the LF process remains. The high frequency region remains seemingly unchanged which is surprising considering the process HF1 was attributed to the silicon conduction before but silicon is no longer present. As mentioned in the initial process overview the lithium conduction through the solid electrolyte appears in the same region as the silicon conduction. This is readily apparent when fitting the impedance data. The formerly very low capacitance of process HF1 (due to silicon being rather thick) is now increased about two orders of magnitude to the order of 10^{-9} F to 10^{-8} F which matches the geometrical conditions of the solid electrolyte with a thickness of 1 µm to 1.5 µm and an assumed relative permittivity of 20 to 30.[102] The resistances measured for this process across all samples studied varied between ca. 150 Ω cm and 500 Ω cm which translates to a lithium ion conductivity of $3 \cdot 10^{-7}$ S/cm to $1 \cdot 10^{-6}$ S/cm which is the typical range expected for the electrolyte according to the literature.[3,44,103–108] Process HF2 remains largely unchanged except for the already mentioned reduction in overall resistance it shares with the other processes indicating that the process is not related to the substrate. The discussion of process HF2 will be given after the remaining processes are discussed since its definition is largely based on the exclusion of other possibilities.

11.2 The LTO thin film and its phase transition (LF)

The process in the low frequency region is influenced by the SOC and is the most dominant out of all visible processes indicating a connection to the changing cathode. Two processes are likely to be strongly dependent on the cathode properties, the charge transfer at the LTO/“LiPON” interface and the Li ion conduction through the LTO thin film. Fig. 23 depicts the fitted resistance values of process LF plotted versus the cell potential which indirectly represents the state of charge for LTO films with different film thicknesses. It is apparent that the overall resistance of the process scales with the thickness of the LTO film and therefore the process does not represent the charge transfer at the interface since that process is not expected to be dependent on the film thickness.

The apparent conductivities derived from these values in combination with the film geometry are in the order of 10^{-12} S/cm for the fully discharge material (1.0 V) to ca 10^{-10} S/cm for the fully charged phase (2.0 V). The change of the apparent conductivity is similar to the change expected in the diffusion coefficient for the phase transformation between $Li_4Ti_5O_{12}$ and $Li_7Ti_5O_{12}$ with the spinel phase $Li_4Ti_5O_{12}$ (charged phase) having a higher diffusion coefficient and the rock salt phase $Li_7Ti_5O_{12}$ (discharged phase) having a lower diffusion coefficient. This behavior also matches the data depicted since the apparent conductivity is lower in the discharged phase indicating that the ionic conduction is the main limiting factor to the apparent conductivity. The electronic conductivity for the discharged phase is expected to be orders of magnitude higher than the results shown here so for the $Li_7Ti_5O_{12}$ the ionic conduction is expected to be rate limiting.

For the $Li_4Ti_5O_{12}$ phase though in the fully charged state it is not clear if the limitations arise from the ionic conduction alone or if the electronic conduction influences the apparent conductivity in this SOC region. For the 700 nm and 100 nm sample a dip in conductivity can be observed towards the upper potential limit of 2.0 V which might arise from the electronic conductivity of the spinel phase (expected to be 10^{-11} S/cm) becoming dominant in this region. For the 1400 nm film this effect is not observed which can possibly be explained by the lower utilization of the thin film which is an often observed phenomenon with thicker “thin” film electrodes. The residual $Li_7Ti_5O_{12}$ phase inside the thin film might act as a electronic conduction agent similar to carbon in conventional battery electrodes and prevent the low electronic conductivity of the spinel phase to become relevant until all remaining phase domains have been transformed.

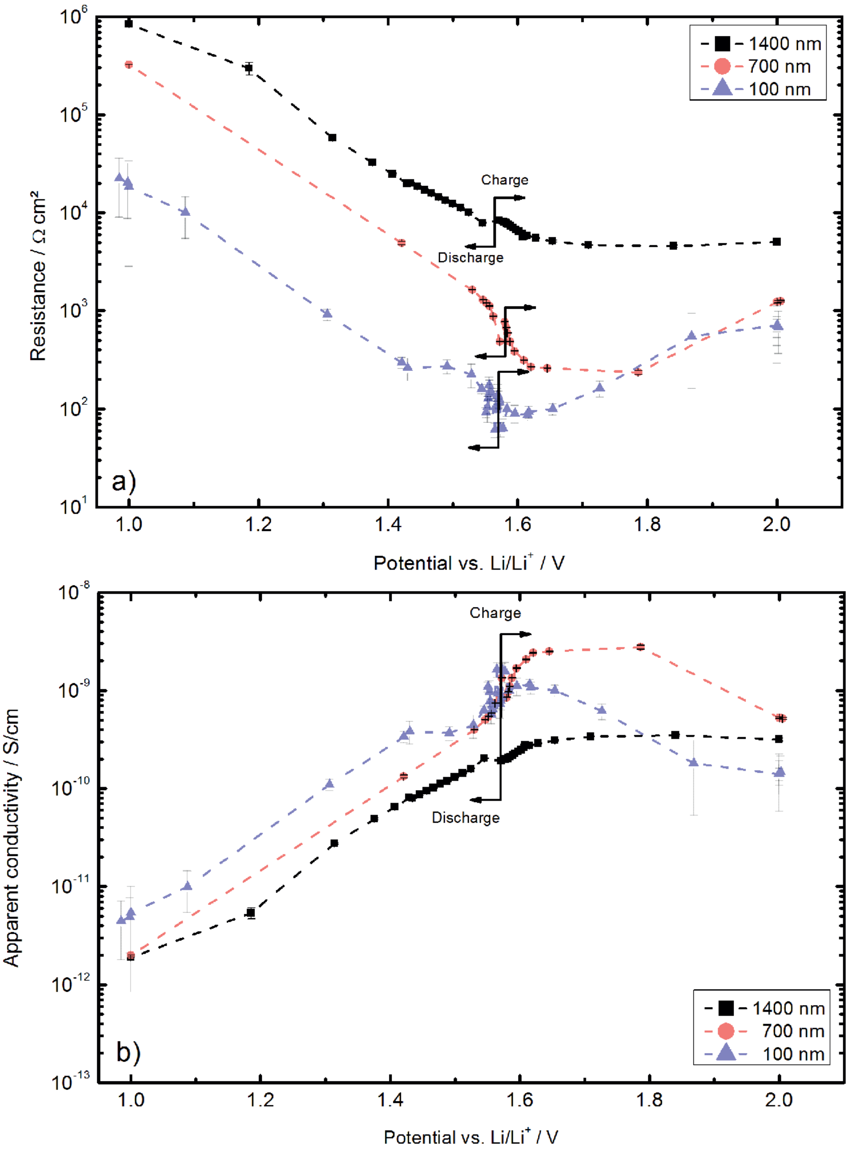

Figure 23: a) Resistance of process LF plotted versus the cell potential (SOC) for LTO thin films with different film thicknesses as well as b) the derived apparent conductivity for the thin films.

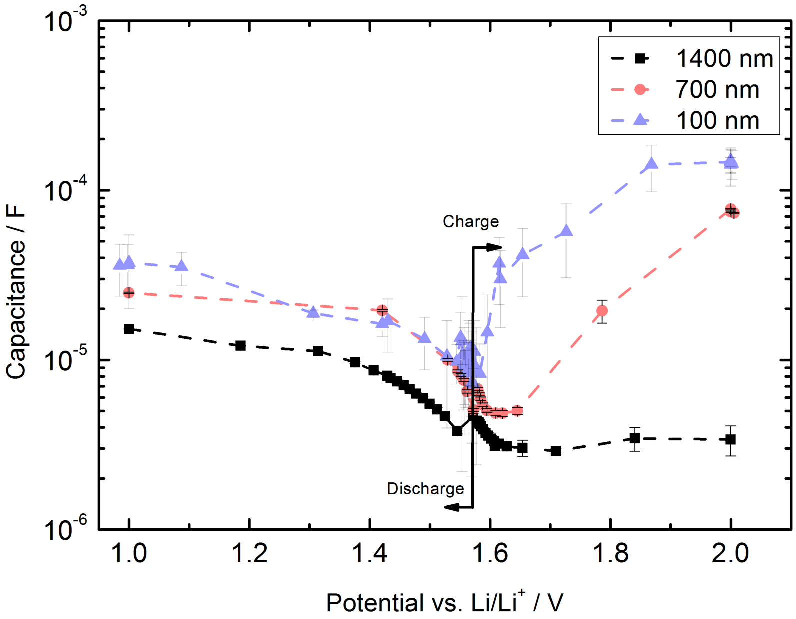

Figure 24: Capacitances for the LF process for LTO thin films with different film thicknesses.

11.2.1 Evaluation of a core shell transition mechanism

Since the resistive behavior of the thin film seems to arise solely from the properties of the two phases involved more detailed conclusions about the phase transformation can be drawn by analyzing the data. If a model similar to the often used core shell model for liquid electrolyte systems is to be applied to a two dimensional layer system the phase transition would be expected to proceed via a phase boundary that forms either on the electrolyte or the substrate interface and then proceeds to move through the thin film. In this model the resistance of the process is expected to scale linear with the thickness of the limiting phase layer i.e. the spinel phase in case the electronic conduction is limiting or the rock salt phase if the ionic conduction is limiting. It is also possible that at a certain SOC the limiting process switches since the non limiting layer becomes so thick that its resistance becomes dominant. The ionic conductivity of the rock salt phase is not known directly but if it is reduced like the diffusion coefficient by two order of magnitude when compared with the spinel phase it would be in the order of 10^{-11} S/cm to 10^{-9} S/cm. With both limiting conductivity values being rather similar, the individual layer thicknesses might indeed be relevant for the dominant conduction. There are multiple details though that challenge the validity of applying this model to the system.

Fig. 24 depicts the fitted capacitance values of the LF process for LTO thin films with different film thicknesses plotted against the cell potential. Some inconsistencies are apparent when considering the 3 logical cases for a growing layer mechanism a) the ionic conduction is limiting, b) the electronic conduction is limiting and c) the dominant con-

duction changes during layer growth.
In case a) the capacitance of the LF process would be at its maximum while the ionic transport limiting layer is thinnest i.e. near the fully charged state or close to 2.0 V. This seems to be the case for the 700 nm and 100 nm film but the capacitance would also be expected to change linear with the state of charge increasing the further the cell approaches the fully charged state. This is not the case since the capacitance only rapidly increases towards the end of the charge cycle while it remains mostly stable or even decreases in earlier parts of the cycle. Note here that a majority of the SOC change occurs around 1.55 V and the data points depicted above approx. 1.6 V and below 1.5 V already represent SOC values of above approx. 90 % and below approx. 10 % respectively. Furthermore, since both charge and discharge cycle are depicted in fig. 24 the data points directly adjacent to the inserted arrows represent the start of the charge cycle and the start of the discharge cycle and therefore have drastically different electrode compositions from very lithium rich (start charge cycle) to very lithium deprived (start of the discharge cycle). The capacitance difference of the ionic limiting layer should therefore be highest at these two points yet the values are almost identical. The same argument applies when the electronic conduction is limiting but is of course mirrored. The $Li_4Ti_5O_{12}$ phase should be limiting therefore capacitance should be highest at 1.0 V and increasing during the discharge cycle (which is the case in the data) but again start of charge and discharge cycle should be the points of biggest difference.

In case of a change in dominant conduction it would be expected that the capacitance increases initially (since the limiting layer shrinks) and then starts to decrease again (when the new dominant layer continues to grow) which is observed in none of the samples. None of these cases reflect the measured data satisfactory and the model seems to be inconsistent with the data. Note here though that the change in capacitance is not only related to the expected change in geometry but also to change in material properties. Since the capacitance of a plate capacitor is directly proportional to the relative permittivity it is an important value to take into consideration. For the spinel phase the relative permittivity is expected to be rather high in the given frequency range according to Ganesan *et al.*[109,110] (in the range of 10^6) which also explains the relatively high capacitance the LTO layer exhibits. In theory the capacitance derived from the given parameters would be expected to be even higher yet since the material probably does not exist in pure spinel form after the cell has been assembled and instead in varying degrees of lithiation in the $Li_{4+x}Ti_5O_{12}$ composition the value derived from the data is closer to 10^4 - 10^5 which is still quite considerable. The change in measured capacitance might simply arise from a change in permittivity when the electrode is transformed during cycling. No permittivity values for the $Li_7Ti_5O_{12}$ phase are reported in the literature so it is unclear how much the permittivity is expected to change. Even if the permittivity values were drastically different from one another the beginning of the charge and the beginning of the discharge cycle would still be expected to reflect this difference yet, as mentioned before, the capacitance is nearly identical.

Another detail questioning the growing layer mechanism is the electronic charge transfer process MF discussed in the previous section. This process is located at the LTO/substrate interface and is dependent on the material properties of LTO at this interface. If a growing layer mechanism was applied to the thin film the charge transfer resistance at the interface would be expected to change fast and drastically as soon as the contacting LTO phase changes so either at the start or at the end of the cycle depending on where (geometrically) the initial phase transformation in this model begins (determined by which conduction process is limiting). As can be seen though in both fig. 17 as well as fig. 20 the charge transfer resistance changes gradually across the cycle indicating that the interface contact changes across the entire cycle duration and not at a specifically determined point.

As described in section 6 the phase separation between the spinel and rock salt phase is thermodynamically unstable above 80 K but is typically induced kinetically during cell cycling causing the flat voltage plateau. Between 80 K and 300 K a solid solution with some nano domains between 1 nm and 800 nm are expected under reversible conditions. Since the cells in this thesis were typically cycled with currents of ca. 1/10 C to 1 C the rates might not have been high enough to kinetically stabilize the phase separation fully. Furthermore, the impedance measurements were taken during the cycle under potentiostatic conditions i.e. the current flow was not controlled and the film or parts of the film might have relaxed to the solid solution equilibrium state. Under the assumption that the phase transformation proceeds with a solid solution mechanism the data shown above seems more reasonable. The properties of the interface would be expected to change gradually as the phase composition of the solid solution shifts and with it the conduction properties of the material. A problem when discussing the data is that parts of the battery cycle are dominated by non ideal polarization phenomena towards the end of the respective cycle.

11.2.2 Solid solution transition

Until now the points of radically different electrode composition were always described as being at the start of the charge and discharge cycle but of course at the end of the respective cycles the composition difference is also maximized but mirrored. The two states are not easily comparable due to the way in which the experiment was carried out. To ensure that the first measurement point in a given cycle did represent the active state during cycling as close as possible some amount of charge has to be inserted in order to not measure the equilibrium state of a charged or discharged cell. Therefore the active cell state “at the start of the cycle” cannot be measured, only the state shortly after the start of the cell. For the end of the cycle polarization phenomena start to occur that cause the rapid increase in cell voltage. This is caused by parts of the cell being already fully transformed and the remaining current density being applied to a lower amount of active material causing higher overvoltages until the cell is fully transformed and capacitive behavior sets in. The latter case is further from the actual conditions of the majority of the cell cycle because the cell potential is further from equilibrium and current densities applied to the remaining active material are higher. In the data it is indicated that upon beginning of the charge and discharge cycle the solid solution is formed rapidly since vastly different compositions display similar properties. The solid solution then shows only minor property change with the SOC across a majority of charge insertion up to about approx. 90 % SOC. After that point properties begin to change rapidly, probably because the solid solution begins to collapse. Individual parts of the film are already fully transformed and exist in their respective phases. The parts that are yet to be transformed are cycled with higher current densities and therefore the kinetic formation of phase domains or the phase separation itself is promoted. The distribution of these regions is random across the film and not limited by a layer growth mechanism so not only the interfaces are affected. Considering the columnary structure of the electrode it is possible that individual crystals that span across the entire thin film are fully transformed at this point while others remain only partially transformed.

This is more likely for the thinner films and as can be seen in the capacitance plot they show an increase in capacitance towards the end of the charge cycle corresponding to the phase formation of the spinel phase with high permittivity. The thicker 1400 nm film is probably less utilized and therefore the percentage of material still in the solid solution phase transition is increased. The overvolage for this cell is higher due to the increased film resistance so equivalent cell potentials do not correspond to equivalent states of charge when compared to the other films. Either due to the lesser degree of phase transformation or the increased film thickness and therefore reduced influence of phase separated nano domains the behavior of the thicker film is more stable.

Another example of this behavior is depicted in fig. 25. Shown is the resistance of the LF process during cycling plotted against the cell voltage for multiple samples deposited with the same deposition parameters. All samples were deposited with 10000 pulses (except for sample 198 which features only 1000 pulses as a comparison) but between sample 185 and 187 a new target pellet was utilized. The old target pellet had at this point degraded and due to heavy surface damage introduced in the last few samples prepared on that

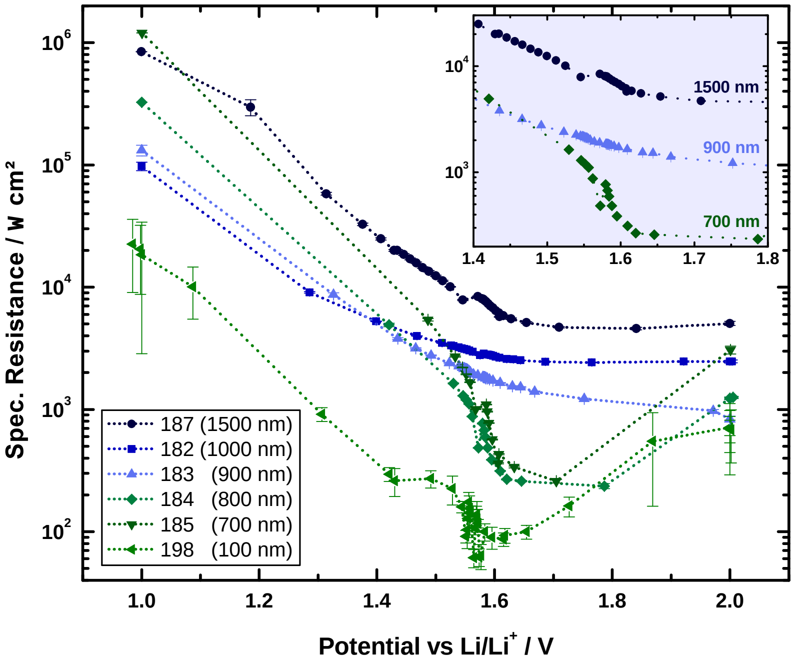

Figure 25: Resistance of the LF process for multiple different film thicknesses resulting from aging of the target pellet.

target the ablation rate started to steadily decline leading to a variation of film thickness. This is also apparent in the decrease in overall resistance measured which was also used to estimate the film thicknesses of these films since they were not measured individually due to samples prepared at the start and end of a target cycle life typically not being used for cell characterization.

As can be seen the resistive behavior around the equilibrium potential changes when the film thickness reaches a threshold of about 700 nm to 800 nm. For these films the resistance change is compressed into a smaller potential window due to the charge and discharge plateaus suddenly becoming rather flat i.e the measurement points are more condensed around the equilibrium potential. The corresponding region is therefore depicted in more detail in the inset for three selected film thicknesses. This is an indication of two phase behavior since the difference in resistance outside of the narrow range near the equilibrium potential is not too different to the slightly thicker films (accounting for the difference in geometry) so the sudden change around equilibrium potential indicates a change in transport. Reiterating though that for the thinner films the behavior at the substrate interface does not change this result is probably caused by the thin film dimension approaching the size region of the nano domains of phase separation. The film thickness of about 700 nm - 800 nm matches the estimate given by Wagemaker *et al.*[13].

In summary the conditions for cycling the LTO all-solid-state batteries in this thesis seem to be close to a switching point of mainly solid solution and nano phase domain controlled behavior. The model of a growing layer mechanism is inconsistent with the gradual change of the interface so if two phase separation occurs it is not in the form of two dimensional layers moving through the electrode. For intermediate potentials during cycling the cell probably exists in a state of solid solution majorly since heavily different compositions exhibit very similar resistive and capacitive properties. Individual phase domains distributed randomly across the film continue to grow though and start to influence cell behavior stronger the further the cut off potentials are approached since they become dominant across the film. This behavior is emphasized when the films are reduced in thickness since the domains are possibly stretched across the entire film thickness in this case. Conditions at the start of a cycle are not the same as at the end of the previous cycle i.e a near fully discharged cell at the start of the charge behaves different than a fully discharged cell near the end of the discharge. This indicates that the solid solution is formed rapidly once the phase transformation kinetic sets in and only dissolves once large enough parts of the material are no longer kinetically active and allowed to relax. In order to fully describe these phenomena though in-situ synchrotron measurement of LTO all-solid-state cells with varying film thicknesses would be necessary since the difference in the diffraction pattern between the spinel and rock salt phase is very minor and not visible with conventional XRD setups.[12,98] Neutron scattering to observe lithium positions would be difficult to carry out in-situ especially since the layer of interest is encased in other solids (substrate and electrolyte).

11.3 The Li/LiPON interface (HF2)

So far the discussion of process HF2 was avoided in order to first explain the reasoning behind attributing the other observed features to different cell processes. The process HF2 itself is difficult to characterize since in all variations of cells measured process HF2 was always constant and never changed with SOC, polarization, contact materials or other changes to the system.

Fig. 26 provides an overview over the range of capacitance observed for the different cell processes. As mentioned before the solid electrolyte has a relatively low capacitance due to the high film thickness in combination with the low to medium permittivity. The relative permittivity of "LiPON" is reported by Le van Jodin *et al.*[102] to be around 20 - 30 at 10^4 Hz which fits with the observed values for the capacitance considering the film geometry. The electrode film, despite having comparable film thicknesses (within an order of magnitude), has a much higher capacitance due to its higher permittivity (in the respective frequency range). The permittivity is about 4 to 5 orders of magnitude higher which matches the capacitance difference which is also 4 to 5 orders of magnitude higher.

The remaining process ascribed to the Li/“LiPON” charge transfer has a somewhat higher capacitance than the “LiPON” thin film, considering the degradation layer is stable and its growth self limiting the thickness is estimated to be in the 10 nm range.

The growth of this layer has been shown by Schwöbel *et al.*[28] as well as Wenzel *et al.*[111,112] for sulfur based electrolytes. Judging the permittivity of this layer is difficult. Under the assumption that the permittivity is comparable to the solid electrolyte the calculated capacitance values are already within the same order of magnitude as the observed values (about $7 \cdot 10^{-7}$ F). To achieve values closer to the observed results, assuming the geometry is fixed, the permittivity of the formed layer would have to be in the range of 4 to 6. To explain this one has to consider the composition of this layer. Schwöbel *et al.* demonstrated that upon contact with Li the “LiPON” solid electrolyte decomposes into mainly Li_2O, Li_3N and Li_3P. While the exact permittivity of the material composite is not known the individual components exhibit a somewhat lower dielectric constant as reported for “LiPON”. In particular the main component of the degradation layer, Li_2O exhibits a dielectric constant in the range of 2 to 4[113] which is close to the estimated value given for the interphase derived from the observed data. Since the interphase is not grown in a controlled manner exact values for the capacitance also might vary slightly from sample to sample depending on exact film thickness and geometry leading to different values for the dielectric constant. Considering these uncertainties discussing a deviation of a factor of about 2 to 3 in the observed dielectric constant versus the expected one from the literature values is not reasonable.

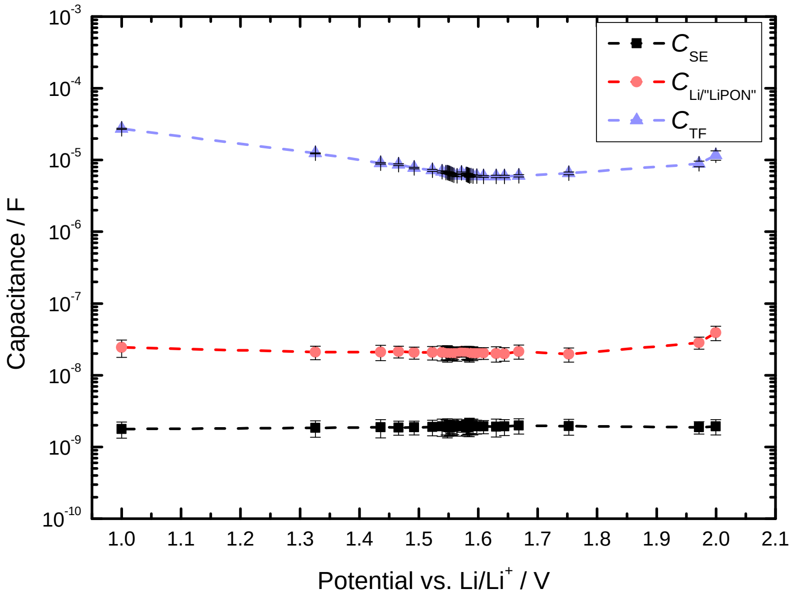

Figure 26: Capacitances for the different cell processes for a Li/“LiPON”/LTO/Pt cell in a “front contact” assembly. Visible are the solid electrolyte capacitance (C_{SE}), Li/“LiPON” charge transfer capacitance ($C_{Li/\text{“LiPON”}}$) and thin film capacitance (C_{TF}).

The resistance of this process is about the same as the remaining 1 µm to 2 µm of “LiPON”. Assuming again a thickness of the degradation layer of about 10 nm this indicates a reduction of conductivity of about 2 orders of magnitude to the range of 10^{-8} S/cm to 10^{-9} S/cm. While the ionic conductivity of Li_3N[114–117] and Li_3P[118] are expected to be even higher than the conductivity of “LiPON”, the majority component of the layer, Li_2O, has very low ionic conductivity at room temperature (in the range of 10^{-10} S/cm to 10^{-11} S/cm extrapolated from Biefeld *et al.*[119]). The presence of Li_2O can explain the very low conductivity of the interphase under the assumption that it forms the limiting component for ionic transport.

$$\mathrm{Li_3PO_{4\text{-}\mathit{x}}N_\mathit{x}} + (8-5\,x)\,\mathrm{Li} \longrightarrow (4\text{-}x)\,\mathrm{Li_2O} + x\mathrm{Li_3N} + \mathrm{Li_3P} \tag{3}$$

Equation 3 shows a possible summary degradation reaction for the solid electrolyte. As is apparent from the stoichiometry Li_2O is formed in relatively high excess since the amount of nitrogen in the material is typically low (x about 0.5 to 1.0). If a composite material is formed it is therefore unlikely that ionic transport can proceed in the Li_3P or Li_3N material without at least partial transport through the Li_2O phase. In the actual cell reaction that takes place it is probably necessary to distinguish between reaction of triple and double coordinated nitrogen structures in the “LiPON” phase. Schwöbel *et al.* described two different cell reactions for that case[28] but the authors also mention that these are only two of many possible partial reactions so instead here a summary reaction into the degraded materials is given.

In general the driving force for these reactions is thermodynamic since the Gibbs enthalpy of reaction is typically negative for these components. The degradation of the material in contact with lithium is therefore not a phenomenon of the electrochemical activity of the cell and is expected to always occur independent of other utilized cell components, especially the cathode. Schwöbel *et al.* also suggested that the interphase formation is likely self limiting which can be explained with the very low ionic and electronic conductivity values of the interphase that only allow for a rather thin interphase to form. This might be different if significant electronic conductivity was introduced into the solid electrolyte. As mentioned when discussing the electrochemical performance of early battery cells the “LiPON” initially deposited with our machine had significant iron impurities due to the sputtering setup and exhibited a significant electronic conductivity leading to the cells short circuiting. TOF SIMS depth profiles depicted in fig. 27 show the difference between two identical Li/“LiPON”/Glass samples where one sample was measured as fast as possible after lithium deposition (about one hour) and the other was aged after lithium deposition for a day before measurement (in glovebox atmosphere). In the non aged sample a distinct lithium layer is visible at the beginning of the depth profile although the signal

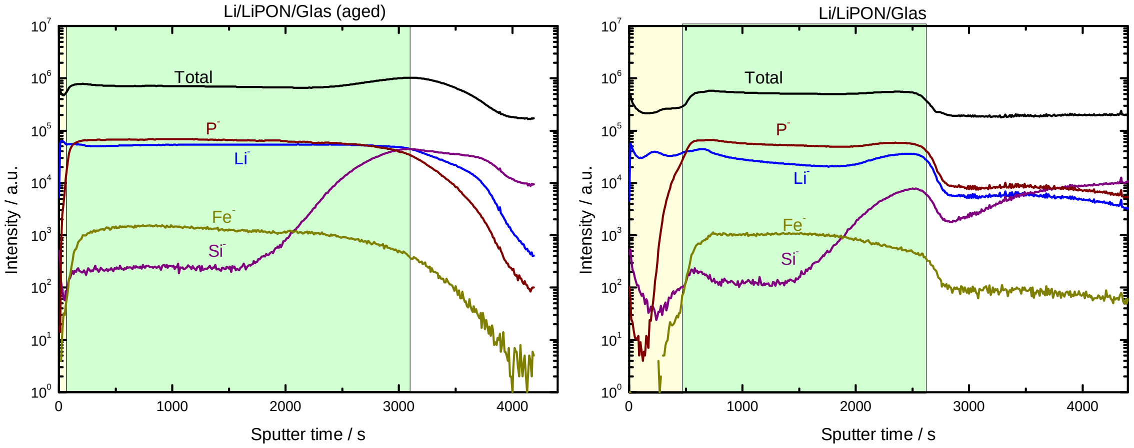

Figure 27: TOF SIMS depth profiles of two samples of LiPON with a Li layer on top, one sample was measured fresh after Li deposition (vapor deposition), one sample was aged for 24 hours after deposition and then measured. (Bi^+ 25 kV analysis beam (1 pA), Cs^+ 1 kV sputter beam (130 nA), negative mode, $m/\Delta m = 6000$ for $m = 55.84$ (iron), 50μm · 50 μm analysis field)

intensity is not stable in this region which might occur due to the on setting degradation reaction and the therefore introduced changes in the sputtering matrix. After aging this lithium layer is barely visible and seems to have been almost completely absorbed into the “LiPON” layer. This can also be visually verified in that the opaque lithium film on top of the translucent “LiPON” was no longer visible after that time and the sample appeared translucent again much like just the “LiPON” layer would.

The amount of lithium deposited (about 1 μm Li on top of 1 μm “LiPON”) was more than the amount needed to form the self limiting degradation layer of about 10 nm thickness. Correlating the sputter time directly with the film thickness is difficult due to the changes in the sputtering matrix. The lithium film for example appears thinner in the figure only because the sputtering rate in the material is higher than in “LiPON”. In the aged sample the “LiPON” film thickness appears roughly like the Li layer and the “LiPON” layer combined in the fresh sample but again this can only be interpreted as a tendency and not directly. Measuring the depth of the sputter crater was not possible since at the time there was no way to measure surface profiles under glovebox or vacuum conditions and the sample surface degraded under normal atmosphere. The information obtained from surface profiling therefore was not reliable. Distinguishing between components of the degradation layer and the “LiPON” film is difficult because similar ionic sputter species are expected to form. Differences might arise from the different sputter yields in the different phases due to matrix effects but none are clearly visible in the measurement which indicates that those either do not exist or that the lithium is distributed uniformly throughout the “LiPON” film. Since high electronic conductivity of the electrolyte is not tolerable in battery cells anyway the data just serves to indicate how readily the degradation between the two materials occurs if left unhindered leading to the full reaction of 1 μm lithium in only 24 hours.

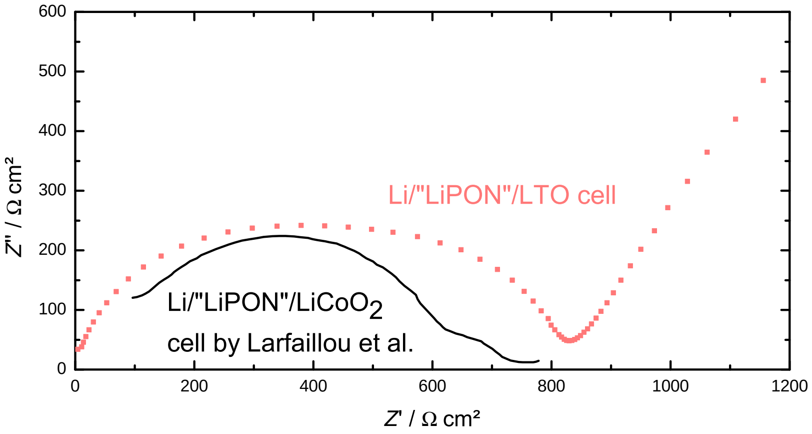

Figure 28: Nyquist plot of an example Li/“LiPON”/LTO cell from this thesis and data for the Li/“LiPON”/$LiCoO_2$ system from the literature. The data was extracted from Larfaillou *et al.*[26] and corrected by the cell geometry.

With the degradation of the “LiPON” occurring independent of the remaining cell setup and the resistance of the degradation layer being significantly higher than of the “LiPON” phase itself it is expected that a significant impedance contribution of this interphase should occur in all cells having the materials in direct contact. For very thin electrolyte films it is expected that their impedance response is completely dominated by the interphase layer while for thicker films the effect is lessened. Typically though “LiPON” is used in thin film cells with a film thickness of less than 10 µm so if the degradation layer is not present in the impedance data it has to be explained by another process dominating at this frequency region. This is important to note since for quite a long time “LiPON” was expected to be stable in direct contact with lithium so some of the results obtained in the literature might have to be reevaluated. The process might be masked by geometry effects in some examples but might have been misinterpreted in other works. A recent work by Larfaillou *et al.*[26] provides similar insight as this thesis for the Li/“LiPON”/$LiCoO_2$ system and the authors arrive mostly at the same conclusions. Fig. 28 depicts a typical LTO cell from this thesis (“front contact” on Al_2O_3/Pt) and data from Larfaillou *et al.* for the Li/“LiPON”/$LiCoO_2$ system. The data from Larfailou *et al.* has been extracted from the work and modified by the cell area to make the data more comparable.

The two semicircles in the high frequency area are comparable because they both arise from the “LiPON” conduction (1st) and Li/“LiPON” charge transfer (2nd) as is also noted by Larfaillou *et al.*. It is apparent that the resistance ratio of the two processes varies in the two systems. While in this thesis the two processes have roughly the same resistance, in the work of Larfaillou *et al.* the ratio is roughly 5 to 1 with the “LiPON” conduction having a higher resistance. This can be explained by the differences in cell setup. While the electrolyte layer in this thesis was about 1.5 µm in thickness in the work from Larfaillou *et al.* the thickness was about 2 µm to 4 µm. Due to the thicker electrolyte films the conduction through the layer has a higher resistance and therefore becomes more dominant while for the interphase layer no dependence on electrolyte thickness is expected. The overall lower resistance of both processes in the work of Larfaillou can be explained by a higher overall conductivity for the solid electrolyte used in their work and the fact that the cell geometry is not exactly determined in both systems (as mentioned previously).

The comparison of both works indicates that the data is consistent with the expectations arising from the model proposed in this thesis and by Larfaillou *et al.* which are identical for the high frequency range and only vary when discussing effects of the cathode. Also following the trends observed here it is estimated that the “LiPON” electrolyte conduction begins to dominate the high frequency range in such a way that the Li/“LiPON” charge transfer is obscured not before the electrolyte thickness approaches approx. 10 µm at which point “LiPON” as a “thin” film electrolyte is typically no longer useful. It is also important to note that even if the “LiPON” conduction is “dominant” this only means the charge transfer process is no longer easily visible in the data. It is of course still present underneath the conduction process and has to be considered while fitting the data unless an error is to be introduced. Considering these results it might be necessary to reevaluate data previously published in the field and to critically examine if certain processes might have been wrongfully attributed. It also indicates that the interphase layer that forms between Li and “LiPON” is not as sometimes proposed a better conducting phase than the electrolyte itself but significantly worse. This might depend on the electrolyte composition though and the properties of the interphase might change if for example more nitrogen is present in the electrolyte and therefore more high conducting Li_3N is formed in the interphase. Variation of the electrolyte composition or properties was not in the scope of this thesis and is part of the work done by Matthias Geiß. In the future especially for very thin cells it might be necessary to consider the composition of the interphase first and the electrolyte properties second when designing the electrolyte.

11.4 Energies of activation for the various processes

11.4.1 Exclusion of additional temperature effects

After the processes were successfully identified the activation energy for the individual processes was measured to obtain further insight into the limitations of the individual transport and to judge the transport mechanism for some of the processes involved. In order to first determine that the activation energies measured are not connected to the method employed while measuring, some preliminary experiments had to be carried out. First any influence of the temperature on the measured cell (besides the Arrhenius behavior) had to be ruled out in the given temperature range. Possible side reactions include degradation of the electrolyte or the formed interphase films as well as possible annealing effects on the interfaces leading to a change in contact geometry. To rule out these effects the impedance of the cells was measured during the ascension of the temperature profile as well as during the following descension back to room temperature. The individual resistance values for each process (semicircle) was extracted from the fitting of the impedance data and converted to an Arrhenius plot to obtain the activation energies for the different processes. Fig. 29 depicts the described measurement for a typical Li/“LiPON”/LTO cell. The data points for the ascending and descending measurement are very close to each other for each individual cell process. The only data point of significant difference is at 30 °C for the thin film conduction (R_{Tf}). Since the difference is rather small and it is the only data point showing any remarkable difference this has been attributed to an outlier value in either the measurement itself or the fitting process of the impedance that lead to the resistance values obtained. Due to the complexity of the impedance data individual spectra can show slightly differing values depending on how the fitting algorithm approaches the data in the specific case. The influence of the outlier data point on the fitted activation energy is in any case quite minor and likely overshadowed by the statistical error obtained over multiple measurements.

The data confirms that no irreversible change occurs during the temperature treatment of the cell and that the holding steps during the temperature treatment are long enough to

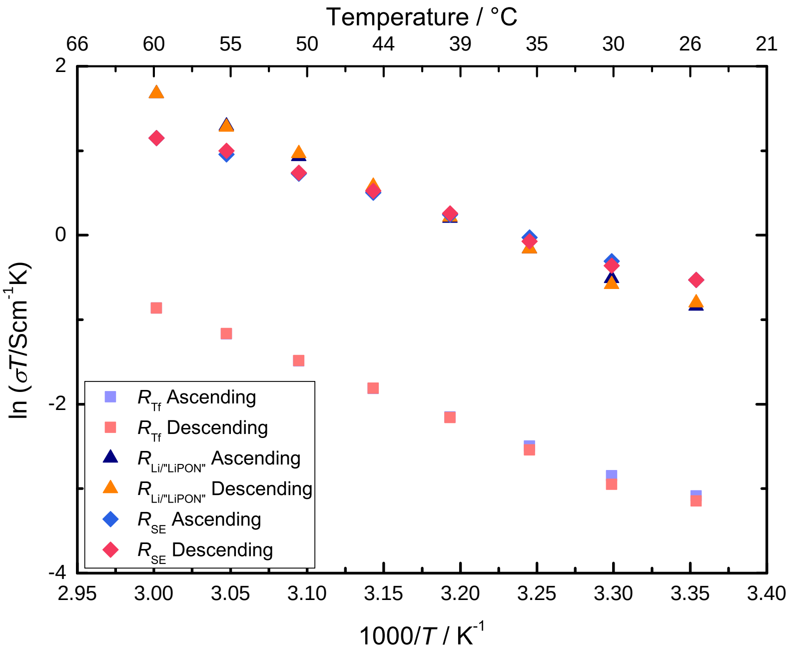

Figure 29: Arrhenius plot of the individual processes observed in the Li/“LiPON”/LTO cell for the ascending and descending part of the temperature profile. (Error bars derived from the fitting error of the impedance data have been omitted to reduce image clutter. Refer to fig. 32 for an example of the error magnitude)

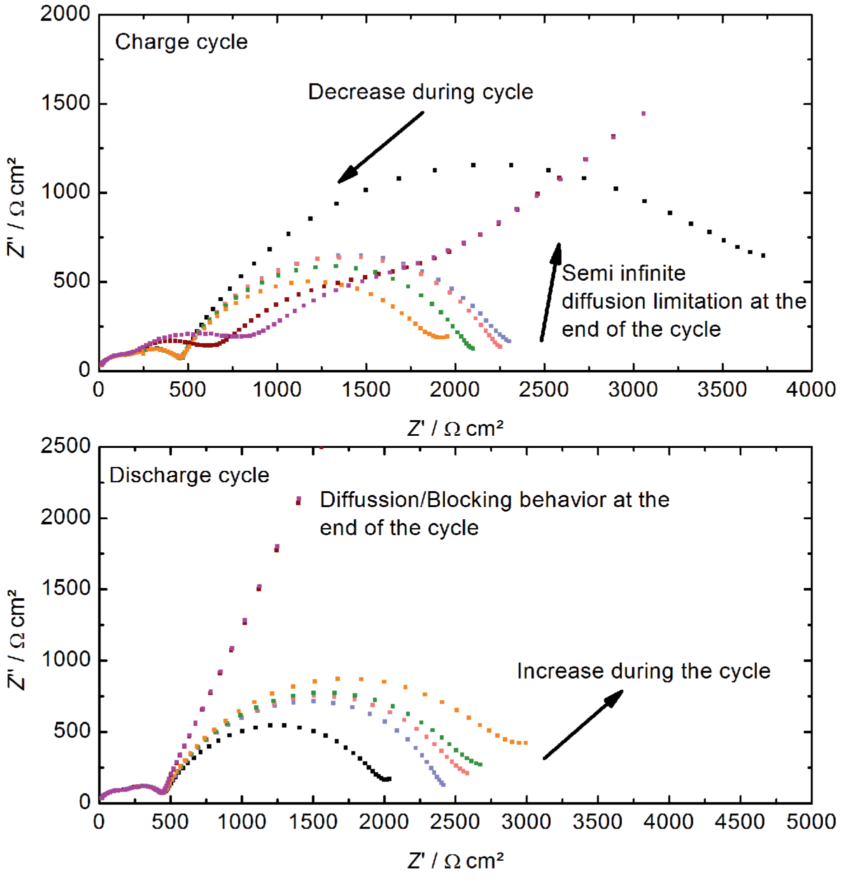

Figure 30: Nyquist plots of a Li/"LiPON/LTO cell during the charge and discharge cycle.

fully equilibrate the cell. The temperature range and processing is therefore suitable for the measurement of the system.

11.4.2 Achieving a fixed state of charge for the measurement

Since the impedance spectra of the cells are very dependent on the state of charge as shown previously the state of charge at which the activation energy is measured is important in order to draw conclusions about the cell behavior. Three main states are in theory interesting for the analysis, the fully charged, fully discharged, or any other defined equilibrium state in between with the 50% charged state being the most straightforward. The fully charged and discharged state are somewhat problematic because in the low frequency process the lithium conduction through the thin film transforms into a blocking/diffusion limited behavior near the end of the charge/discharge cycle. Fig. 30 depicts this behavior. While the cell can easily be modeled with a 3 process equivalent circuit during the majority of the cycle the behavior change at the respective cycle endpoints is too drastic for the model to still be applicable. The material at this point is nearly fully drained and the electrode behavior changes from lithium transport to a mix between lithium blocking and semi infinite diffusion behavior depending on charge or discharge cycle. The exact nature of the behavior is difficult to describe because the state of the cell at this point is not clearly defined. Regions of the completed phase transition probably coexist with small parts of the electrode that have not been active in the cell cycle and show some diffusion behavior while other parts are completely filled with or devoid of active lithium an therefore act blocking. The data can of course still be analyzed by fitting but by changing the corresponding equivalent element the values obtained are not comparable to data previously measured in the cycle both chemically and mathematically.

Also visible in the figure is the effect the high state of charge has on the medium frequency. With the behavior change in the low frequency region there is also a slight increase in resistance in the medium frequency region. This is a residual effect of the still not completely optimal charge transfer between the platinum film and the LTO electrode. While overall the charge transfer process was mostly eliminated by the use of platinum, for some individual samples at the very end of the charge cycle the process was still visible. This is attribute to the nearly complete phase transformation to the $Li_4Ti_5O_{12}$ high band gap material that seems to still cause problems under certain contact conditions. Why the process only appears for selected samples is still unclear and is probably related to minor changes in the forming contact due to slight variations in cell processing or deposition parameters. The increasing polarization of the interface due to the potential increase in this SOC region might also attribute to the higher resistance. This illustrates that the electronic contact of electrode materials is not necessarily negligible even if metal current collectors are applied. In the discharge cycle the process is not present even at the end of the cycle because the pure $Li_4Ti_5O_{12}$ is never fully formed at the interface as described earlier.

Another problem when trying to measure the system in a fully charged and discharged state is of a more fundamental nature since during the impedance measurement current flow is not limited. Due to the difference in charging and discharging material properties of this cell the net charge transport during the impedance measurement is not necessarily symmetrical. Due to the frequency range measured the time required for the impedance measurement was multiple minutes. Since the impedance response at the end states of charge and discharge is already very sensitive to the SOC it is possible that the changes in the SOC induced by the impedance measurement change the cell behavior.

Considering all these points measuring the cell impedance in the fully charged and discharge state is not feasible for the determination of the activation energies of the different cell processes (except for the conduction through the solid electrolyte for which the state of charge is irrelevant). The activation energies of the system therefore have to be determined

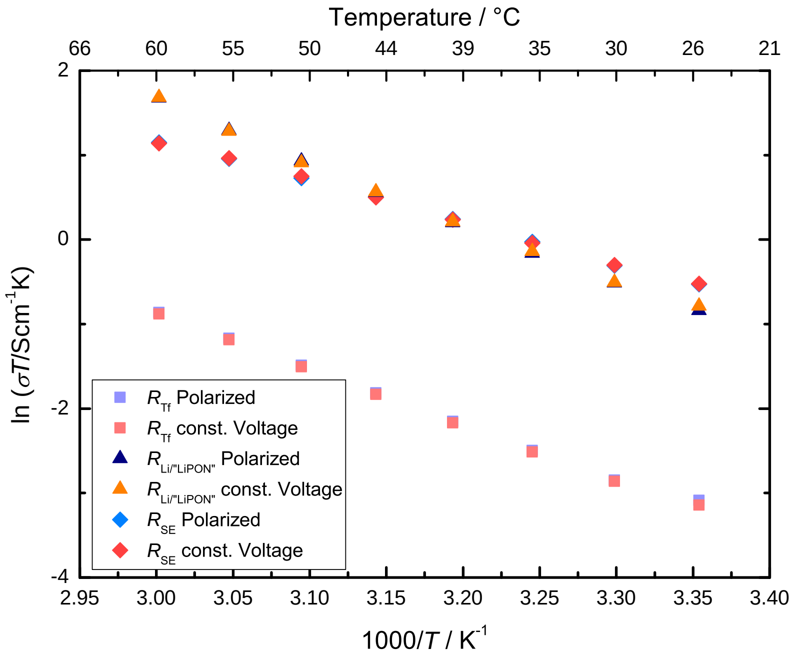

Figure 31: Comparison of activation energy measurements performed with different methods of cell equilibration. Polarized measurements describe an initial cell charge/discharge to the equilibrium potential while const. voltage describes the application of this potential as external voltage across the entire measurement.

at the equilibrium state near 1.55 V. To equilibrate the cell to this state two experimental setups are feasible, one involves the charging/discharging of the cell to 1.55 V and subsequent impedance measurement without controlling the cell potential which again allows for minor changes in the state of charge in between measurements. The second approach is the constant application of an external potential of 1.55 V during the whole measurement. A constant application of an external voltage might influence the phase relaxation behavior of the phase since the phase separation into the pure phases can be induced kinetically. To confirm if one of these methods has a detrimental or otherwise influencing effect on the impedance response both were measured and compared.

Fig. 31 depicts this comparison experiment. As is evident from the data the measured resistance values and therefore the properties of the Arrhenius plot do not change with the method of equilibration. This indicates that either no change in the state of charge occurs during the impedance measurement in equilibrium or that the change is minor and does not influence the resistance values fitted (the latter being more likely). Also the cell does not loose significant amounts of charge during the roughly 24 hours the impedance measurement and thermal treatment requires.

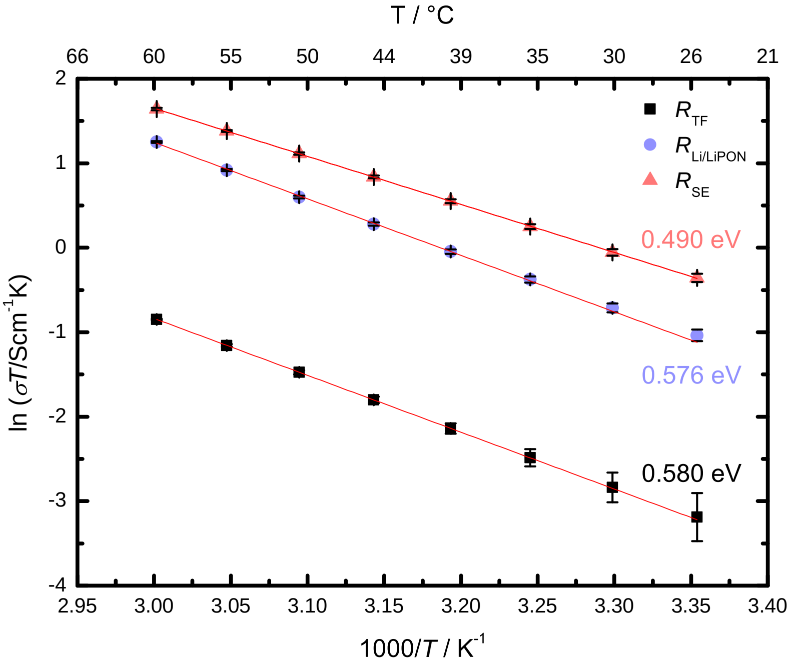

Figure 32: Arrhenius fit of the impedance data for a Li/“LiPON”/LTO cell.

11.4.3 Determination of activation energies

With the state and properties of the cells defined the activation energies can be measured and determined by fitting the data of the Arrhenius plot. Fig. 32 features another set of example data for the determination of the activation energies including the linear Arrhenius fit and the activation energies determined. The linear fit is in good agreement with the measured datapoints with the error for the activation energy derived from the fit being quite small. As is evident though the measured activation energy differs somewhat between this sample and the sample shown above for the preliminary measurements. This is especially evident when comparing the datapoints for the Li/“LiPON” charge transfer. The measurement of the activation energy was performed on two identical samples with 5 different measurements across these samples. Since the deviation of the activation energies in these measurements was larger than the error for the activation energy arising from the fit of the data it was decided to instead use the deviation from the mean value as the error for the activation energy.

Tab. 4 lists the activation energies obtained from the data as well as the derived mean value and the maximum deviation of the data from the mean values. As a general tendency the activation energy is highest for the Li/“LiPON” charge transfer, followed by the thin film conduction and lowest for the conduction through the solid electrolyte. The error obtained for the Li/“LiPON” interface is also the highest which has multiple reasons. The two features in the impedance spectrum corresponding to the electrolyte conduction and the Li/“LiPON” charge transfer are both “smaller” semicircles in the high frequency region while the thin film conduction is a “big” semicircle dominating the lower frequency region. Since both high frequency processes infringe on each other and are less dominant the fitting algorithm has a slightly higher variance for these processes leading to some inconsistency in the obtained resistance values. This alone does not explain the variation as the resistance corresponding to the Li/“LiPON” charge transfer would often visibly vary in between samples. Since the charge transfer process at this interface describes either the charge transfer from the formed degradation layer to the neighboring phases or the transport through this interphase (the two processes are indistinguishable in the impedance data) the composition of the interphase is important for the value of the obtained activation energy. The interphase is formed in an uncontrolled way after cell assembly and the specific composition and geometry might vary slightly from sample to sample. Furthermore, if the transport through the layer is involved it is not clear what the relevant transporting phase is.

The activation energy observed for this process is higher than expected for “LiPON” (ca. 0.47 eV[3,21,32,34,44,108], Li_3N (ca. 0.43 eV[116]) and Li_3P (ca. 0.18 eV[118]) but lower than expected for pure Li_2O (ca. 0.7 eV[119]). Aside from the mentioned degradation products multiple intermediary compounds can form depending on the mechanism of the decay. Some of these compounds like $LiPN_2$ (ca. 0.6 eV[120]) have transport activation energies closer to the observed value and might therefore be involved in the transport process. Arguing this purely based on the observed activation energies is not conclusive though and can only serve as an indication. Since activation energies of the different materials are often given in a quite large range when compared to the difference in value obtained in this thesis a more detailed analysis would be necessary to draw exact conclusions about the nature of the Li/“LiPON” charge transfer resistance. From the values obtained though it seems as if the transport across the interface is definitely hindered by the interface and the good conduction properties of Li_3N and Li_3P do not enhance the transfer across the interphase either because the transport is limited by lesser conducting parts of the interphase or because the process in question is just the phase transference and no extended transport phenomenon. The latter case might become problematic if nitridic or phosphidic phases are to be used as protection layers for Li metal anodes as proposed for example by Zhu *et al.*[121] because the interface phenomena could limit the performance of the final battery.

The activation energy for transport through the solid electrolyte shows less of a variation throughout the measurement and the resulting value is approx. 0.45 eV. This is in good agreement with values reported in the literature.[3,21,32,34,44,108] The activation energy is on the lower end of reported values and is most closely matched by values obtained

Table 4: Activation energies determined for the Li/“LiPON”/LTO system and the different processes observed.

Measurement	$E_{\mathrm{a,\ Tf}}/\mathrm{eV}$	$E_{\mathrm{a,\ Li/``LiPON''}}/\mathrm{eV}$	$E_{\mathrm{a,\ SE}}/\mathrm{eV}$
1	0.566	0.62	0.47
2	0.580	0.58	0.49
3	0.570	0.60	0.42
4	0.570	0.59	0.42
5	0.564	0.66	0.43
Mean value	0.570	0.61	0.45
Max. deviation	0.006	0.05	0.03

by Jacke *et al.*[108] for “LiPON” deposited at elevated temperatures of about 200 °C. Since in the sputter setup used in this thesis no additional cooling of the substrate was possible the temperature of the substrate would often rise to about 150 °C to 180 °C possibly explaining the reduced activation energies. The conductivity values determined for the solid electrolyte are also typical for the material as mentioned before. The determination of the needed resistance values is complicated by the overlapping of the process with the Li/“LiPON” charge transfer leading to a relatively high error value but the scattering range is less than for the Li/“LiPON” charge transfer since the electrolyte is expected to have more stable properties in between samples and measurements than the charge transfer due to a better defined deposition process. As mentioned during the discussion of the impedance profile of the cell the “LiPON” conduction can only be measured in “front” contact measurement setups without silicon being part of the conduction path.

Fig. 33 depicts the activation energy for the HF1 process that is obtained in the case of the earlier samples for which the battery cell was deposited directly on the silicon wafer and impedance measured through the wafer. As a comparison data of the pure silicon wafer is given when measured in an equivalent cell setup (i.e. geometry) contacted with the same stainless steel backplate and utilizing a gold contact on the other side instead of the battery stack. For the battery on silicon the activation energy is much smaller than expected for the “LiPON” solid electrolyte further confirming that the process observed is not the electrolyte conduction. The activation energy is relatively high under the assumption that the electronic conduction through the silicon wafer is the measured process. The silicon wafer in this case was a n-doped (phosphorus) sample with a specific resistance of 1 Ω cm - 20 Ω cm. The phosphorus energy level introduced by the doping in this case of wafer is typically only about 0.05 eV below the conduction band of silicon and fully thermally activated at the measured temperature range.[122] The measured activation energy therefore cannot describe the band gap activation energy inside the doped semiconductor (ionization energy of dopand levels).

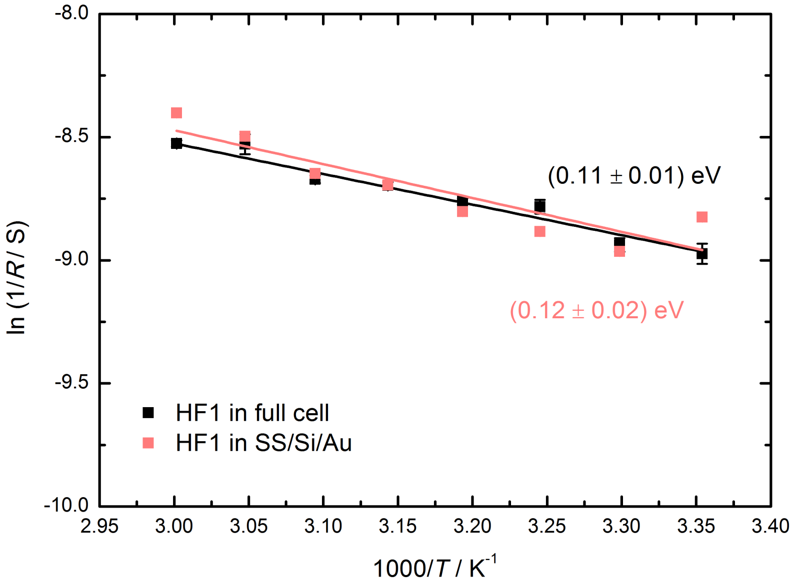

Figure 33: Comparison of activation energies obtained for the HF1 process in a full battery cell on a silicon substrate and of the silicon substrate measured between stainless steel (SS) and gold in an equivalent system setup.

The measurement of the isolated silicon wafer features nearly identical activation energy and resistive behavior confirming that the activation energy is related to the transport in the silicon wafer. Multiple explanations are possible for the higher activation energy observed. Depending on the temperature range the conductivity (and therefore resistance measured and activation energy derived) of the silicon is influenced by other factors like impurity scattering (typically below 200 K [122–124]) and the activation of the dopand levels themselves which can lead to an increase in conductivity with the temperature. On the other hand at elevated temperatures the semiconductor changes to intrinsic conduction behavior (1.1 eV activation due to the band gap) but again for silicon this is mostly expected above 500 K.[122–124] The change is gradual so some influence of the intrinsic conduction might influence the measured activation energy even at 360 K considering the comparatively low extrinsic carrier concentration. For the higher doped silicon variant with 0.006 Ω cm (arsenic) the activation energy measured was indeed very low with values ranging in the order of 80 meV but since the temperature range for the measurement was quite small such low activation energies are difficult to determine via the Arrhenius plot and the measurement therefore is not shown. This is consistent with the previous assumption since an elevated extrinsic conductivity would shift the dominance of intrinsic conduction towards higher temperatures outside of the measured range.

A second point that cannot be ignored is the influence of the stainless steel contact on the measurement. While the gold contact was described earlier the steel contact that is present in both pure silicon and battery measurement was not defined. It may be hidden underneath the gold contact signal but might as well influence the region of the impedance spectrum where the silicon conduction is measured. In this case an apparent activation energy would be measured that consists of the nearly stable resistance of the silicon wafer (in the given temperature range) and the changing resistance of the contact leading to an activation energy somewhere in between that is not defined since the processes are not separated. In contrast to the gold/silicon contact signal the HF1 process is only slightly dependent on applied potential as seen in fig. 21 indicating that a possible contact contribution from the steel contact would be rather small. For the gold contact no activation energy for comparison could be determined in the given temperature range since the data did not follow typical Arrhenius behavior i.e. the resulting line plot would be constant or slightly negative probably caused by statistical variation of resistance measured in the impedance data. Nevertheless the behavior of the HF1 process is identical when measuring pure silicon and the battery cell on a silicon substrate.

The activation energy measured for the conduction through the LTO thin film was very reproducible and only showed slight deviations in between measurements and samples. One reason for this is that the semicircle corresponding to the thin film conduction is quite “big” and dominates the impedance spectrum in the lower frequency range. The impedance fit for the process is therefore more accurate since the influence of the other processes on the obtained resistance values is relatively small. Another reason might be that the activation energy is less dependent on the small differences in material properties between measurements and samples because the solid solution exists within a wide window of compositions and exhibits the same activation energy within that composition range. Reported activation energies for the pure spinel $\mathrm{Li_4Ti_5O_{12}}$ and rock salt $\mathrm{Li_7Ti_5O_{12}}$ phase vary in a very broad range in the literature. For the spinel phase values between 0.3 eV to 0.7 eV are reported while the rock salt phase typically exhibits somewhat lower activation energies between 0.2 eV to 0.5 eV.[14,125–128] Both Ziebarth *et al.*[128] as well as Wagemaker *et al.*[13,14] have discussed the transport mechanism for the pure phases as well as for the forming solid solution at room temperature. The activation energy here depends on the lithium ion path through the material that is crystallographically different for both materials. As mentioned in section 6 for the stoichiometric spinel phase lithium is positioned in the $8a$ tetrahedral positions while the $16c$ octahedral positions remain empty. The transport path consists mainly of a hopping mechanism between the empty $16c$ sublattice and the occupied $8a$ sublattice. For the stoichiometric rock salt phase the situation is reversed and the $16c$ positions are occupied while the $8a$ positions remain empty. The energy of the $8a$ and 16 c positions therefore is not identical in both systems and the energy of activation for the transport is different. Chen *et al.*[129] note though that the $48f$ positions are also partly involved in the transport path.

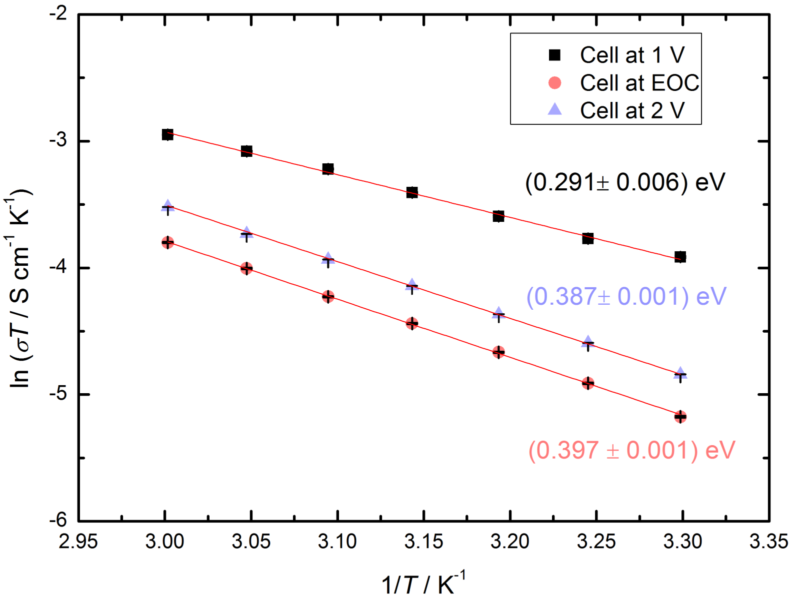

Figure 34: Activation energies of the lithium ion conduction in the thin film at different cell states. The cell was cycled close to the given potential and the potential was then applied during the measurement.

In the solid solution both sublattices are partially occupied and the energies of the individual positions in the conduction path is somewhere in between the values of the pure phases. In the case of two phases coexisting within the material layer the change of activation energy is expected to be linear as also argued by Ziebarth *et al.* due to the activation energy measured being the apparent activation energy of the combined composite. In most experiments though the activation energy drops rather sharply as soon as lithium is inserted into the spinel. Ziebarth *et al.* argued that therefore additional diffusion processes for example along grain boundaries might be involved. But their work modeled the pure spinel and rock salt phases and the conduction paths within, the formation of a solid solution phase was not directly considered.

Fig. 34 depicts the activation energies measured for a thin film cell (Li/“LiPON”/LTO(180 nm)/Si in this case) at different stages of charge. It was already described previously how measuring the impedance in the fully charged and discharged state is difficult and not necessarily comparable to the equivalent circuit during the remaining charge states, yet it was still attempted to compare states of higher lithium content with states of low lithium content. The figure depicts the activation energy that was determined after the cell was charged or discharged close to the endpoints of the cycle (about 90 % SOC and 10 % SOC) and afterward the cut off potentials were applied during the impedance measurement to achieve a comparable polarization environment to the fully cycled state. Note here that because of these reasons the states of the battery measured in this setup are not equilibrium states.

The activation energy determined for the near fully charged state (close to 2 V) and the intermediate state (close to EOC) are nearly identical and both are higher than the activation energy measured near the fully discharged state (close to 1 V). This is consistent with the discharged rock salt phase having a lower activation energy for transport, but the decrease is as mentioned above not linear. The difference of state of charge between 2 V and EOC is about the same as the difference between EOC and 1 V. This is consistent with the observed sharp drop in activation energy described above (activation energy expected from pure LTO is higher than what is measured here even in the “charged” state). In the equilibrium measurements depicted in tab. 4 the activation energy is typically higher even though the state of charge is expected to be similar to the EOC measurement depicted in fig. 34. The difference can possibly be explained by the different phase state of the battery during kinetic conditions and equilibrium conditions (solid solution vs. two phase separation) but it is also possible that the lower thin film thickness used in these measurements (to decrease cycle time) has unexpected effects on the activation energy measurement. The latter might be the case if, as suggested by Ziebarth *et al.*, grain boundary conduction has a significant role in the measurement. The activation energy of the solid solution or phase composite is therefore possibly masked for thinner films while for thicker films the same measurement cannot be carried out because the film displays the same activation energy across a large window of SOC and the activation energy does not change near the end states of the respective cycle before it becomes masked by the blocking and diffusion phenomena mentioned before. Apparently this is caused by different levels of film utilization and relative phase transition in thicker films. So in both cases during the majority of the battery cycle the activation energy appears constant but it is unclear how the ratio between bulk conduction and grain boundary conduction is because the processes are not separated in the impedance data.

Since the activation energy for grain boundary conduction is not expected to change with film thickness an increase of activation energy for the thicker film indicates that the energy measured is not just the grain boundary conduction but at least partially involves the bulk activation energy. The difference in activation energy for the different film thickness is therefore more likely to be attributed to the difference in phase state and, considering it does not change during most of the battery cycle, that the phase state is stable across most of the cycle. So even though the grain boundary conduction likely influences the measured activation energies it is not solely responsible for the drop and subsequent stability of the activation energy upon lithium insertion.

Since the cell is allowed to relax into an equilibrium state in the activation energies depicted in tab. 4 the values probably represent the formed solid solution. The values obtained are above the typical range reported for the rock salt phase (0.2 eV to 0.5 eV as opposed to 0.57 eV measured here). If an error due to the influence of the grain boundary is assumed the real activation energy is expected to be slightly higher because the grain boundary activation energy is expected to be lower (apparent activation energy is reduced in the case of grain boundary conduction). This in turn indicates that the conduction path in the solid solution might be more comparable to the path in the spinel phase than to the path in the rock salt phase. These results are of course only superficial observations indicating a possible similarity in transport mechanism without concrete modeling of the transport paths in compositions with different lithium content. The data though is in agreement with the work done by Wagemaker *et al.*, Wilkening et al, and Ziebarth *et al.* for the macroscopic bulk material. It confirms that inherent material properties of the LTO material have strong implications for the behavior of the impedance spectrum for the thin film batteries because large parts of the frequency range are governed by the electrode properties. The application of a solid solution phase change model is necessary to understand the impedance response. This is true even under kinetic conditions while for bulk cells in liquid electrolytes a core shell model of phase separation that is kinetically induced is sufficient to describe the measured data.

11.5 The LTO/“LiPON” charge transfer resistance

As described earlier for many all-solid-state systems and batteries in general the cathode/electrolyte charge transfer resistance is a major component controlling the kinetic and resistive behavior of the battery cell, yet no such process has been found in this system and all visible processes in the impedance data can be attributed to other processes during cycling. Early reports by Iriyama *et al.*[21] already suggested that the LTO/“LiPON” interface charge transfer is not a major contributor but the authors also did not directly measure the charge transfer impedance during cycling and instead deducted the result from the satisfactory cycling behavior. But can the process be analyzed by impedance spectroscopy if sufficient experimental conditions are met? Due to the earlier results indicating the strong dominance of the LTO thin film conduction in the low frequency region very thin LTO films are required for the analysis of the charge transfer resistance.

Fig. 35 depicts the Nyquist plot of the impedance measured for a thin film cell with a LTO film thickness of approx. 90 nm. The spectra consist of two semicircles in the high frequency region attributed to the electrolyte and the Li/“LiPON” charge transfer identical to previously shown data. The semicircle for the ionic transport in the LTO film though is significantly reduced when compared to for example fig. 30 and decreases further during the charge cycle. Additionally, for the intermediate potentials in the low frequency

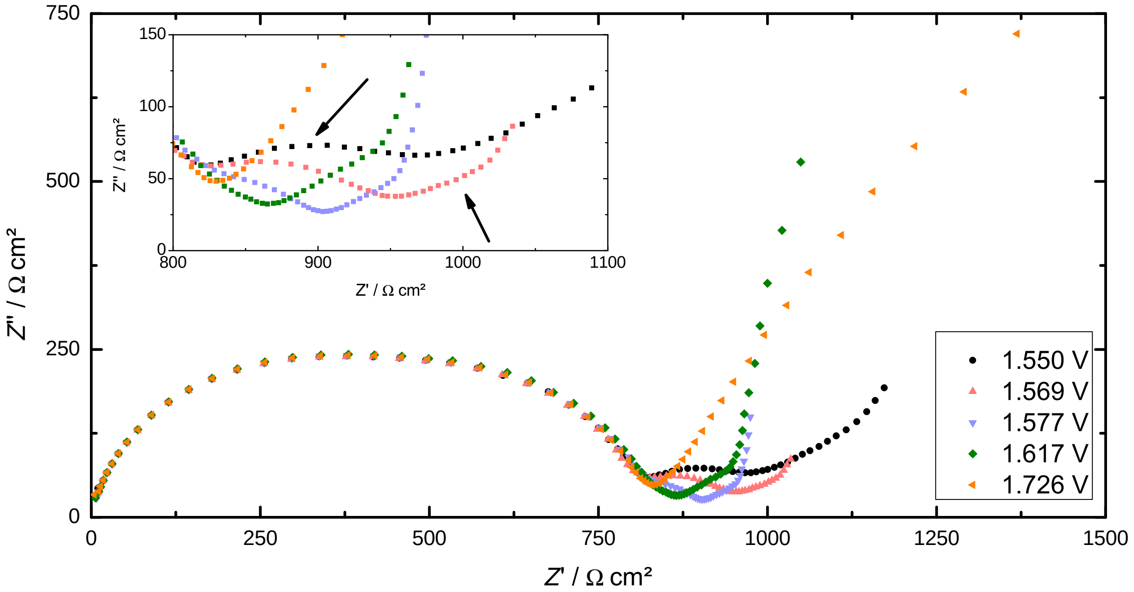

Figure 35: Nyquist plot of a LTO cell with a LTO film thickness of approx. 90 nm during various stages of the charge cycle indicated by the cell potential. The resistance of the thin film for this sample reaches small enough values for an additional process to be visible between 900 Ω/cm^2 and 1000 Ω/cm^2 on the real axis. The arrows indicate the direction of spectra evolution during the cycle.

region another process appears once the thin film conduction is sufficiently reduced in size. The process is magnified in the inset graph and can only briefly be determined at intermediate cell potentials of about 1.569 V to 1.617 V that represent a region of SOC of about 65 % to 90 %. Before this point the process is still dominated by the ionic conduction of the thin film and towards higher states of charge the low frequency behavior switches to a diffusion limited/blocking type behavior. It might be argued that the resistance of the charge transfer increases towards 100 % SOC and that the low frequency region at this point is dominated by the greatly increased transfer resistance which causes the change in spectrum shape. This distinction is somewhat semantic though because naturally blocking electrode behavior and greatly increased charge transfer resistance are two equivalent ways to describe the same phenomenon: the electrode can no longer extract/insert lithium. Measuring the charge transfer resistance is therefore only possible in a small potential (or SOC) window near the end of the charge cycle. Monitoring possible changes in the charge transfer process is not possible due to this small measurement range.

When trying to reduce the thickness of the thin film even further to increase the impact of the charge transfer process another problem starts to appear. PLD films deposited with a film thickness lower than approx. 90 nm to 100 nm were problematic due to the formation of droplets during the deposition process. These droplets exist for all films but once the film thickness was decreased below the just mentioned value in the impact zone around those droplets the film was often disrupted and no longer fully covering the

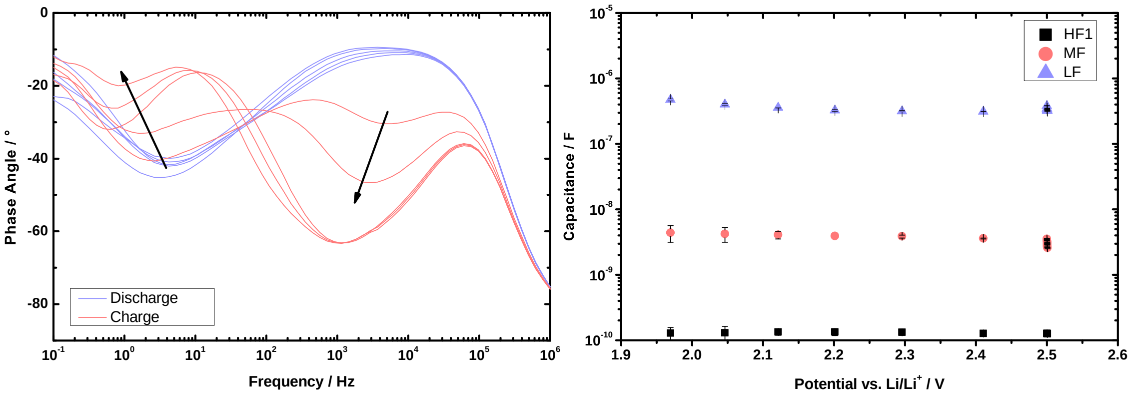

Figure 36: Phase angle plot and charge capacitance for a LTO dip coating film on a silicon substrate approx. 50 nm thick.(Note that the charging voltage for the cell is increased due to high internal cell resistances)

substrate. This was the case even for smaller droplets which lead to a very non uniform covering of the substrate for these films. To produce very thin films LTO was deposited through dip coating with film thicknesses of about 50 nm to 80 nm on pure silicon and Ti/Pt covered silicon but the films had adhesion problems on the Pt layer so that only films on pure silicon could be utilized for cell testing. Fig. 36 depicts the phase angle of the system during charge and discharge as well as the capacitance extracted for these processes versus the cell potential. Because the thin film is deposited directly on silicon in the medium frequency range the electronic charge transfer resistance between LTO and silicon appears again but the resistance of that process is vastly increased for this film. It is also evident that during the charge cycle the resistance increases further (indicated by the arrow) while in the discharge cycle the resistance is mostly negligible. This has already been identified to be an effect of the electronic properties of the two LTO phases and fits previously observed behavior.

The value of this resistance on the other hand is much larger than for similar cells with thicker LTO films. While it is not readily apparent why the charge transfer resistance is dependent on the film thickness it might be because of the size of the forming space charge layer. It is not exactly known how far the space charge layer extends into the LTO and silicon phase respectively but due to the low charge carrier density especially in the charged LTO phase it can be expected to be more than a few nanometers. The film geometry though is limited at 50 nm and this might lead to the space charge layer extending throughout the whole thin film and possibly interfering with the space charge/interface effects on the electrolyte side of the thin film. It could also be an effect of the dip coating preparation but for thicker dip coating films comparable behavior to the PLD films was observed (aside from some adhesion problems for multilayer dip coating films).

The process in the low frequency range in this sample is slightly ambiguous. Typically for thicker films this process would represent the conduction through the LTO film but as shown in fig. 35 for films this thin the conduction resistance is expected to be negligible. The size of the process also does not change as would be expected due to material properties for the ion conduction process but instead stays mostly the same during the discharge cycle and shows an uncharacteristic shift towards lower frequencies in the charge cycle. Comparing the capacitance values for this process as can also be seen in fig. 36 (LF) the capacitance is relatively high but not as high as previously seen for the lithium ion conduction in the thin film (compare fig. 26) despite the capacitance being expected to further increase for thinner films due to the geometrical effect. These factors indicate that the process in this case is not the ion conduction but in fact the charge transfer resistance between LTO and “LiPON” that is also expected in this frequency range. In this case though the large value of the resistance is questionable since the process was previously shown to be almost negligible when compared to the other processes. Again this might be explained with the overlap of both substrate side and electrolyte side space charge layer increasing the resistance of both charge transfer processes vastly. The lowered capacitance of the process is due to the partial involvement of the “LiPON” phase in the charge transfer resistance. Despite the lowered geometrical distance for the capacitive process the “LiPON” phase is expected to have a lower permittivity compared to the LTO phase and therefore the mean permittivity of the interface is lower leading to lower capacitance values than for the pure LTO.

During the discharge the electronic charge transfer process disappears, as described earlier, but the LTO/“LiPON” charge transfer retains its high resistance value. This high resistance can be caused by the space charge layer stretching across the whole thin film at all states of charge for this thin film. In that case the resistance is increased due to the geometric limitations for the layer and the charge transfer resistance is additionally influenced by the electronic charge transfer once that process becomes significant. Another possibility is that for the dip coating film the charge transfer resistances is just higher in general when compared to other films. For thicker samples deposited through dip coating the ionic conduction once again was dominant in the low frequency region so that no particular differences for the LTO/“LiPON” charge transfer were observed indicating that the high resistance is probably related to the extended region of the space charge layer and not inherent properties of the dip coating films.

Currently most of the work regarding space charge layers in solid state batteries is concerned with space charges forming in the solid electrolyte so not much data on the electrode materials exist because the electrode in practical application is expected to be a) modified to facilitate ionic and electronic transport (i.e. conducting agents) and b) not necessarily deposited as thin as possible because the layer capacity is important for the final cell. These results still have implications for the system because the space charge layer in the solid electrolyte is expected to be comparable to the layer inside the electrode but the electrolyte in the final cell is expected to be as thin as possible. For very thin layers the overlap of cathodic and anodic space charge layer might significantly increase the overall cell resistance limiting the electrolyte film thickness not just by preparative conditions but also intrinsically. The opposite effect is also possible in case both space charge layers overlap in a beneficial way. For the electrolyte the situation is somewhat different of course because both space charge layers or interface regions are comprised of a increase or decrease of mobile lithium concentration while in the electrode one side is dominated by electronic and one by ionic effects which might lead to different behavior.

As far as the LTO/“LiPON” charge transfer is concerned it is negligible under typical battery conditions and is barely measurable. It does become relevant for very thin films but is then seemingly amplified by the geometric conditions of the film and because of this influence not necessarily comparable to its properties in a “normal” cell environment.

12 LNMO preparation and characterization

12.1 The temperature stability of LNMO under PLD process conditions

For the deposition of LNMO initially deposition parameters following the work of Mareike Falk[50] were used but it was quickly realized that those parameters seemed only applicable for very thin LNMO layers in a specific setup since none of the produced films seemed to be electrochemically active. The XRD and Raman characterization of these films proved to be difficult because signal intensity was typically very weak and the data therefore not suited for characterization. It was assumed that the elevated deposition temperature that was used in the work of Mareike Falk to achieve smooth films for SIMS analysis was too high for films thicker than 50 nm and caused a degradation of the material. It is known that the material can develop a rock salt impurity phase together with the formation of the disordered spinel phase at elevated temperatures. This is generally described to be happening around 700 °C (although the exact temperature is somewhat debatable). This can be somewhat confusing because synthesis conditions for the material in the literature are often above 700 °C for the bulk material too. In that case the material is expected to equillibrate into the ordered phase again if cooled slowly or the disordered phase is desired since it mostly shows higher capacity and better electrochemical performance in liquid systems.[82,130,131] Synthesis conditions for the bulk material are often under air but the deposition in the PLD process necessarily has to be performed under partial vacuum even though oxygen is used as the background gas this might cause loss of oxygen in the material and enhance the formation of the non stoichiometric disordered phase and the formation of the impurity phases.

In order to determine the temperature stability window for the material used in this thesis temperature dependent *in situ* XRD measurements under vacuum conditions were performed. Due to technical limitations of the setup the vacuum achieved in the XRD chamber was only delivered by a membrane pump and no additional oxygen was introduced to replicate the exact PLD processing conditions. The partial vacuum delivered by the pump in the order of 100 Pa to 10 Pa is somewhat comparable to the deposition parameters. Fig. 37 depicts this temperature dependent measurement for the LNMO powder utilized to form the PLD targets. As can bee seen in the data to the left the degradation of the material starts somewhere in between 600 °C and 700 °C and in the more detailed data to the right the degradation temperature can further be narrowed down to about 650 °C. The initial XRD pattern measured at 50 °C is also given as a comparison in both data sets. Because the reflex positions in the patterns shift at elevated temperatures in the detail plot the forming degradation phase reflexes are marked with an asterisk. At higher temperatures above 700 °C the three reflexes marked are growing further in intensity while

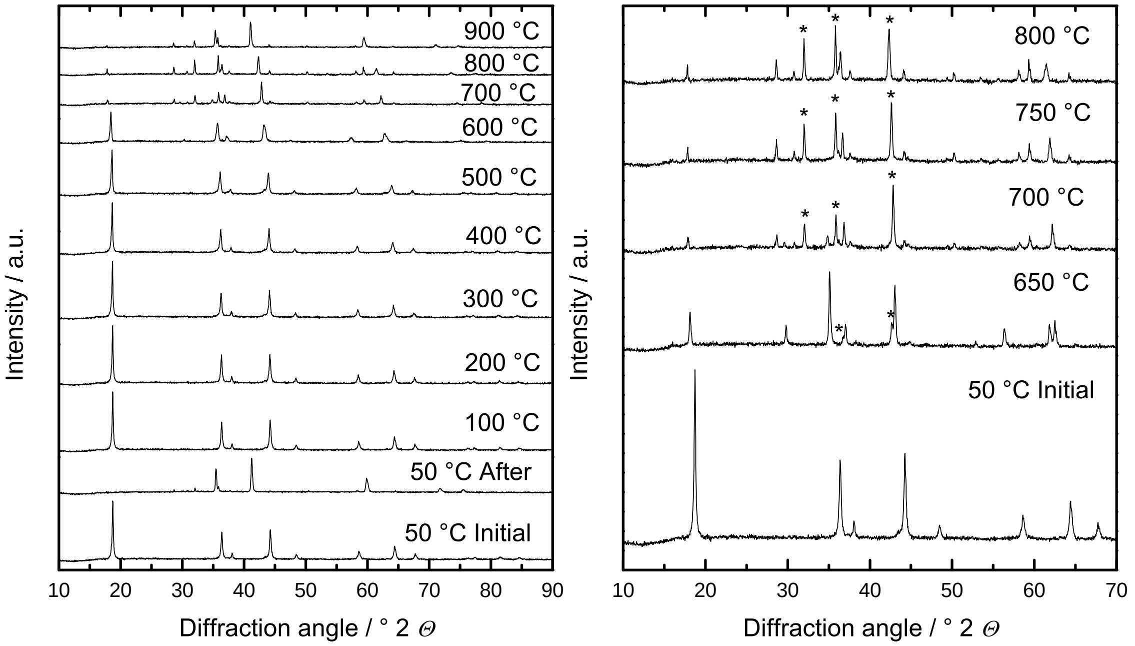

Figure 37: Temperature dependent in-situ measurement of the LNMO powder utilized to form the PLD target. The measurement was performed at 100 Pa to 10 Pa partial vacuum. A degradation of the material is clearly visible above 600 °C and a finer temperature resolution is given for that temperature range. The formation of the forming degradation phase is marked with asterisks.

all other reflexes lose intensity and start to fade. After the sample was cooled down back to 50 °C the XRD pattern is completely changed to feature only three major reflexes (not identical to those measured at elevated temperatures). Because of the reflex shift in the pattern at higher temperatures the multitude of different reflexes appearing in the pattern and the general intensity loss of the data it is difficult to determine which phases exist at these temperatures. At around 650 °C where the pattern is still quite similar to the initial pattern the beginning formation of the reflexes around 30 ° and 44 ° (marked with an asterisk) can be interpreted as the formation of the expected rock salt impurity phase that is typical for the transformation into the disordered spinel phase. It can also be seen that this phase disappears after the subsequent heating and cooling since the reflex positions in the sample after cooling down are not comparable to the positions of the impurity phase.

For the cooled sample fig. 38 offers a comparison to the initial sample and a possible explanation of the degradation occurring after 700 °C. The pattern of the LNMO spinel is given as a reference and the initial sample matches the expected pattern. After temperature treatment the new found pattern can be attributed to a nominal $Mn_{0.75}Ni_{0.25}O$ phase. Note that the pattern does not match up exactly which is probably because the phase does not exist in that exact stoichiometry but is in fact a mixture of MnO and NiO which have very similiar diffraction patterns. The degradation therefore indicates that lithium loss occurs at higher temperatures and possibly the formation of lithium oxide.

While some of the smaller reflexes can possibly be attributed to Li_2O and the phase also has some overlap with the three dominant reflexes shown in the figure, no clear indication for Li_2O can be found in the XRD data. It is likely that the lithium oxide is lost at 900 °C and vacuum conditions in the chamber. The degradation can therefore be described as:

$$2\,\mathrm{LiMn_{1.5}Ni_{0.5}O_4} \xrightarrow[\text{- 1/2 } \mathrm{O_2}]{} \mathrm{Li_2O} + 2\,\mathrm{Mn_{1.5}Ni_{0.5}O_3} \xrightarrow[\text{- } \mathrm{O_2}]{} \mathrm{Li_2O} + 4\,\mathrm{Mn_{0.75}Ni_{0.25}O} \tag{4}$$

With the oxygen loss in the last step likely occurring because of the reducing conditions due to the partial vacuum. The intermediary product is a Mn_2O_3 derivate and again the expected pattern for Mn_2O_3 can possibly be found in the smaller reflexes and overlapping with the big reflexes of the sample after treatment. Due to the low intensity this is not conclusive indicating that only small amounts of the Mn_2O_3 derivative remain in the sample and the rest is further reduced to the MnO and NiO phases.

Considering the degradation above 650 °C under these conditions a deposition at or above

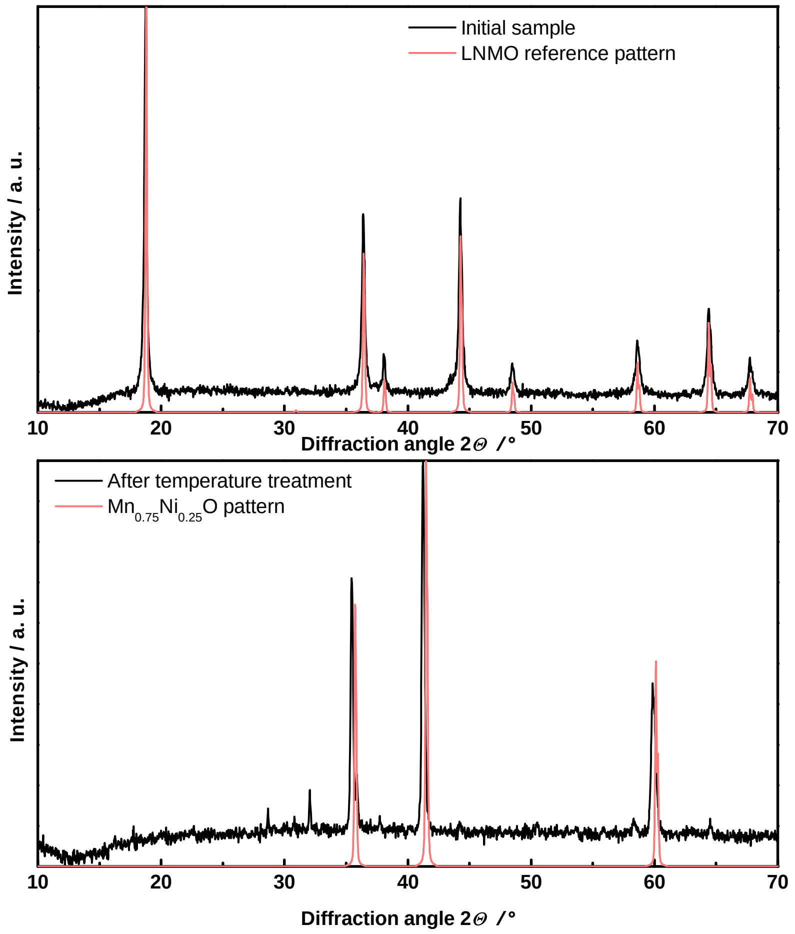

Figure 38: LNMO powder sample before and after heat treatment at 900 °C in the XRD chamber. Reference patterns for spinel LNMO and a possible degradation phase are also given.

these temperatures is not likely to produce the desired spinel LNMO phase. The characterization of the PLD thin films samples is especially challenging because the thin films are rarely polycrystaline and are instead deposited with a preferential orientation. This causes problems in the XRD analysis because often very few reflexes are observed that can be attribute to multiple different phases because the different manganese and nickel oxides tend to have very similar patterns if the reflex count is reduced that much. This is why this initial screening was carried out with a powder sample.

12.2 The choice of substrate for LNMO deposition

As with LTO before, the initial deposition of LNMO was carried out on silicon substrates due to prior experience with the material, its smooth surface and its conductivity allowing it to serve as an electronic contact material. Additionally platinum coated YSZ (as used by Mareike Falk) and platinum coated sapphire were used as deposition substrates. Fig. 39 depicts XRD data of several thin films deposited on silicon (100) substrates at different deposition temperatures. As with the powder sample the degradation of the material at temperatures above 700 °C is visible but more difficult to characterize for the thin films because of the lower overall intensity and the larger by comparison background of the data. At 650 °C the XRD pattern is in good agreement with the reference pattern given with most of the smaller, sharper reflexes (56° and 33° especially) being explained by residual reflexes of the silicon substrate. Especially the LNMO (111) reflex at approx. 18° is visible most clearly at this deposition temperature. Below 650 °C the (004) reflex of the LNMO phase at approx. 44° is highly increased in intensity indicating a (004) preferential orientation of the thin film but other reflexes like the (111) (18°) and (113) (36°) are still visible. Decreasing the deposition temperature further only causes a decrease in overall intensity of all reflexes (leading to vanishing of the (111) reflex) and broadening of the reflexes. This is possibly due to the decreased crystallinity of the films due to the low temperature.

The reflex position of the (004) reflex shifts from 43.46° at 350 °C to 43.71°, 43.76° and 43.57° at 450 °C, 550 °C and 650 °C respectively compared to the expected value of the reference pattern at 43.71°. This can indicate a shrinking of the lattice spacing in c direction with increasing temperatures possibly due to increased strain at lower temperatures since the d-spacing is closest to the expected value at 450 °C and 550 °C. It is also possible that the shift occurs due to the formation of different manganese or nickel oxide phases that share a similar reflex to the observed one. Considering the preferential (004) orientation of the material is not observed on other substrate materials the behavior indicates an influence of the silicon (100) substrate on the growth direction of the LNMO phase at lower temperatures. Above 550 °C the material growth direction changes to (111) which is accompanied with an increase of the *d*-spacing value for the (004) reflex i.e. the reflex position moves away from the expected ideal value. This can indicate that the strain in the material increases again for higher temperatures because of the orientation change of the thin film that seems to be incompatible with the substrate but is still preferred by the material. Above this temperature the material degradation starts and the crystallinity of the remaining material is reduced. Fig. 40 shows that the orientation of the thin film is different on Pt coated YSZ (111) substrates. Given are the raw XRD patterns for the LNMO thin film and the YSZ/Pt substrate. As is evident the substrate itself has a multitude of reflexes that makes it difficult to evaluate the LNMO thin film. For this reason a calculated line profile for the measurement is given featuring just the LNMO reflexes

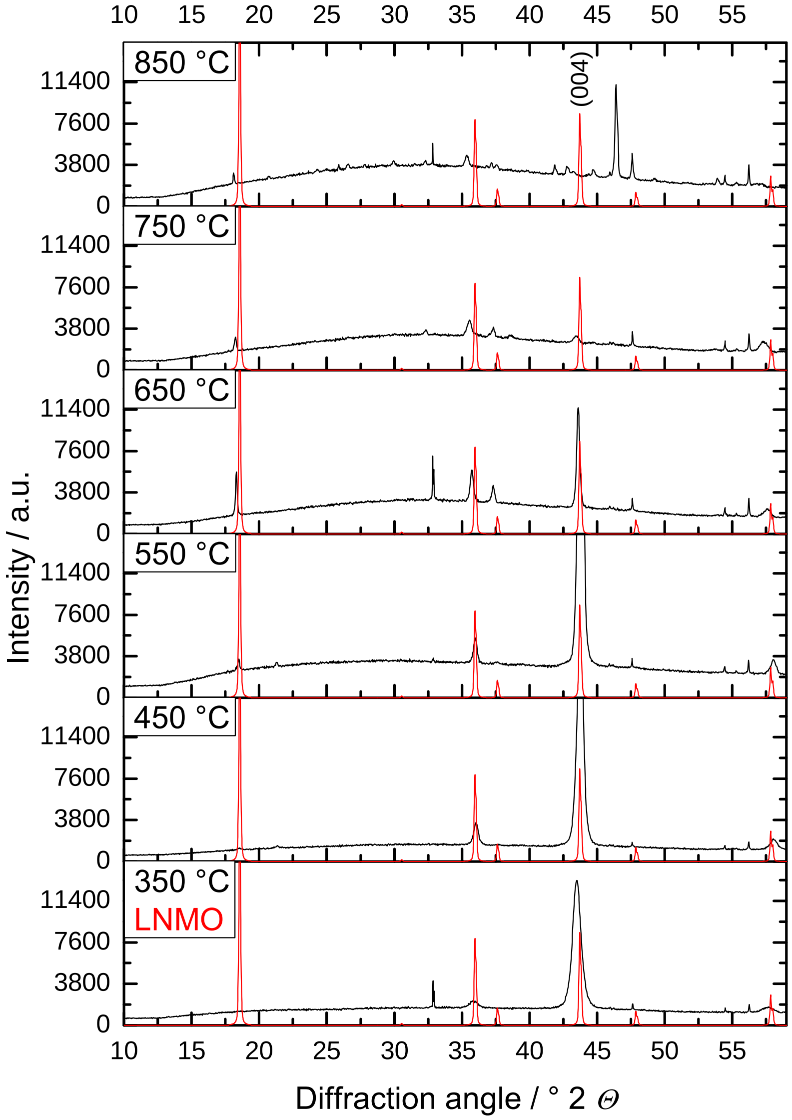

Figure 39: XRD patterns of LNMO thin films (ca. 500 nm) deposited on silicon substrates (100) at different temperatures.

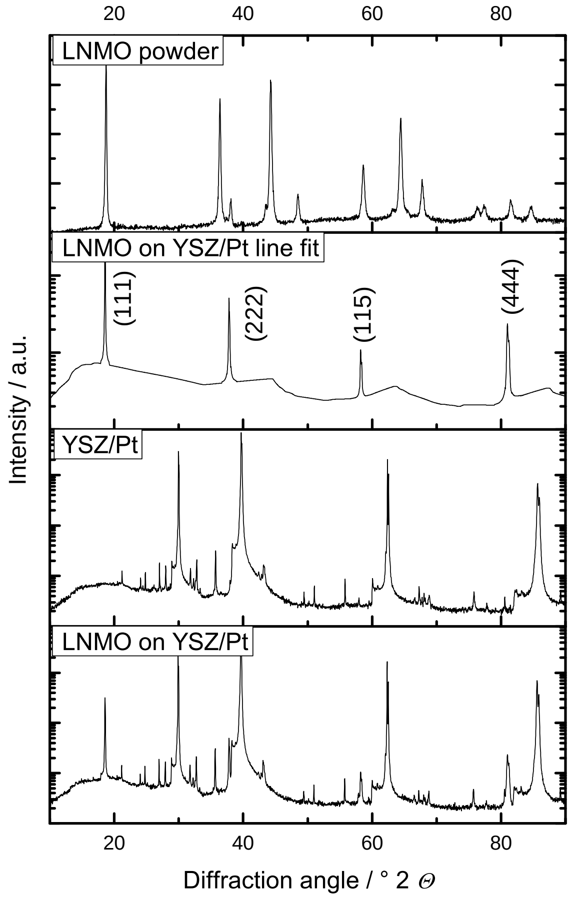

Figure 40: XRD patterns of LNMO thin films (ca. 500 nm) deposited on Pt coated YSZ (111) substrates at 550 °C. Additionally a pattern of just the substrate is given and a resulting line fit featuring just the LNMO reflexes.

visible in the pattern to show the effect more easily.

To determine this profile the substrate and thin film measurements were overlayed (both were measured with identical parameters) and the differences between the two were noted. This resulted in the position of the four reflexes visible in the reduced pattern. Following that a simple line profile fit was performed allowing only the four reflexes determined to be fitted which resulted in the shown pattern. Note here that this profile is only for visual clarity and does not represent a full representation of the thin film pattern. Other possible reflexes of the thin film can be present in the raw measurement but due to them being masked by the high intensity substrate reflexes they might not be visible and therefore do not appear in the line fit at all. The four reflexes determined through this method are the (111), (222), (115) and (444) reflex indicating a strong (111) preferential orientation of the LNMO thin film. The (113) reflex at 35.9° as well as the (004) reflex at 43.7° that still appears for the thin film on silicon substrates at higher temperatures are not visible here. Those reflexes also coincide with relatively strong reflexes of the substrate and might be

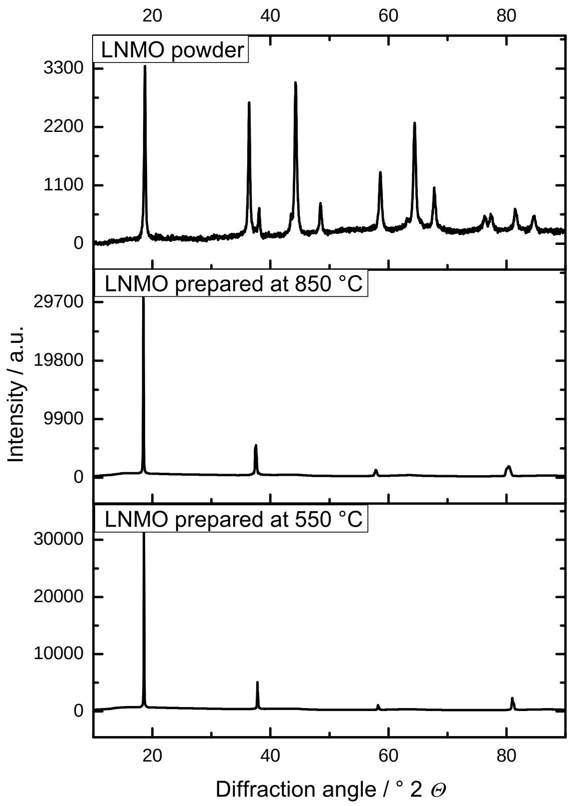

Figure 41: Comparison between two samples of LNMO on Pt coated YSZ substrates prepared at 550 °C and 850 °C. (reduced pattern via line profile fit as described in the text earlier)

masked. Nevertheless the reflexes of the (111) direction are much more clearly visible and of higher intensity than for the comparable thin film on the silicon substrate indicating that the substrate has a influence on the growth direction even though the thin films are relatively thick at about 700 nm. The (111) direction seems to be somewhat preferred by the material since it is formed against the substrate induced growth direction on silicon at higher temperatures and the samples on YSZ/Pt show overall higher relative reflex intensities indicating better crystallinity. This is comparable to the effects observed for LTO which showed preferential (111) growth on all substrates. The same orientation effect as describe for Pt coated YSZ can also be observed on Pt coated sapphire but on these substrates the film adhesion after “LiPON” deposition was very bad. Because almost none of the samples deposited on sapphire substrates produced working cells since the films either delaminated directly upon “LiPON” deposition or once contacted with Li in the cell environment they will not further be discussed in this thesis. As mentioned the physical characterization of these films was more or less identical to the Pt coated YSZ samples.

Another interesting point about the thin films on Pt coated YSZ is that the films seem to be more stable against the temperature induced degradation above 650 °C. Fig. 41 shows a comparison between two LNMO thin films deposited at 550 °C and 850 °C on

Pt coated YSZ as well as a powder pattern for comparison. Despite the elevated deposition temperature that already caused film degradation on the samples deposited on silicon as seen in fig. 39, no clear signs of degradation are visible for these samples. As mentioned before the newly formed reflexes of the degradation phase might be masked by the substrate background but on silicon the degradation is accompanied by a reduction in reflex intensity for the remaining reflexes which is not seen in this measurement. Here the intensities remain mostly unchanged. This might be caused by the lower surface area of the film (as opposed to the powdered material) and shorter time span it is subjected to the elevated temperatures during deposition. The film on silicon possibly only shows degradation because it is already destabilized due to the incompatibility of the thin film orientation with the governing substrate. The exact reasons though remain unknown and further effects of film orientation or lattice strain were not explored in this thesis.

Since the goal was to prepare electrochemically active thin films for cycling the orientation of the thin films was initially not very relevant. The material is expected to be isotropic in electron and lithium transport and therefore there is no clear advantage between (004) or (111) orientation. For the deposition on silicon it was therefore decided to remain below the obvious degradation temperature and a deposition at 550 °C was favored due to the better crystallinity. This parameter set was chosen as opposed to 650 °C since the change in preferential orientation was not expected to have a direct impact on electrochemical cell performance while lower crystallinity generally does have negative effects. For Pt coated YSZ the visible temperature effect on the thin films was rather minor and a lower deposition temperature was favored. The thin films deposited at higher temperature tended to delaminate upon “LiPON” deposition due to adhesive problems between LNMO and Pt. This was already described by Mareike Falk and was the reason why she opted to deposit very thin films in her work. This also allows for a more direct comparison between the two substrate materials. As later experiments would show the mechanical stability of the layer system was in many cases a much bigger problem than the crystal properties of the thin film. This meant that in the case of sapphire substrates for example whole arrangements of samples could not be further characterized and the implications of possibly observed differences in the film properties for the battery and cycling behavior could not be measured in functioning all-solid-state cells. While the result that certain configurations of layer system do not work due to their mechanical properties is a definite one it also is somewhat unsatisfying.

12.3 Considerations about the formed LNMO phase

From the XRD measurements shown above it is not easily determinable if the deposited LNMO phase corresponds to the ordered or disordered spinel phase. Due to the deposi-

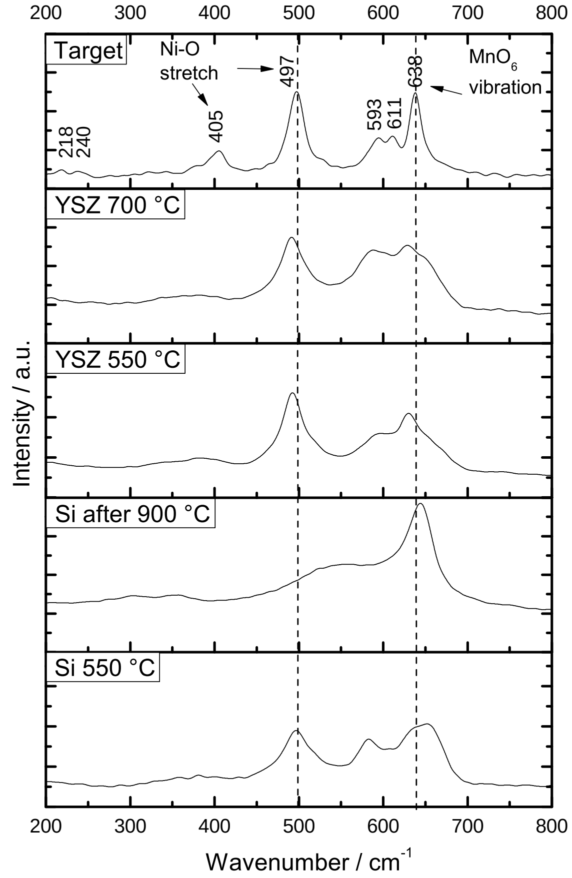

Figure 42: Raman spectra for various PLD thin film prepared on different substrates and at different temperatures. A spectrum for the target powder is also given which shows indication of the ordered spinel phase while most thin films appear to crystallize in the disordered phase.

tion temperature of less than 700 °C the formation of the ordered spinel with space group $P4_332$ is expected but this cannot be derived from the XRD data since the patterns of both phases are quite similar and a Rietveld refinement of the data is difficult due to the preferential orientation, film strain and in case of YSZ substrates the large amount of background reflexes. In order to clarify the formed phase Raman spectroscopy was employed. The main difference between the two phases consist in the ordering of Ni and Mn atoms in their respective positions. The implications of this is that a) in the ordered spinel phase manganese is expected to only exist in the formal +4 oxidation state while it has a mixed oxidation state in the disordered phase and b) the symmetry of the system is reduced for the ordered phase. This leads to a shift in the vibration of the Mn-O octahedral vibrations due to the oxidation state of the manganese and to the appearance of additional Raman bands due to the lowered symmetry. The introduction of nickel into the manganese spinel system also causes additional bands for the Ni-O bond stretching to appear that are of course not present for the pure manganese spinel while the Mn-O octahedral vibrations can be comparable between the two system.

Fig. 42 depicts some Raman spectra measured for PLD thin films deposited on different substrates and at different temperatures as discussed in the previous section. A spectrum for the target material is also given for comparison. The bands of the target material can be attributed to Ni-O stretching vibrations at 405 cm^{-1} and 497 cm^{-1}, the Mn-O octahedral vibration at 638 cm^{-1}, a split signal of octahedral vibrations at 593 cm^{-1} and 611 cm^{-1} that corresponds to the Ni and Mn ordering in the phase and some small bands at 218 cm^{-1} and 240 cm^{-1} that arise from the lowered symmetry in the ordered spinel phase. Typically for the ordered spinel phase the bands just above 200 cm^{-1} are visible and the band at 405 cm^{-1} is sharp while the bands at 593 cm^{-1} and 611 cm^{-1} are split into distinctive signals.[82,83,132,133] For the disordered spinel phase the lower energy vibrations are not visible, the Ni-O stretching vibration at 405 cm^{-1} is broad and the octahedral vibrations corresponding to the Ni/Mn ordering do not show clear distinction and appear mixed because Ni and Mn exist in mixed crystallographic positions throughout the crystal. The spectrum shape of the target material therefore corresponds to the ordered $P4_332$ phase of LNMO even though the bands at lower energy are somewhat weak.

In theory the position of the large band at 638 cm^{-1} can be interpreted regarding the oxidation state of the manganese but here it is necessary to note that the measurement was carried out with a grid resolution of 9 cm^{-1} to 15 cm^{-1} meaning the error of the peak position can be up to 15 cm^{-1} and the expected shift in the Mn-O vibration is smaller than this error. On closer inspection it can be seen that the absolute position for example of the Ni-O stretching vibration is also not consistent between the measurements and varies in the mentioned range. This is a limitation of the measurement setup because while the spectrometer allows measurement at higher resolutions (3 cm^{-1} - 5 cm^{-1}) the signal intensity with these parameters is lowered. Even with a very long measurement time only very low fidelity spectra could be obtained with higher resolution and the lack of quality would negate all that could possibly be gained through the higher resolution. Increasing the laser energy for a stronger excitation is also problematic for this material because sample damage can easily occur for manganese based oxides. The analysis of the spectra is therefore limited to a more general discussion of the spectrum shape.

For the PLD thin films prepared at low to intermediary temperatures similar Raman bands to the target material can be observed. The thin films differ though in that no low energy bands are observed, the Ni-O stretching vibration at 405 cm^{-1} is very broad to the point of being difficult to recognize and the Ni/Mn ordering vibrations have combined. This is clear indication that the thin films crystallize in the disordered $Fd\text{-}3m$ phase at all conditions measured. For the high temperature sample that was measured after temperature treatment in the XRK chamber of the XRD (temperature dependent

XRD measurement shown in the previous section) the Raman bands of the Ni-O stretching vibrations have completely disappeared indicating that the material has completely degraded and no longer exists in the spinel structure as before. The spectrum shape of the degradation product is similar to layered manganese based oxides for example MnO_2 but due to the low resolution no information on the exact peak position and therefore the manganese environment can be given. Interestingly no indication of NiO that would be expected around 500 cm^{-1} can be seen in the data. This can possibly be explained by the higher amount of manganese based oxide in the film (due to the stoichiometry) and subsequent suppression of the nickel oxide bands or due to surface effects since Raman spectroscopy is a surface sensitive method. Since the XRD data was inconclusive in regards to which oxidic component forms the resulting mixed cationic oxide might only exhibit Raman bands typical for the Mn-O vibration.

For the sample deposited at 700 °C on YSZ/Pt it can be seen that the distinction of the different bands between 550 cm^{-1} and 700 cm^{-1} already starts to suffer due to the deposition parameters being close to the decomposition range of the material. Since the effect was not clearly observed in the XRD data this might be a surface effect since oxygen loss at the thin film surface is expected to occur before significant loss in the bulk of the thin film. The Ni-O stretching vibrations are also not directly affected by the higher deposition temperature indicating that the ordering (or disordering) of Mn and Ni has a stronger effect on the Raman data in this case than the formation of a degradation phase. Furthermore in the work of Feng *et al.*[83] the lithium stoichiometry influences the shape and position of the metal vibration bands and generally a lithium deficiency (in the case of Feng *et al.* 10 %) leads to blurring of the bands in that region. In other words as in the XRD data there is no clear indication that the PLD thin films on YSZ/Pt degrade significantly at 700 °C as opposed to the films on silicon.

For the silicon sample the comparison with the powder data confirms that the deposited films indeed represent the LNMO material at this temperature while as mentioned the XRD data was not material specific due to the reduction in visible thin film reflexes because of the strong preferential orientation. In fact the differences between the various PLD thin films respective Raman spectra is not in the overall shape of the spectrum but more in the general intensity and relative intensities of the different modes. This might be related to differences in the defect structure or crystal size of the different thin films that can be expected due to the various deposition temperatures and growth orientations. Lattice strain can also influence the intensity of the vibrational modes.

Fig. 43 depicts Raman spectra of the target pellet measured with different setups. Each measurement was performed on a new site and the amount of accumulation time and co

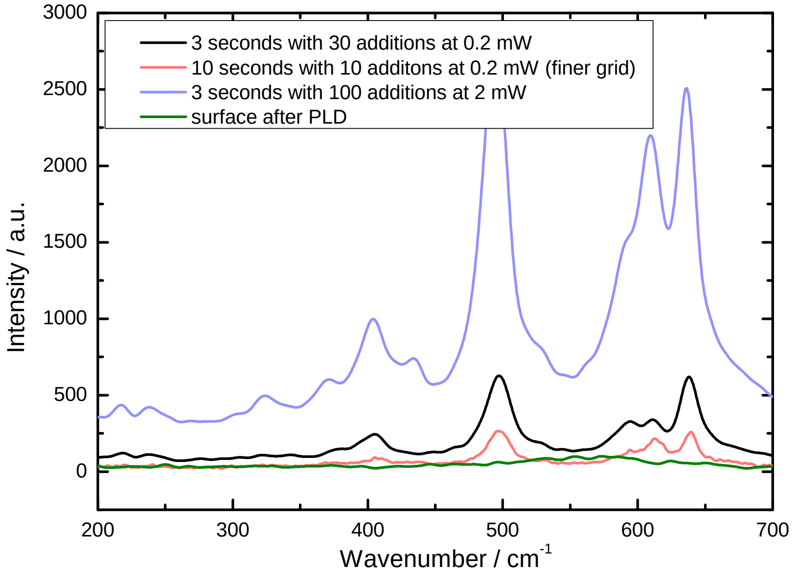

Figure 43: Raman spectra of multiple spots on the same LNMO target measured with different setups (energy, accumulation time, co additions and resolution grid). After subjection to the PLD laser the material is degraded.

additions was varied (3 s, 30 additions for example as opposed to 3 s, 100 additions) as well as the laser energy and the resolution grid. Initially the black and red curve can be compared to judge the influence of the higher resolution measurement grid. The overall intensity is lower and it is necessary to increase the accumulation time to achieve similar intensity (the amount of co additions was lowered to maintain roughly the same measurement time and therefore keep the time the spot is subjected to the laser consistent). The spectrum shape does not change significantly but the increased measurement resolution is negated by the overall lower quality of the data leading to no additional gain in information. The blue curve showcases the effects longer exposition to the laser and higher energies have on the sample. The intensity of the spectrum is increased but the relative intensities of the double peak at around 600 cm^{-1} are changed. Since other Raman bands are still present (especially the bands at around 200 cm^{-1} to 250 cm^{-1}) it is unlikely that a phase transition to the $Fd\text{-}3m$ phase has already occurred. This indicates that it is difficult to formulate “optimal” measurement conditions and a balance between intensity and exposure time/energy has to be struck. The green curve additionally shows that it might be irrelevant to discuss the exact crystal phase of the target material because after the surface was subjected to the high energy of the deposition laser no defined Raman modes can be measured. It is therefore unlikely that the crystallographic properties of the target material outside of mechanical and compositional parameters have a large influence on the resulting thin film material. The thin film material is of course subject to the same measurement problem as the bulk material is.

12.4 Spin coating of LNMO materials

Due to the very poor electrochemical performance of nearly all LNMO samples prepared via the PLD process (as will be discussed in section 13). The material was additionally prepared via spin coating from an aqueous solution of the corresponding metal salts based on the work of Gellert *et al.*.[37,54] The method offers several advantages when compared to the PLD process but also some severe disadvantages. Since no vacuum is required for the deposition process the reduction of the material is less favored and the formation of oxygen deficiency is suppressed because working in air i.e. higher oxygen partial pressure is possible. These conditions are also closer to the preparation conditions of the bulk material which is also typically prepared in air. The nature of the substrate is typically less important for spin coating since epitaxial growth effects are not expected and the resulting films are not necessarily orientated which is expected for PLD thin films or sputter deposited films in most cases. On the other hand film thickness cannot be as easily controlled as for PLD deposition and to achieve film thicknesses that are comparable to the PLD films (700 nm to 800 nm) multiple layers have to be coated. Since the previous layer has to be fixated before the next layer can be deposited a temperature treatment of the sample after each layer is necessary (i.e. heating the sample to 600 °C to remove organic solution components and precrystallize the layer). Multiple layers have to be deposited (up to 20 layers in total) and in order to produce a sample in a reasonable amount of time heating and cooling times of the layers in between deposition has to be rather quick. The recipe of Gellert *et al.* suggests a temperature treatment of 4 minutes for each layer so after each layer the sample was put directly into a preheated oven for 4 minutes. This rapid heating and cooling introduces a lot of thermal stress into the sample and therefore poses an additional challenge for the substrate material.

Out of the tested substrate materials (stainless steel, silicon, YSZ and sapphire each also in a Pt and Au coated variant) only stainless steel was able to withstand the preparation conditions. For the silicon substrates either cracking during the process would occur or the resulting thin films had severe adhesion problems often leading to a delamination of the thin films upon cooling or as soon as any additional stress (for example “LiPON” deposition) would be put on the sample. Applying different metal coatings to the single crystals could not improve this behavior significantly either because the metal thin films themselves had adhesion problems (most prominent for gold on silicon which is known to cause problems) or the LNMO thin film adhesion to the metal layer was not significantly better than to the pure substrate. The steel substrates generally had no noticeable adhesion problems which is probably related to their slightly rougher surface properties. Stainless steel substrates were purchased without any surface finish from the supplier. The substrates were then manually polished using the method described in the experi-

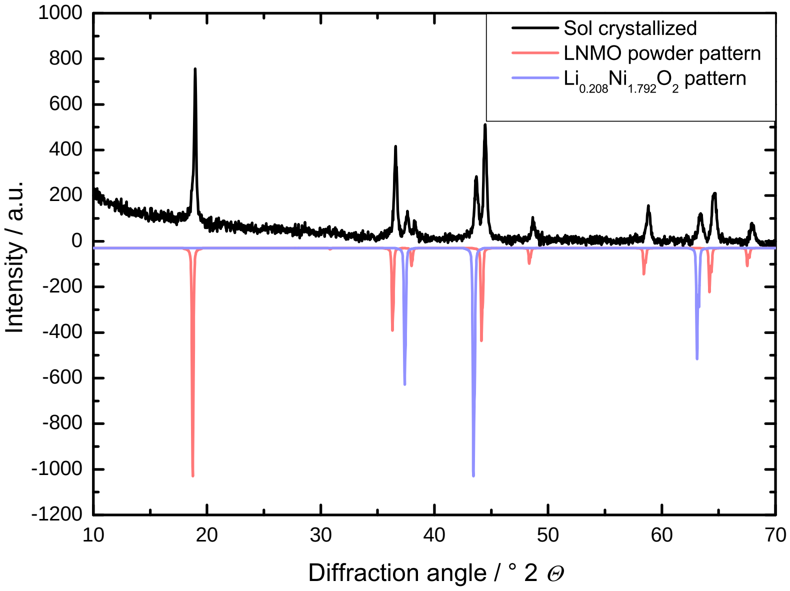

Figure 44: XRD pattern of LNMO powder crystallized from the liquid sol for spin coating preparation. Patterns for the LNMO powder material and a reference for the clearly visible rock salt impurity phase are given.

mental section but the surface roughness achieved with this method is not comparable to the smooth surface of industrially produced single crystal substrates. The lowest possible roughness achievable with this setup is ca. 20 nm to 50 nm due to the granularity of the polishing solution but the real roughness is somewhat higher due to polishing artifacts and macroscopic scratches on the surface. Unfortunately given the limitations of the polishing setup these scratches cannot realistically be avoided, range in the order of a few hundred nm to a few µm deep and are not always visible to the open eye. Of course the increased roughness does not only have positive effects on the adhesion but also negative impact on the cell performance as will be shown in the electrochemical characterization.

The material deposited via spin coating was characterized by XRD in two ways. First direct XRD patterns of the thin films were measured and second 1 ml of the liquid sol was heated to 700 °C for 4 hours and the resulting powder was measured. Fig. 44 depicts the XRD pattern obtained for this powder sample. It is apparent that in addition to the expected LNMO phase a rock salt type impurity phase has formed. This is in congruence with the literature described earlier and the degradation data obtained in this thesis by temperature dependent XRD measurements. Although the material is heated in air oxygen loss and impurity formation still occurs possibly because the amount of material heated was very minimal and therefore a large amount of surface area was exposed. Otherwise the expected spinel LNMO phase has formed. The pattern given here for the rock salt impurity phase is a sample pattern based on a Li enriched NiO phase. As mentioned before the pattern of the rock salt phase matches a multitude of different Mn, Ni and Li

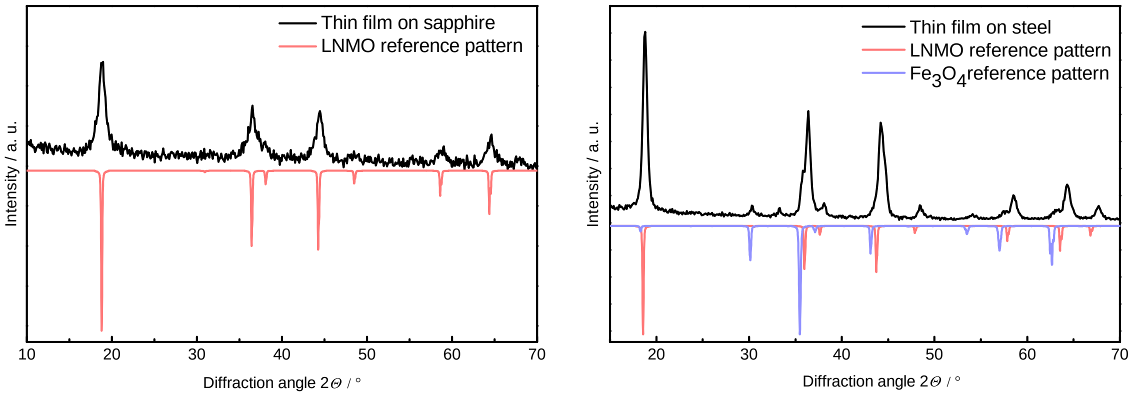

Figure 45: Grazing incident XRD measurements of LNMO thin films on sapphire and stainless steel substrate deposited via spin coating.

mixed oxides of the type MO and likely the phase consists of a mix of these oxide phases that all have very similar XRD patterns regardless of individual stoichiometry. The reason why it is assumed that the impurity mostly forms due to the temperature influence and not because the spin coating mixture has the wrong stoichiometry for example is that no clear indication of the same impurity phase can be found on the thin film samples.

Fig. 45 depicts grazing incidence measurements of spin coated thin films deposited on sapphire and stainless steel substrates. For these samples it was necessary to perform grazing incidence measurements since especially for the stainless steel substrate the strong substrate reflexes and the strong background noise made typical data difficult to interpret. Note that as mentioned before the thin film deposited on sapphire was of rather low quality due to adhesion problems and the signal intensity is therefore diminished for this sample. The measurement is given as comparison since the data for the stainless steel substrate shows that despite an incident angle of only 0.5 ° residual intensity of an iron oxide phase can be detected and the sample on sapphire shows no reflexes attributed to the substrate. The iron oxide phase is not necessarily part of the deposited thin film but likely only present at the edge of the thin film but to explain this it is necessary to briefly describe the spin coating setup.

The stainless steel substrates used were as described in the experimental section polished metal discs with a diameter of 12 mm and a thickness of about 500 µm. The spin coating solution was an aequous solution with very low viscosity and due to the forces applied to the coating film during the spinning of the disc an area about 1 mm thick at the edge of the sample disc was typically not or only partly coated with the thin film due to shearing of the coating solution. For the usage of the sample in the solid state cells this was negligible because the Li counter electrode used was 6 mm in diameter and the area of uniform film deposition was about 9 mm to 12 mm but for the XRD measurement this means an area at the edge of the steel sample was subjected to elevated temperature in oxygen without being coated leading to the formation of a slight oxidation layer. Due to the grazing incident conditions in the measurement this thin layer at the sample edge is still visible in the data also because the edge of the sample is generally somewhat rougher due to the polishing process. The reflex positions of the iron oxide are generally slightly towards lower diffraction angles when compared to the LNMO phase which causes the formation of a shoulder for almost all LNMO reflexes. Estimation from a very basic refinement suggests a phase composition of roughly 90 % LNMO to 10 % iron oxide. The reflex position of the iron oxide phase somewhat overlap with the reflexes expected for the possible LNMO degradation phase (ref. fig. 44) but the appearance of additional reflexes not found in the rock salt degradation phase reinforces that the present phase is iron oxide.

The iron oxide reference pattern given here is an example, the surface layer on the substrate likely consists of a mixture of different oxide phases. Other oxides like Fe_2O_3 (most prominent reflex at 33 °in the graph) or iron itself explain the reflexes not explained by fig. 45 but are not shown to prevent clutter in the graph. A comparison measurement of just the steel substrate treated in the same manner as the samples depicted here but without the metal salts in the spin coating solution exhibits the same iron and iron oxide reflexes under grazing incident conditions. The mismatch between expected and observed reflex positions for the LNMO film can possibly be explained due to strain in the thin film For the sample deposited on sapphire no clear indication of any impurity phase can be found although in this measurement the expected impurity reflexes are somewhat masked by the rather low intensity of the pattern overall caused by the lower sample quality as mentioned above. Compared to the crystallized sol though the composition of the sample even if impurity phase is present is shifted towards the pure LNMO phase. This suggests that the strong degradation of the crystallized sol is because of the longer temperature treatment combined with the higher surface area and that for the thin film due to the short exposition time to high temperatures and the comparatively low surface area the formation of the rock salt degradation phase is less favored. Contrary to the PLD thin films the spin coated films show no preferential orientation and appear polycrystaline as expected since oriented growth is not typical for spin or dip coating.

Since the spin coated films showed some problems in the XRD measurements due to the forced use of substrates (iron oxide for steel and bad quality for other substrates), Raman spectra were measured to judge the formed LNMO phase. In congruence with the spin coating process described by Gellert *et al.* the samples were subjected to 700 °C for 8 minutes after all layers were deposited to crystallize the LNMO. This temperature is as shown right on the border between ordered and disordered phase formation with the ordered phase expected to form below and the disordered above this temperature. At this

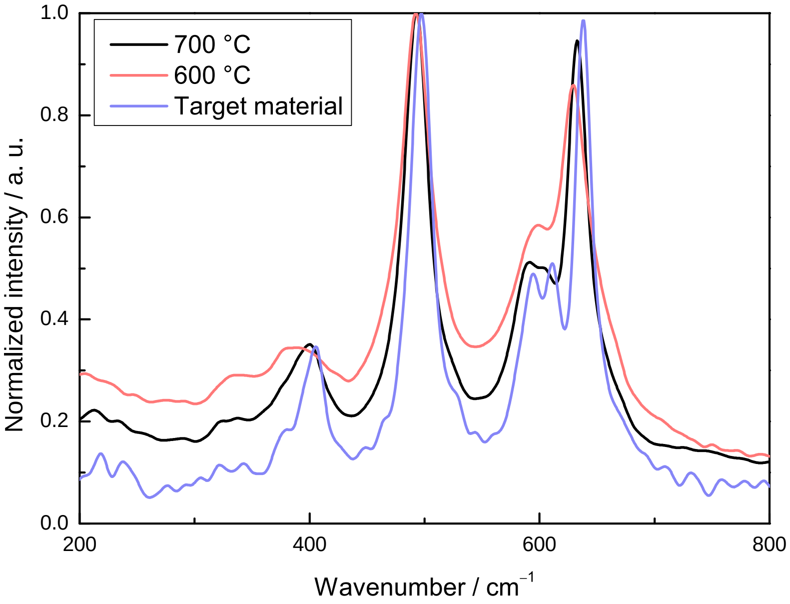

Figure 46: Raman spectra for spin coated LNMO samples on stainless steel heated to 700 °C and 600 °C respectively for crystallization. The Raman spectrum for the target material is also given for comparison.

point it is necessary to refer to the electrochemical data which will be described in section 13. Since for most of the LNMO films deposited a large part of the initial capacity was irreversibly lost in a first cycle reaction around 4.0 V the formation of the disordered spinel phase and the reduction of manganese in the system was suspected. In order to suppress this formation additional samples were prepared and only heated to 600 °C.

Fig. 46 depicts Raman spectra for two samples treated at different temperatures and a spectrum for the target material for comparison. Both films were deposited on stainless steel. The spectra for the two temperatures appear rather similar on first glance and match the expected spectrum for the target material quite well. As mentioned before the main factor in distinguishing between the ordered $P4_332$ and disordered $Fd\text{-}3m$ phase are the appearance of additional bands between 200 cm^{-1} and 250 cm^{-1}, the sharpness of the band around 400 cm^{-1} and the peak splitting of the bands at around 600 cm^{-1}. The sample at 700 °C matches the spectrum of the target material and represents the $P4_332$ phase while the sample at 600 °C appears closer to the spectrum expected for the $Fd\text{-}3m$ phase. This is surprising since the $Fd\text{-}3m$ phase would be expected for the higher temperature but not for the lower one. The measured intensity of the 600 °C sample is lower though (spectra are normalized to visualize relative spectra appearance better but higher background intensity for the 600 °C sample indicates lower overall intensity which is clear in the raw data not shown here). Even for the 700 °C sample the shape of the spectrum is not as clear as for the target material with for example the band splitting around 600 cm^{-1} being less defined.

As for the PLD samples measurement of multiple identical films yields not a completely consistent picture with intensity relations shifting and features appearing slightly more or less defined. This indicates that with the given preparation conditions the thin films are not completely phase pure but instead consist of a mixture between the two LNMO phases that are difficult to determine from the physical measurement data alone. Since this is the case judgment on the phase composition was mainly made by utilizing the electrochemical cycling data and judging based on the prevalence of manganese oxidation around 4.0 V.

Overall the Raman spectra of the spin coated thin films appear much closer to the expected shape seen for the target material as is the case for PLD thin films (ref. fig. 42). This is possibly caused by more favorable reaction conditions due to the higher oxygen availability in air as compared to the vacuum conditions in the PLD chamber or a decrease in film strain due to the preferential orientation that at least in case of the silicon substrates is forced by the substrate. A decrease in strain can only be argued for the spin coated samples on stainless steel substrates of course since samples on other substrates had serious adhesion problems.

Fig. 47 depicts HREM images of LNMO thin films on different substrate materials. For the sample spin coated on silicon a) large cracks are visible across the surface and the material is delaminating due to stress. It can also be seen that a “wavelike” microstructure has formed on the surface. The cross section c) shows that this effect is indeed a three dimensional distortion of the thin film surface. For the same deposition on YSZ/Pt this effect is not visible and the surface appears smooth and without any cracks and very small visible crystals. The cross section of this sample d) depicts again the smooth and flat surface and the individual layers deposited by the spin coating process are somewhat visible but it can also be seen that the contact between the underlying platinum layer and the YSZ substrate has deteriorated due to the temperature treatment visible as a small gap formation.

It should be noted here that the platinum deposited on the YSZ was annealed at 600 °C before the spin coating layers were applied to increase crystallinity and adhesion. The system is in general stable at these temperatures but the rapid change in temperature during the spin coating process seems to negatively impact the overall adhesion. As mentioned before it is not easily possible to reduce the temperature strain put onto the sample while maintaining realistic sample processing times and sample throughput.

Finally images e) and f) depict the surface of a LNMO thin film deposited on gold coated silicon via PLD at 650 °C (e)) and a spin coated film at 700 °C on stainless steel. The

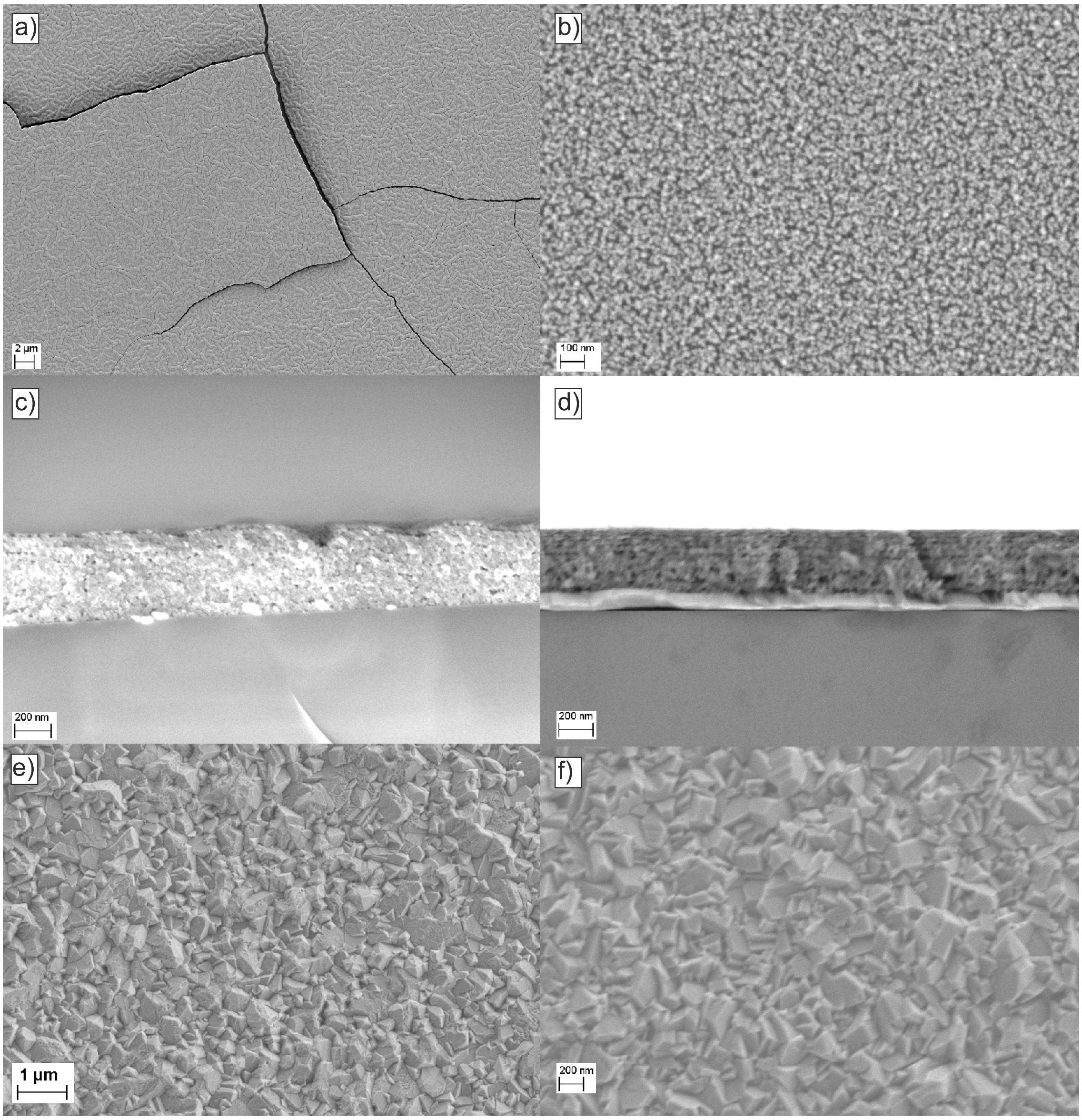

Figure 47: HREM images of LNMO thin films a) spin coated on silicon, b) spin coated on YSZ/Pt, c) cross section of the spin coating film on silicon, d) cross section of the spin coated film on YSZ/Pt, e) PLD deposited on gold coated silicon and f) spin coated on stainless steel.

surface of both samples appears rather similar even though different deposition methods were used. When compared to the spin coated film on YSZ/Pt it can be seen that the film on steel has a bigger average grain size which is possibly related to the rougher surface of the steel substrate facilitating crystal growth. Cross section data for the samples on stainless steel was not measured due to the difficulty in preparing a clean cross section on steel substrates. While it is possible to cut the substrate and subsequently polish the cross section mechanically or via ion polishing the result was still a very damaged cross section with parts of the thin film breaking away from the edge or the structure of the cross section being obviously changed by the polishing method so that no relevant information about the growth properties could be extracted. For the samples on single crystal substrates this was not a problem since cross sections can easily be prepared by cracking the substrate in the center. The resulting cross section at the breaking edge was often very well defined. The HREM images also provide information about the film thickness of the spin coated films which was on average about 500 nm for 10 deposited layers and about 250 nm for 5 layers deposited leading to a thickness per layer of about 50 nm which is in the expected range and in agreement with Gellert *et al.*

In summary the physical characterization shows that with all methods used in this thesis the LNMO material can be deposited on a multitude of substrates. The material degrades at elevated temperatures above 700 °C under low vacuum conditions but remains seemingly phase pure below that temperature. The phase composition achieved with PLD and spin coating deposition seems to be a mixture between the $P4_332$ and $Fd\text{-}3m$ phase with the PLD samples tending more towards the disordered oxygen deficient phase and the spin coating films appearing more balanced or tending towards the $P4_332$ phase. Since the disordered spinel phase is formed at least partially in all films rock salt impurity phases are still expected even though they cannot conclusively be identified by XRD or Raman measurements which also means that some level of Mn^{3+} activity in the electrochemical measurements is expected (and seen (ref. section 13)). Despite variations of temperature treatments or annealing time this could never fully be prevented. The main problem facing all-solid-state cells based on the LNMO system in this thesis though was not the production of chemically correctly formed LNMO thin films but instead of mechanically stable full systems. Thin films would often appear fine after deposition but easily delaminate after some additional stress either through the “LiPON” deposition or through cell assembly with metallic lithium electrodes being applied leading to immediate cell failure and short circuiting. For the PLD deposition Pt or Au coated sapphire yielded almost no stable samples with direct contact problems between the metal layer and the substrate even with multiple annealing steps tested. Platinum on YSZ produces more stable substrates but as already shown by Mareike Falk adhesion of LNMO on these samples is problematic unless using very thin LNMO films which in this thesis was not feasible because of the conditions set by the electrochemical characterization.

If spin coating methods are employed this problem becomes more severe due to the harsher temperature treatment and leads to almost no useful samples being produced. The only substrate able to withstand the conditions of the spin coating process was stainless steel but the failure rate of these samples was rather high due to other reasons as will be discussed in the electrochemical characterization. Because of the instability of the full systems the sample preparation is often limited by these external parameters and certain experimental setups that should in theory improve certain aspects of the LNMO thin film can sometimes not be tested in the battery because the system can simply not be assembled without being destroyed in the process. The stress applied to the thin film by applying an additional solid electrolyte layer and direct contacting with Li metal seems to be significantly higher than if liquid electrolytes are used. This is in contrast to the LTO system for which it is comparatively easy to produce chemically correct LTO thin films but these thin films are also a lot more robust in their contact behavior inside the all-solid-state system leading to mechanically highly stable systems. To give a comparison and perspective for the LTO system it was always possible to peel the lithium electrode off the sample after the electrochemical measurement without damaging the LTO or "LiPON" thin film (aside from surface damage caused by the Li contact) even if significant force had to be used but for the LNMO thin films this was only possible on stainless steel substrates without destroying the entire layer system.

13 Electrochemical characterization and processing setup for LNMO based batteries

Since the impedance characterization of the LNMO thin film system in this thesis is not as extensive as for the LTO system, results from the impedance measurements will be given in this section together with the cycling data to describe the general cell behavior of LNMO thin film cells. The initial samples for LNMO cells prepared in parallel with the LTO cells were in general non functional. The samples were prepared via PLD on silicon substrates and showed no electrochemical activity. Fig. 48 depicts the Bode plot of such a cell and shows that it exhibits very high resistance in the middle to low frequency range. As with the LTO cells the process in the high frequency range can be attributed to the electronic conduction through the silicon wafer and shows comparable values and behavior. The middle to low frequency range though is not necessarily directly comparable. For the LTO system in this frequency range the ionic conduction through the LTO film was shown to be rate limiting but for the LNMO thin film this is not an expected behavior since the ionic conductivity should be higher. The resistance depicted here also extends into the mega ohm region and is vastly higher than any resistance observed for the LTO system outside of the blocking behavior at the very start or end of a cycle. In regards to results that will be shown in the following the electronic contact to the silicon wafer seems to be the main factor for this total blocking behavior. Measurement data on the early cells is limited because few reasonable measurements can be obtained from non functional cells and no direct experiment probing the contact could be made. Later cells on YSZ/Pt

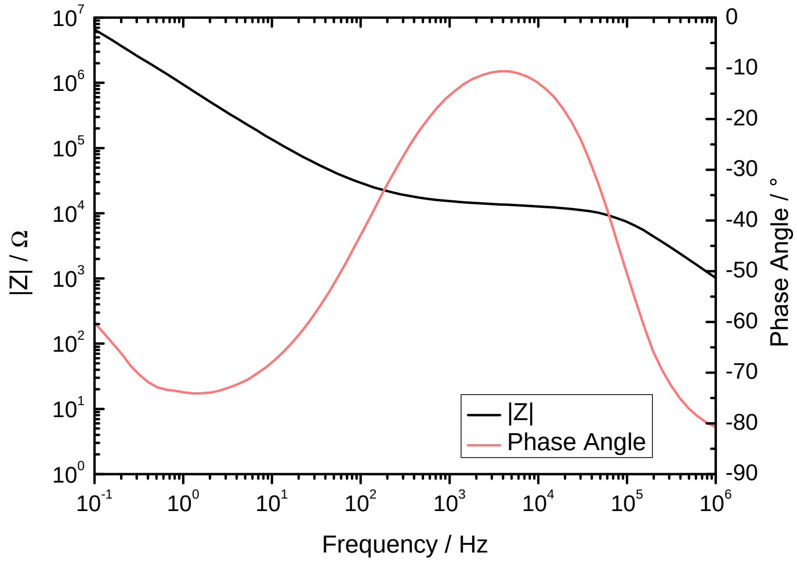

Figure 48: Bode plot of a LNMO thin film all-solid-state battery deposited via PLD on a silicon substrate. The cell exhibits very high resistance in the middle to low frequency range completely blocking any electrochemical activity.

and sapphire/Pt also deposited via PLD did show cell activity and did not exhibit this massive resistance so this indicates that the charge transfer between silicon and LNMO is problematic.

The nature of this blockage is difficult to determine due to the lack of reliable data and the fact that the electronic properties of the LNMO phase are strongly dependent on the nickel content and the prevalence of Mn^{3+} in the phase as shown by Lazzaraga *et al.*.[134] If the formed phase is not the stoichiometric ordered spinel phase, as the physical characterization (and data that will be shown in the following) seems to suggest, Mn^{3+} exists in the material and leads to an improvement of the electronic conductivity. The phase composition present at the interface is unknown. For the LTO system the composition at the interface could be extrapolated from the contact properties and resistances in dependence to the state of charge. No such measurements were possible with the LNMO system. Discussing the band structure at the interface therefore is equally difficult. The higher cell polarization and possible larger voltage drop at the silicon/LNMO interface that is prevalent due to the high cell voltage of LNMO/Li cells might be part of the reason why this interface is much more problematic than is the case for LTO based systems. The problem is isolated to the silicon substrates though and as with the LTO system silicon was quickly abandoned as a substrate material due to the various problems it causes in the all-solid-state system. All samples further discussed for the LNMO systems will be on sapphire/Pt and YSZ/Pt for the PLD samples as well as on stainless steel for the spin coating samples. Most PLD samples will be on YSZ/Pt due to the adhesive problems on sapphire mentioned in section 12 but for non short circuited cells both substrates are functionally identical for the electrochemical characterization.

13.1 General cell properties

Fig. 49 depicts a LNMO thin film system PLD deposited on Pt covered sapphire at 550 °C and at 5 Pa pure oxygen. The data shown is the first and second charge and discharge cycle for the resulting LNMO/“LiPON”/Li all-solid-state battery. Initially it is notable that the starting cell potential is not close to 4.7 V or even 4 V but is at around 2.6 V. In the early stages of the first cycle the first plateau reached is therefore the tetragonal/cubic phase transition of the system as lithium is extracted. This indicates that for this sample the lithium content in the thin film is higher than expected, beyond the expected stoichiometry and at the start of the cycle the material does not exist in the desired cubic spinel phase. This is surprising since lithium loss typically is expected especially since the deposition pressure in this case was somewhat lower than for other samples that will be discussed shortly hereafter. The cell transitions into a large plateau at around 3.9 V, a short inclined plateau at around 4.0 V and a very undefined plateau at around 4.6 V to

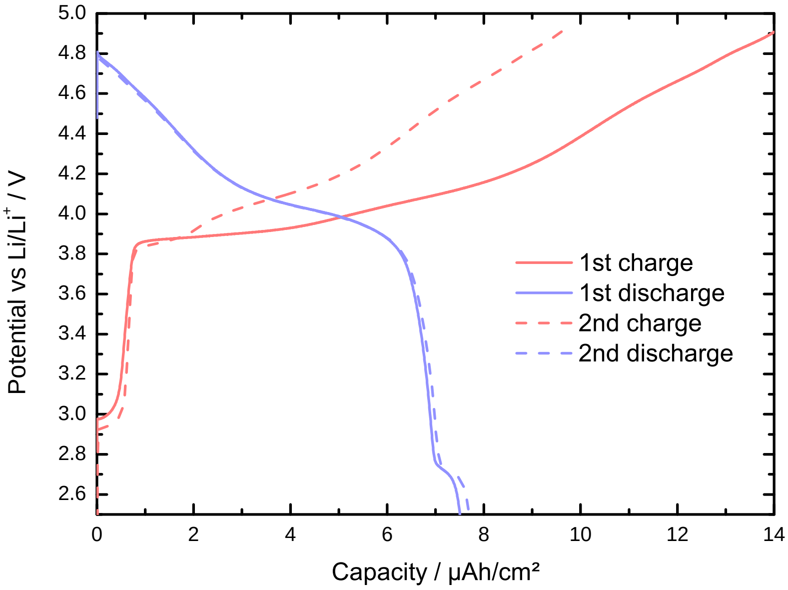

Figure 49: First and second cycle charge/discharge profile of a LNMO thin film battery on sapphire/Pt substrate PLD deposited at 550 °C and 5 Pa oxygen (3.5 µA/cm^2). Strong first cycle irreversible effects are visible in the data.

4.7 V. The charge insertion around 4.0 V is typically attributed to Mn^{3+} that exists within the phase either because of the formation of the disordered phase or because of lithium manganese oxide impurity phases. The undefined plateau around 4.7 V corresponds to the desired Ni transitions but is not well developed. The charge inserted at 3.8 V is not readily explainable. If the phase composition of the material is not as expected as suggested by the high content of Mn^{3+} in the thin film, the transition could consist of a $Li_xNi_{1-x}O_2$ impurity phase. This phase might form together with a $LiMn_2O_4$ phase or, as considered by Pröll *et al.*,[135] is a residual charge transfer based on the tetragonal/cubic phase transition which is present when the system is cycled below ca. 3.0 V. In any case the first cycle effects visible are highly irreversible and only about 50 % of the overall capacity inserted can be extracted again mostly from the Mn^{3+}/Mn^{4+} transition and some from the higher voltage nickel transition.

In the second cycle the plateau at around 3.8 V is vastly reduced in capacity and corresponds now more closely to the effect observed by Pröll *et al.* for residual phase transition capacity since the cell was cycled back to the initial EOC. Capacity loss of LNMO based all-solid-state cells in the first cycle is an effect also observed in the literature[51] but typically the percentages are not as high. Since the nickel transition at higher voltages cannot be sufficiently addressed in these samples the material deposited is likely not the desired LNMO phase or at least not at the quality level desired. As mentioned in the physical characterization due to the preferential orientation in the XRD data and the similar Raman data for both phases this is only evident once the system is cycled. Because of this it

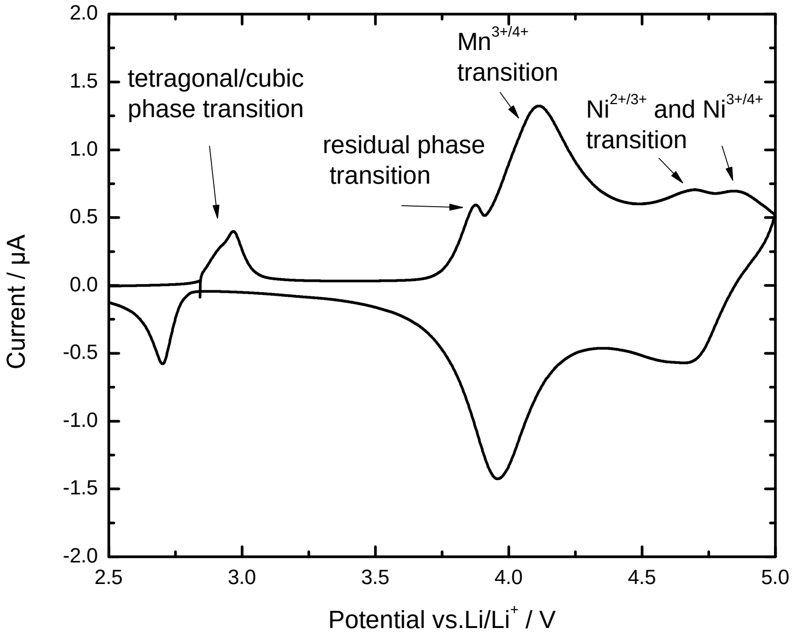

Figure 50: Cyclic voltamogramm of the LNMO sample depicted in fig . 49 the nickel transitions at high voltages are clearly visible here even though they are less defined in the cycle profile.

cannot be determined if the initial deposited LNMO thin film was already not formed with the correct phase composition or if the later treatment of the sample (“LiPON” deposition, cell assembly) caused a lithium enrichment in the film. It is possible that additional lithium was incorporated into the thin film during the “LiPON” sputter deposition since lithium excess is not a typical phenomenon of PLD deposited thin films. The oxygen partial pressure during the deposition is another possible explanation for the prevalence of reduced manganese species in the sample. In the physical characterization not much difference was observed between samples deposited at high or low oxygen partial pressure which is partly because the pressure range for deposition is limited to roughly one order of magnitude above the 5 Pa mentioned here. Due to the experimental setup partial pressures above 40 Pa are not possible with pure oxygen while pressures above 20 Pa put a significant strain on the turbo pump due to the high gas influx.

Fig. 50 depicts a cyclic voltamogramm of the same sample and reinforces the general processes observed in the cycling profile. Additionally the high voltage nickel transitions are more easily discernibly in the CV data and confirm that besides the high amount of reduced manganese species and likely impurity phase formation the sample still contains the desired spinel phase and referring back to the profile data in fig. 49 about 1/3 of the overall charge insertion extraction is in the region ascribed to the nickel oxidation/reduction. Increased oxygen partial pressure to better facilitate manganese oxidation should therefore suppress the formation of the undesired impurity phases if they are a product of the PLD deposition and not introduced during a possible lithium enrichment in the sputter process or caused by other effects.

13.2 The manganese oxidation state and lithium enrichment

Fig. 51 shows data of a sample deposited at higher oxygen partial pressure of 20 Pa during the deposition. The desired reduction in reduced manganese species is only partly achieved. The initial potential of the cell is somewhat higher compared to the previous sample. The first plateau addressed during cycling now is located at 4.1 V and can therefore clearly be attributed to the Mn^{3+} transition while the previously observed transition at 3.8 V attributed to residual tetragonal/cubic phase transition or impurity phases is no longer visible. The overall capacity addressed through the Mn^{3+} transition is still in the range of 50 % overall cell capacity so the reduction in reduced manganese species is not significant. As with the previous sample after the first cycle most of the capacity, especially from the Mn^{3+} transition, is irreversibly lost. Cycles at reduced cycling current are given to show that this is not an effect of changing cell resistance and therefore higher overpotentials after the first cycle because even with reduced cycling current the cycles appear almost identical. The fact that the capacity in the first cycle is completely irreversible suggests that the thin film is still lithium enriched.

If the Mn^{3+} activity was caused by formation of the disordered spinel phase or the nickel

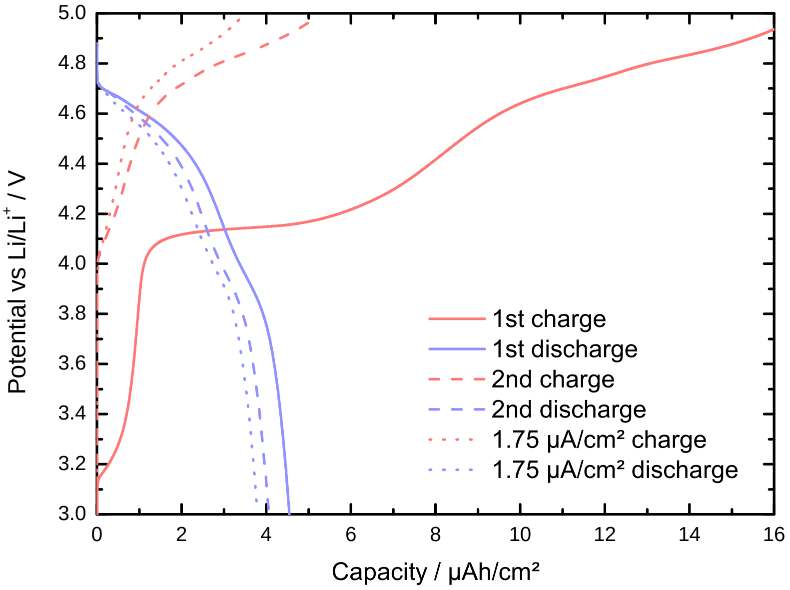

Figure 51: Cycle profiles of a LNMO thin film deposited on Pt covered YSZ at 500 °C and 20 Pa pure oxygen. The change in deposition pressure only has a minor impact on the overall cell behavior. Comparative data at lower cycling current of 1.75 µA/cm^2 is also given (standard cycling rate 3.5 µA/cm^2).

deficient pure manganese spinel it would be expected to be reversible since $LiMn_2O_4$ is a viable electrode material perfectly capable of reversible cycling. The phase is problematic in liquid systems since the manganese redox products tend to dissolve in the liquid electrolyte and therefore reduce overall capacity loss but in the solid state system this is not expected to happen. If the Mn^{3+} activity is instead caused by a lithium enriched phase in which manganese is reduced due to additional lithium incorporation the reinsertion of the lithium can only take place below 3.0 V which is outside the cycling window in this case. On the other hand the capacity extracted from the film in the first cycle was below the theoretical capacity of the material which does not suggest that additional lithium is extracted from the thin film. This can be an effect of incomplete film utilization though. In the literature the first cycle effect is known in recent publications about all-solid-state thin film batteries of the material[40,51] and in case of Li. *et al.* is also explained by additional lithium incorporated into (in their case sputter deposited) LNMO thin films. In their case though the first cycle capacity exceeds the theoretically expected capacity so that conclusions about the 4.0 V plateau are less ambiguous.

The nickel transitions at higher potentials are much more clearly defined in this sample and a step in the charge profile is visible in the first cycle when switching between both nickel transitions from +2/+3 to +3/+4. The capacity addressed through the nickel oxidation is only about 50 % of the overall cell capacity. In the second and further cycles the Mn oxidation at 4.0 V disappears almost completely but the capacity addressed through the nickel redox pairs also suffers a significant loss in between the first and second cycle leading to a capacity retention of only about 25 % after the first cycle. As mentioned before the overpotential for these cycles is not increased when compared to the first cycle so no significant additional resistance is introduced into the system in between cycles.

The Bode phase angle plot of the sample (measured after the first 5 cycles as with the LTO system) mainly shows two constant processes in the high frequency region and a lower frequency process that is somewhat undefined. The behavior at the start of the charge cycle is given as a reference but it should be noted that the impedance at the start of the charge and discharge cycle was identical and only at the end of the given cycle differences evolve. At the start of the given cycles the low frequency region does not show the same process as observed towards the end of the cycles. The characteristic of the low frequency process is not clearly identifiable as a CPE/R, CPE or Warburg like element but appears to be a mixture of these elements depending on the real cell state. It may be interpreted as a feature of the cathode that tends towards diffusive behavior at the end of the discharge cycle while appearing more like a very depressed semicircle at the end of the charge cycle. Since it is not clear what process exactly is shown here interpretation is difficult. If the system is similar to the LTO system the process could represent conduction

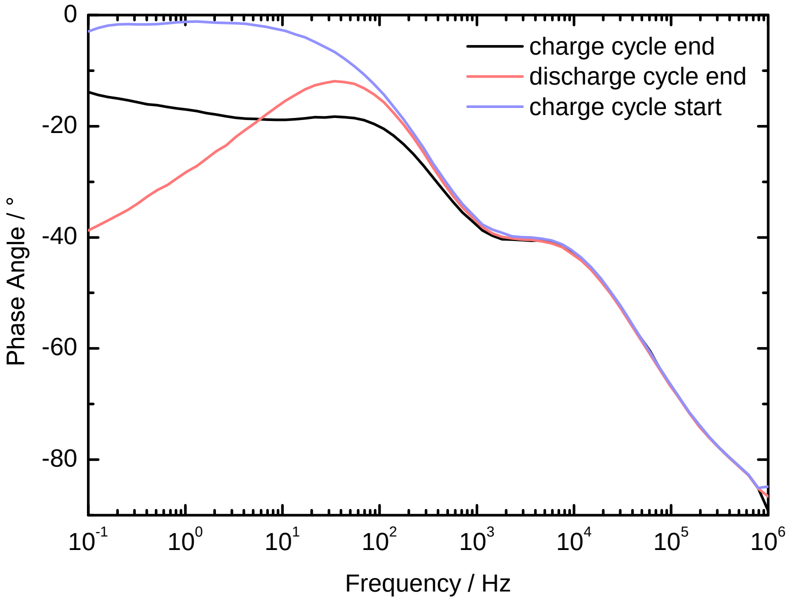

Figure 52: Phase angle plot for the LNMO thin film sample depicted in fig. 51. The end of both charge and discharge cycle is given as well as the start for the charge cycle. Note that the impedance spectrum at the start of the charge and at the start of the discharge cycle are identical so only one is given.

through the LNMO thin film but for LNMO it is also expected that the charge transfer to the “LiPON” phase is significant. Without further data this cannot be determined from this data alone.

Both processes (film conduction and charge transfer) are expected to be dependent on the state of charge because of the possible change of reaction kinetics at the interface and the expected change in transport properties of the LNMO thin film although the changes in transport properties are not expected to be as drastic as for the LTO system. The process visible in the high frequency region can as detailed for the LTO system be ascribed to the solid electrolyte conduction and shows similar values as expected since the electrolyte properties are not changed between systems (aside from possible differences in the charge transfer). The medium frequency range features another process that remains stable across the state of charge change. For the LTO system this was ascribed to the Li/“LiPON” charge transfer but for the LNMO samples the process was often enlarged when compared to the LTO system. The interface properties between Li and “LiPON” are not expected to change when utilizing a different cathode material and therefore no difference in this process would be expected. The higher cell potential introduced by the use of LNMO should be applied majorly at the electrolyte/LNMO interface. As shown in fig. 48 the electronic contact properties to the substrate material are likely of significantly bigger proportions in the case of LNMO as was the case for the LTO system. Small residual contributions of the electronic charge transfer are expected for the LTO system

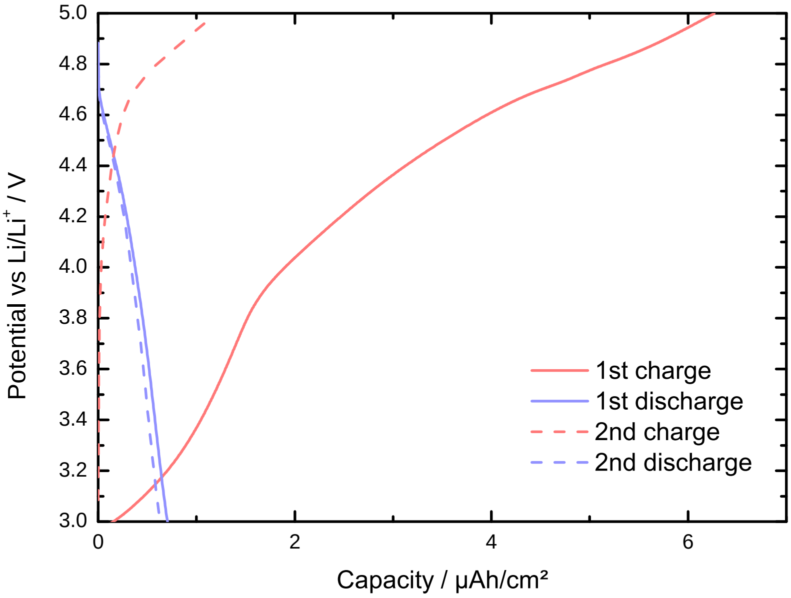

Figure 53: LNMO thin film prepared via PLD at room temperature on YSZ/Pt and subsequently post annealed in an oven at 700 ° C for 1 hour in air.

even using metallic contacts as outlined in section 11. If LNMO follows the same behavior but the effect is overall stronger due to the higher electrode polarization, as suggested by fig. 48, the residual charge transfer resistance when using metallic contacts is also slightly higher. The process might overlap in this frequency region with the Li/“LiPON” charge transfer resistance. This leads to the observation of a semicircle with a slightly increased size. The effect will be further discussed below.

Since further increasing the oxygen partial pressure during deposition was not possible additionally samples of LNMO were prepared by depositing the film with identical parameters but at room temperature and subsequently annealing the sample in an oven at 700 ° C for 1 hour to reproduce the powder preparation conditions. Fig. 53 depicts the first and second cycle data of a sample prepared this way. The prevalence of the manganese transition at 4.0 V is further reduced and is replaced by a distributed plateau between 4.2 V and 5.0 V but the overall capacity of the system suffers greatly and large parts of the achieved capacity in the first cycle is still irreversible. Due to the plateau being distributed over a larger potential range it is difficult to judge the proportions of the different redox processes involved. The reversible capacity now consists only of the nickel transitions but is extremely low so that the system can only barely be described as electrochemically active. Comparing the data to fig. 51 and 49 it seems the more the formation of the reduced manganese species is suppressed the more the reversible capacity and cyclability of the system suffers in return.

13.3 LNMO coatings and interface considerations

The low electrochemical activity of LNMO in solid state systems especially partnered with “LiPON” is an often considered point in the literature and might be based on another factor not yet discussed. Often when measuring impedance data these systems show a larger dominant low frequency process that constitutes a large part of the overall cell resistance. These processes in the low frequency region of the impedance are often ascribed to cathode processes and in the LNMO system especially a large charge transfer resistance between LNMO and “LiPON” is often shown to be the limiting factor for LNMO based cells. To overcome the poor electrochemical activity of the system coating materials are used to adress the limitations of the pure LNMO/“LiPON” contact. These coatings follow two different trains of thought. One idea is to improve the chemical interface between the two materials either by protecting the system from possible degradation or offering beneficial transport properties at the interface. The other concept described by Yada. *et al.*[40] aims to decrease the strong space charge layer formation in the electrolyte phase due to the high cell potential. Through the inclusion of high permittivity materials at the interface in small particles the space charge polarization is expected to be reduced near the particles and transport through the space charge layer is expected to proceed with less resistance.[40] For all thin films produced via PLD aside from the large irreversible capacity in the first cycle the cycling performance was extremely low with very low reversible capacity and also rather low peak currents in the cyclic voltamogram data.

In addition to the steps taken to reduce the prevalence of Mn^{3+} in the phase different coating materials were also employed to improve cell performance. As a coating material lithium niobate (LNO) and LTO were tested and both were applied via PLD and via ion beam sputtering with film thicknesses between 20 nm (ion beam) and 50 nm (PLD). For the dielectric interface modification a 0.008 wt% solution of barium titanate nanopowder (99.99 % ChemPUR, particle size 100 nm) in methoxyethanol was used in accordance to a publication from Yada *et al.* and dip coated onto the sample with a pulling rate of 2 mm/s as well as sprayed onto the sample using a pressurized air gun. Samples coated this way were dried in an oven at 100 ° C for an hour. It is important to emphasize that for the BTO coating no uniform film was deposited since this would lead to blocking of the cell kinetics but instead small particles were distributed across the surface.

Fig. 54 depicts a comparison of the different coating materials tested in first and second cycle profiles. In fig. 54 a) and b) the first charge cycle of the different samples is given versus the achieved capacity a) and normalized for the state of charge b) to better visualize the profile shape. All samples used for testing coating materials were prepared by PLD and post annealing as described above. Fig. 54 c) depicts the reversible capacity

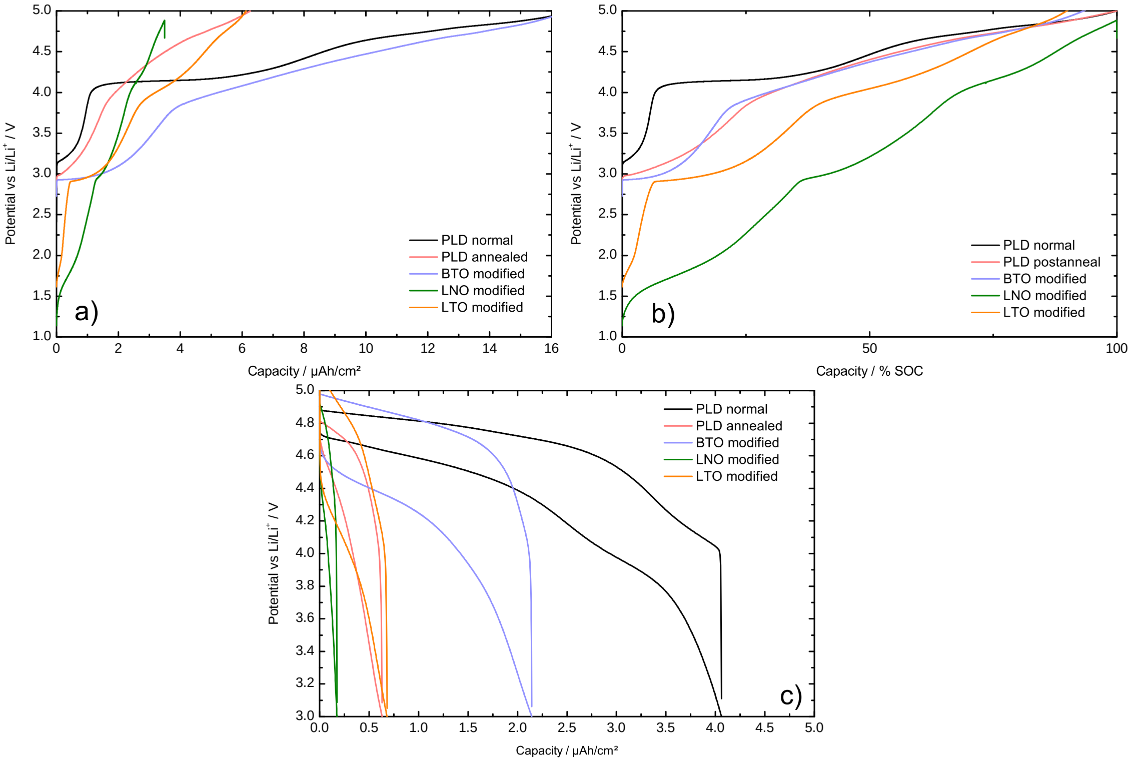

Figure 54: Comparison of first and second cycle data for LNMO films prepared with different coatings. LNMO films with coating materials were prepared by PLD and post annealing. The data shown is a) the first cycle charge step , b) a capacity normalized first cycle charge step to better visualize the profile shape and c) the reversible capacity in the second cycle in a hysteresis plot of charge and discharge step.

achieved in the second cycle in a hysteresis plot of both charge and discharge cycle.

The direct comparison of first cycle charge capacity a) shows that the PLD deposited normal thin film and the BTO modified post annealed thin film perform rather similar in the first cycle. While for the PLD thin film the 4.0 V transition is clearly defined the BTO modified film shows a more distributed plateau and a significant amount of charge is inserted around 3.0 V indicating a tetragonal phase transition at the start of cycling. Comparing the BTO modified film to the unmodified post annealed film the BTO modification clearly improves the first cycle capacity. As the normalized data in b) shows the overall profile shape of the unmodified post annealed sample and the BTO modified one is almost identical but the capacity achieved by the BTO modification is higher. The other two coating materials LNO and LTO do not perform as well. Capacity is either not increased at all for LTO or even reduced in the case of LNO coating. The profile shape in b) also indicates that a significant amount of charge is inserted at lower potentials of about 3.0 V indicating tetragonal transition. In the case of the LNO coating the starting potential is also very low featuring additional charge insertion below 3.0 V. Because the overall capacity of this sample is so low this might be a reaction of the coating material itself while most of the deposited LNMO film remains inactive. For both of these coatings

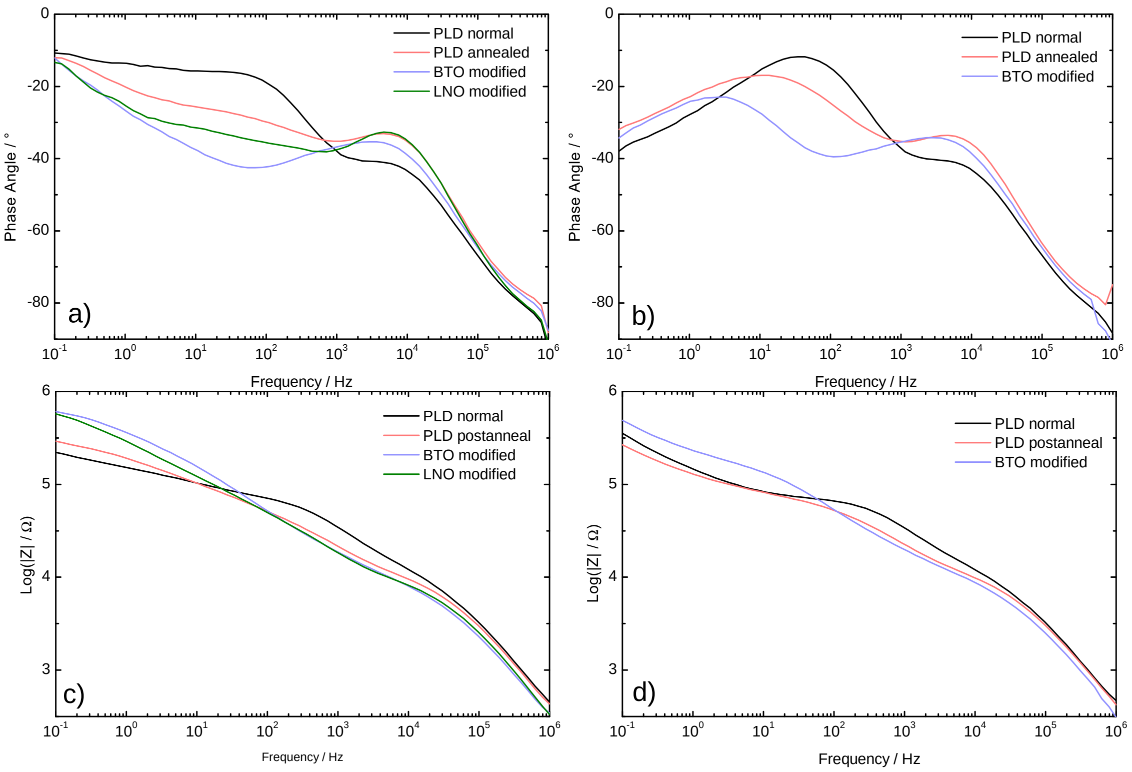

Figure 55: Impedance data of LNMO films prepared with different coatings. Given are a) the phase angle of the impedance at the end of the charge step, b) the phase angle of the impedance at the end of the discharge step, c) the value of the impedance at the end of the charge step and d) the value of the impedance at the end of the discharge step. Phase angle and value of the impedance were separated to reduce clutter in the graph.

the capacity inserted through the nickel transitions is very minimal.

The overall conclusion is that the samples annealed in air feature less defined manganese transition reactions in the first cycle and almost none in the following. The sample deposited normally in the PLD features the highest initial and reversible capacity but also very defined manganese oxidation and reduction in the first and following cycles. The BTO modification increases the capacity of the annealed LNMO film but does not change the profile shape and the other coatings do not have favorable effects. No samples feature both high capacity and a elimination of the manganese redox couple from the battery cycle. The reversible capacity in all cases is very low compared to the initial capacity and the theoretical capacity (estimated about 21 µAh/cm^2 for the given films) especially for samples without an active manganese redox couple in the cycling process.

Fig. 55 allows some conclusions about the resistive difference between the samples and about the influence of the coating materials. Depicted are the phase angle and value of the impedance at the end of the charge and discharge step. Focusing first at the phase angle of the impedance at the end of the charge step a) the data shows that for the medium frequency range around 1 kHz - 10 kHz the sample prepared normally in the PLD has the highest resistance. As described earlier this process is likely a combined system response from the Li/“LiPON” charge transfer resistance and residual charge transfer resistances at the thin film/substrate interface. It is therefore expected that the preparation method of the thin film has an effect on the substrate/thin film interface. In this case specifically the data suggest that the interface prepared under high temperature PLD conditions is of higher resistance than the interface prepared at room temperature and subsequently post annealed. This seems reasonable considering that samples prepared at higher temperatures often had problems with film delamination (as described in section 13) indicating a strong mismatch or film strain between substrate and thin film at high temperatures. It is also possible that the film composition change, caused by annealing the sample in air and leading to a higher overall oxidation state of the thin film, has favorable effects for the substrate interface. Considering that higher film oxidation leads to a reduced amount of Mn^{3+} and therefore reduces electronic conductivity in the thin film this effect might be of secondary importance.

For the BTO and LNO modified sample this frequency region is similar to the post annealed sample which is also expected since the surface coating at the LNMO/“LiPON” interface is not expected to have an influence on the substrate interface. In the following lower frequency region it is more difficult to discern between individual processes because in this region multiple processes seemingly overlap which can be seen in the broad, distributed spectrum shape in this region lacking clearly defined signal shapes. At least two possible contributions in this region can be inferred one around 100 Hz and one at around 1 Hz with further contributions possibly existing in the background. The contribution at 100 Hz is more pronounced and of higher resistance for the surface modified samples when compared to the post annealed or even normally deposited sample. This indicates that the process in this region is related to the LNMO/“LiPON” interface.

In all cases for modified or unmodified samples the resistance in this region is higher than for the normally prepared sample in the PLD and is generally highest for the BTO modified sample. This is surprising since comparing the post annealed and BTO modified sample the BTO modification did increase the capacity during cycling yet it seemingly introduces a higher resistance at the interface. Even though the battery capacity is not directly related to the cell resistance, higher cell resistances typically cause higher overvoltages. This can still allow for the same cell capacity albeit at different potentials but it is not reasonable that higher cell resistance has a positive effect on the capacity. This can only mean that the effects at the interface are not the cause for the higher capacity. The bulk properties of the thin film are not expected to change with the surface coating except if non intended effects are considered. One possible effect is the formerly discussed effect of thin film change during sputter deposition of the “LiPON” solid electrolyte. The BTO coating at the surface might influence the effect the exposition to the sputter plasma has on the thin film and therefore change the thin film properties without a direct effect at the interface. If this was the case the same would be expected for the other coating materials.

The main effect that is theorized to be occurring during the sputter deposition is a change in lithium stoichiometry i.e. a lithium enrichment of the thin film leading to formation of unwanted phases. BTO could possible block this effect since the material itself does not contain lithium and is not a lithium ion conductor while both other coating materials are both containing lithium and are reasonable lithium ion conductors. Another possibility is that the solvent used to deposit the nanoparticles had an effect on the thin film properties since some kind of carrier solution was necessary to distribute the nanoparticles across the surface. The additional heat treatment at 100 ° C of the samples used to dry the organic solvent on the other hand is not likely to have an additional effect on the properties of the thin film.

The other process in the low frequency range inferred from the data around 1 Hz is once again rather similar for the modified and unmodified samples. The process changes to a diffusive behavior at the end of the discharge cycle (fig. 55 b)) as is also observed for the normally deposited sample via PLD. At the end of the discharge cycle this effect is nearly identical for all samples and therefore likely represents diffusion effects in the system that become dominant in the system once the cathode capacity is exhausted similar to the LTO system. The process is likely a summation of multiple diffusion processes.

13.4 Performance of spin coating films and comparison to PLD

Comparing the different data on all PLD deposited and even modified samples it is clear that the LNMO thin films produced this way have a multitude of problems preventing the production of a high quality, reversible battery system. Problems exist in regards to mechanical stability, phase composition and contact behavior of the system. Since the variation of deposition and production parameters for the PLD process could not eliminate these problems additionally spin coating of LNMO materials was employed to compare PLD thin films with a non vacuum based process more comparable to the powder preparation or electrode sheets prepared for liquid systems. For the preparation of these films a route published by Gellert *et al.*[54] was followed involving formation of the LNMO phase from a solution of the metal acetates described in the experimental section.

Cycling data for a spin coating LNMO thin film is depicted in fig. 56. As with the

PLD thin films the initial charge cycle exhibits signs of tetragonal/cubic phase transition indicating yet again the formation of the lithium enriched phase even though the thin film preparation method is very different from the previous samples. The capacity achieved by the system in the first cycle is close to the theoretical capacity estimated for this film which is 32 µAh/cm^2 (500 nm film thickness) so if complete film utilization is assumed the overall lithium stoichiometry is not above the expected range. Considering the cycling profile clearly shows the tetragonal phase transition only parts of the thin film might be active. The relative capacity achieved between different samples scales linear with the film thickness so effects causing low film utilization are not caused by conductive limitations or else thinner films would be expected to have higher relative film utilization.

As with previous samples in the first cycle a large part of the overall capacity achieved is irreversibly lost in the second cycle and the second and further cycles only show a small amount of Mn^{3+} oxidation with the nickel transitions clearly visible at higher potentials. This is the more generally expected behavior for the disordered spinel phase. The capacity loss between the first and second cycle is almost 2/3 most of which originating from the manganese transition while the nickel transition suffers a smaller loss in relative capacity. After the second cycle the capacity is relatively stable. The overall capacity achieved by the LNMO spin coating films is much higher when compared to the PLD thin films with similar thickness, especially the reversible capacity after the first cycle. By changing the deposition method better overall performance was achieved then was possible with the PLD deposited films irregardless of parameters employed or surface coatings tested. This begs the question on what the defining difference between both deposition methods is.

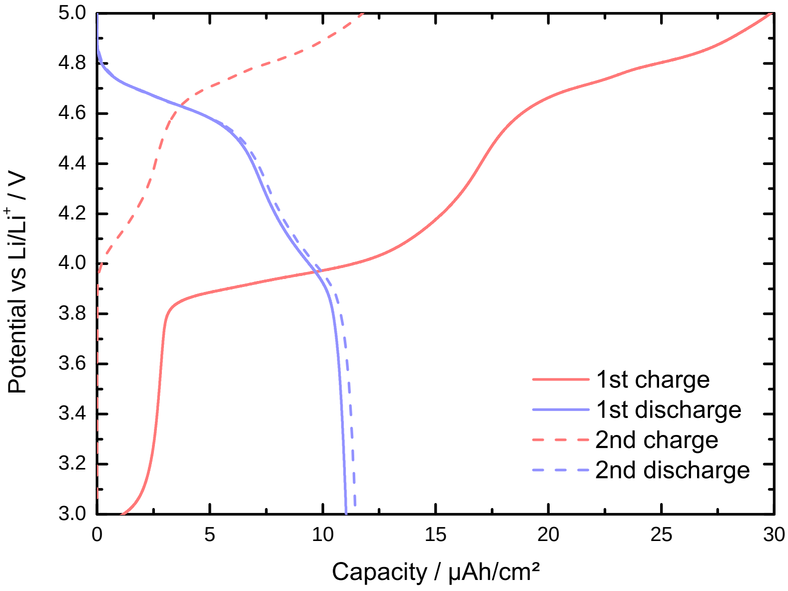

Figure 56: First and second cycle charge/discharge profile for a LNMO sample deposited via spin coating on a stainless steel substrate.

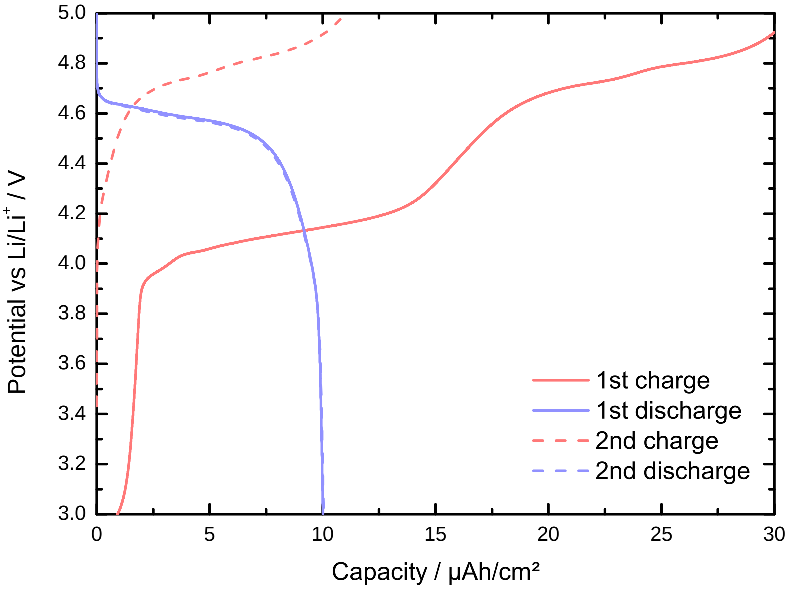

Figure 57: First and second cycle charge/discharge profile for a LNMO sample deposited via spin coating. An additional temperature relaxation step at 600 °C was introduced.

By changing the spin coating processing slightly it is possible to further modify the cycling behavior. Since the film shown in fig. 56 is prepared according to parameters described by Gellert *et al.* it is subjected to 700 °C for about 8 minutes before being rapidly cooled. This temperature is as described in the physical characterization close to the transition point between the disordered and ordered spinel phase and the rapid cooling aids in "quenching" the disordered phase once it forms leading to residual Mn^{3+} in the phase. By introducing an additional relaxation step at 600 °C for 4 hours and subsequent slow cooling of the sample the thin film is allowed to relax into the ordered spinel phase. This can be seen in fig. 57 in which a sample prepared identical to fig. 56 except for the additional temperature relaxation is shown. In the first cycle the two samples appear almost identical regarding the overall capacity and a similar charge distribution across the different cell processes is exhibited. In the first discharge however it becomes clear that for the reversible capacity the amount of active Mn^{3+} in the sample is significantly reduced. The different preparation conditions seemingly lead to the formation of the ordered spinel phase in which only nickel is active.

This conclusion is problematic though when considering the first cycle. As already described the cause for the large contribution of active manganese in the thin film is not entirely clear. If this is because the spinel phase is not correctly formed is it due to the preparation conditions itself or the further processing during the following steps? This result suggests that changing the preparation conditions has an influence on the cycling behavior of the cell so the problem is within the thin film preparation itself. The results also suggest that in the first cycle the preparation conditions do not matter since the behavior is the same. If it is assumed this is because the thin film is changed by the processing after the initial deposition this would explain why the first cycle is identical for both samples although their composition is seemingly changed. But this train of thought is also problematic because a change in the thin film composition by the introduction of additional lithium leading to formation of the tetragonal phase (indicate by the initial transition around 3.0 V) means that the final active phase is only formed in the cell after the lithium extraction in the initial cycle. If this is the case the preparation conditions should be irrelevant because the conditions in the cell under which the final phase is formed are identical. A alternative explanation is that the initial phase that is formed after the film deposition retains its cation ordering throughout the tetragonal/cubic phase transition since only the lithium content is changed and only lithium positions are affected by the phase change. This allows the originally prepared phase to show its behavior in the second cycle but still explains why the first cycle might be independent from the initial preparation conditions.

If the tetragonal phase forms and manganese therefore gets reduced to the Mn^{3+} state because of excess lithium the expected maximum composition is $Li_2Ni_{0.5}Mn_{1.5}O_4$[88] meaning that a maximum of 1/2 of the overall capacity could be ascribed to manganese oxidation due to excess lithium extraction. This is not considering that the expected voltage of extraction for compositions beyond about $Li_{1.4}$ is different than for compositions below that stoichiometry. The capacity displayed in the first cycle is not above the expected theoretical capacity. This explanation would only be feasible if the thin film utilization was lower than expected and only parts of the thin film were active during cycling and therefore the displayed capacity is above the theoretical value for the parts of the electrode that are active. It would still be expected that 1/2 of the initial charge capacity is reversible in the given voltage range. The reversible capacity measured is lower than that and it can also be seen that capacity is lost for the nickel transition too which should be unaffected by the effects describe above. This might be caused by film strain due to the phase transition of the material and subsequent additional loss of active electrode volume between the first and second cycle.

In theory the Mn^{3+} that is formed because of the additional lithium in the tetragonal phase is not equivalent to the Mn^{3+} in the disordered spinel phase. As Mancini *et al.*[88] showed the additional capacity introduced by the excess lithium is expected to be extracted at 3.0 V and not at 4.0 V as would be expected for the disordered spinel phase. Yet in the samples shown in this thesis the lithium extraction mainly proceeds at 4.0 V weakening the previously described argument that they result from a lithium enriched tetragonal phase. It is possible that the lithium extraction occurs with a significant overvoltage and therefore only appears in the given voltage range but 1 V of overvoltage is an exceedingly large value. This returns the train of thought back to the beginning and the question why is this transition irreversible if it is possibly not connected to the tetragonal phase? Somewhere along the line there is a piece missing in the argument. Recent literature by Li *et al.*[51] have demonstrated a highly functional battery of the same type as shown here but they also show the same first cycle anomaly as is depicted here. The authors used the same argument of excess lithium in the first cycle to explain their findings but the same argumentative problem applies to their results as well. If the processing conditions after the initial film deposition prove to be an important factor in the electrochemical behavior of the electrode material this could have severe implications for the LNMO all-solid-state system in general.

In liquid cells additional capacity loss in the first cycle is often also attributed to minor side reactions in the system and the formation of a SEI degradation layer. In solid state cells the phenomenon is not yet clearly explored. From the LTO cell data and works in the literature regarding the “LiPON” stability[28] it is known that “LiPON” degrades in contact with lithium, forming a SEI layer but for the cathode materials this phenomenon is not often discussed. The amount of charge lost in the first cycle is also quite high to be explained purely in this manner. Since this phenomenon is not directly explained by the considerations offered so far and is clearly limited to the first charge only, it is possible that the formation of a cathode/electrolyte SEI in the solid/solid phase is observed here. This degradation is possibly “activated” through the increased cell potential since the cell is assembled in a discharged state with possibly small amounts of tetragonal phase present (small voltage plateau at 3.0 V) so some excess lithium is indeed introduced into the system. This was also already observed in the LTO system. Once the cell potential is increased during the first charging step the electrochemical stability region of the electrolyte is surpassed and the degradation sets in. This could also explain why the position of this plateau is seemingly randomly different for the samples shown here and in one case is slightly above and in the other slightly below 4.0 V. The similarity to the voltage position of the manganese transition in this case could be purely coincidental. In any case the simple explanation given in the literature that the irreversible capacity in the first cycle is caused by lithium enrichment seems inconsistent.

13.5 A perspective on the impedance analysis of the LNMO system

Analysis regarding the impedance behavior of the LNMO solid state state cells is hampered by inconsistencies in the impedance data for seemingly identical cells. In order to draw significant conclusions from the impedance spectrum the underlying processes have to be understood in order to interpret the spectrum correctly. In the case of the LTO

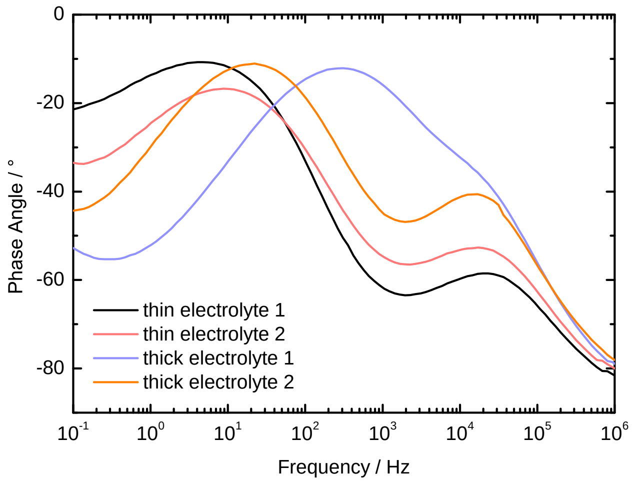

Figure 58: Phase angle of LNMO cells produced through spin coating. In this case 5 layers of LNMO were deposited on stainless steel and coated with either a "thin" electrolyte layer (5 hour deposition about 1.5 μm) or a "thick" layer (9 hour deposition approx. 2.75 μm). Two samples are given for each system.

system this was done by changing parts of the cell setup and interpreting the differences observed in the impedance spectrum. Initially this process can be difficult if the processes involved are unknown since changing a specific property of the cell design might not have the expected consequences and effects might either not be visible or counter intuitive. Unknowingly other properties of the cell not previously considered but important for the impedance spectrum might have been changed causing a difference in the observed data. This basic principle of empiric sciences can only be circumvented by constant comparison to a stable comparison state. The problem for the LNMO solid state cells in this thesis is that such a stable comparison state could never be reached because cells produced in an identical manner would exhibit differences in their impedance data that are not yet conclusively understood. Of course a margin of variance exists in the measurement even of identical cells that is typically alleviated through measurement of a large number of samples and evaluating the statistical distribution of results. This is in this case not easily possible since a) the cell production methods are somewhat complicated allowing only a relatively small amount of cells to be produced and b) in case of the LNMO system due to various engineering problems already discussed a high percentage of these cells were not functional to the point of allowing reasonable measurements.

An example of this problem is depicted in fig. 58. In this case two examples of identical cells are given with either a "thin" electrolyte coating of 1.5 μm or a "thick" coating of 2.75 μm. All four samples were otherwise produced via spin coating on stainless steel substrates with a LNMO thickness of 5 layers or approx 250 nm. The expected change in impedance data between these samples is that the resistance in the high frequency region should increase since it is attributed to the solid electrolyte. This can be observed when fitting the data though it is not readily apparent in the data as displayed. More importantly this is the only change that is expected in the impedance since all other processes expected and discussed so far are not dependent on the electrolyte thickness. It is obvious though that especially in the middle frequency region large differences between the samples exist. For the “thin” samples 1 and 2 this is still possibly explained by variance while for the “thick” sample 1 this region is clearly different even though it should be identical to “thick” sample 2 and even both “thin” samples. If the previously made assumption that electronic charge transfer resistances between the substrate and the LNMO film are visible in this region are still valid then this can possibly be explained. Since this charge transfer resistance is sensitive to the contact interface between the metal and the thin film it is possible that variations in temperature or different surface conditions while applying the LNMO film have an effect causing the differences in observed behavior.

Probing this behavior by employing changes to the surface of the stainless steel substrate (i.e. platinum and gold coating) should allow to further investigate the effect but the differences observed in these measurements were either not clear enough due to the variations already present in unmodified samples or problematic due to problems with film adhesion (in the case of gold coating). The lack of solid data in this frequency range also complicates the analysis of the difference between thin films prepared by PLD, surface modified PLD and spin coating. As has been shown the spin coating films offer vastly improved performance and cell activity but the underlying reason is not understood. The experimental data for coating layers on PLD thin films suggested that a change in the impedance is achieved in the middle frequency region by introducing surface coatings which suggests that other processes than the substrate/thin film contact are important in this region as well. As with all impedance measurements processes can only really be studied if they are significantly dominant in their respective frequency region or if the exact number and relation of all processes in a frequency range to each other is already known. Otherwise the impedance spectrum observed can be fitted with any number of equivalent circuits rendering the interpretation of the spectrum rather speculative. For LTO this problem could be circumvented by iterative testing and elimination of many theoretically possibilities regarding the nature of underlying processes but for LNMO the changes in the data resulting from the change in setup are not entirely consistent.

With the high frequency region of the impedance data acting as expected, representing the solid electrolyte, and the middle frequency region remaining questionable due to the involvement of too many currently unknown effects this leaves the low frequency range to be discussed. In the case of LTO it was concluded that this region depicts the ionic

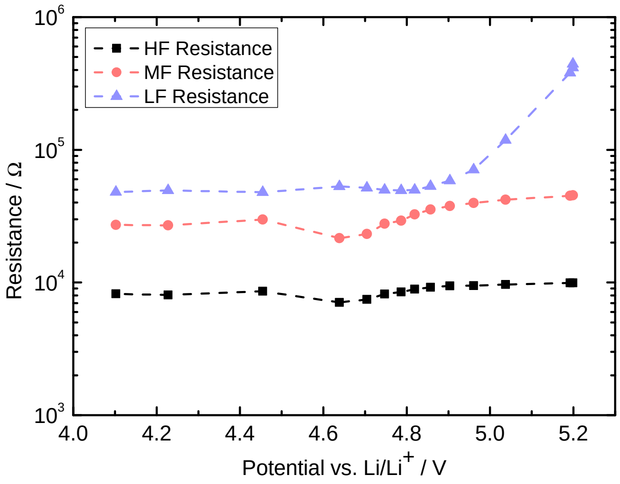

Figure 59: Fitted resistance values for the impedance data of an LNMO all-solid-state cells during the charge half cycle. Resistances depicted are for the high frequency process HF, middle frequency process MF and low frequency process LF.

transport through the thin film since its properties were directly related to the state of charge and to the two phase nature of the material discussed. Significant changes in the transport properties of LTO were expected during cycling and were represented in the impedance data. For LNMO changes as drastic as previously observed are not expected.

Fig. 59 depicts the resistance values that can be extracted for a LNMO cycling profile for a model assuming 3 different process (i.e. R/CPE elements) in the high, medium and low frequency region. The high frequency resistance corresponds to the solid electrolyte as with LTO and exhibits about the same values and behavior as seen for the LTO samples. It does not change significantly with the state of charge or cell potential of the cell. The not clearly defined process in the medium frequency range also is not influenced much by the state of charge with only a slight dip in resistance being observed around the lithium insertion/extraction potential. The low frequency process that showed rather clear dependence on the state of charge for the LTO samples is also not strongly dependent on the SOC in this case except for potentials in excess of 5.0 V. This abrupt change in behavior towards the end of the charge cycle is more likely directly related to a switch in cell conditions once the lithium extraction is finished. The electrode changes to blocking behavior since lithium can no longer be extracted which changes the nature of the process observed in this region . This has already been described for the LTO system and is also similar in the discharge cycle.

The fact that this process is not linear dependent on the SOC is no helpful criteria in determining if the bulk thin film properties or the interface properties are observed in this case. To exclude the possibility of the bulk thin film being measured, experiments with varying thin film thicknesses can be performed as was done with the LTO system. For the LNMO system this measurement is problematic due to the unclear nature of the variance in the medium frequency range. Referring back to fig. 58 it is obvious that the low frequency range of the impedance is influenced by the middle frequency region. The magnitude of the observed resistance is different in all cases and the overlap between the low and medium frequency processes is directly dependent on the magnitude of the medium frequency process. This is a problem because for the comparison of film thickness effects absolute values of the resistance have to be compared i.e. is the resistance twice as high for twice the thickness?

If the resistance gets influenced by unknown effects in the middle frequency region that are, under the currently known circumstances, seemingly random such a comparison is not possible not only because the logical relations between processes is unclear but also because the fitting algorithm employed can easily result in varying results if not controlled tightly by the user. The data measured in these samples was inconclusive since no clear dependence of the low frequency process with film thickness could be determined. This suggests that the process is not related to the thin film bulk properties and instead related to a interface resistance but as described this result is not conclusive. Assumptions on the behavior can be made from the data but not reliably proven due to too many unknown influences in the impedance. Because of the engineering problems in the cell setup used and the limitation those problems put on the choice of substrate and sample handling it is unlikely that the cell and processing design as it was used in this thesis is able to facilitate all necessary changes to the system that have to be made in order to determine the nature of the underlying process. In order to explore these question a redesign of the entire cell setup and possibly of the utilized deposition method (i.e. change to sputter deposition) is likely necessary. This in turn would make direct comparisons to the LTO system studied in this thesis questionable depending on what specifics of the setup (specifically cell constant and overall proportion of cell geometry) were to be changed. The design rework would therefore extend beyond the scope of this thesis.

Returning to the discussion of the impedance for the data that was measured, it is interesting to note that the changes observed in the impedance for different cells while significant in the impedance spectrum seemingly had no massive consequences for the cycling performance of the cells. The cycling data of all cells depicted in fig. 58 is comparable even though overall resistance values measured tend to vary sometimes an order of magnitude. This change in the resistance has only minor influence on the overvoltage. Fig. 60 depicts the discharge profile in the second cycle specifically for both examples in fig. 58 that exhibited the largest difference in impedance even though they were prepared identically.

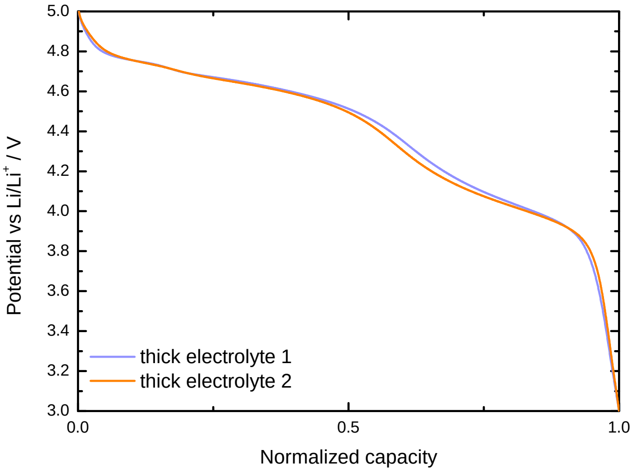

Figure 60: Discharge profile of two identically prepared samples with normalized capacity as comparison to the impedance data in fig. 58.

The discharge profiles for both samples appear nearly identical with apparently only a slight difference in the proportions of the Ni/Mn ordering. The capacity is normalized to easier compare states of charge directly since the absolute capacity was different but in a way that is likely not related to the impedance phenomenon (i.e. the cell with overall higher resistance had slightly higher capacity). It is apparent that the differences in overall profile shape and exhibited overvoltage are negligible between both samples. The large difference in resistance observed between these samples in the medium frequency range therefore might have no impact on the actual cell kinetic. This can be because the difference in resistance measured is small compared to the low frequency resistance that often is not fully depicted due to the measurement times involved in measuring extremely low frequencies (and the problems arising due to the change in battery state at low frequencies). From the data that is available in the measured frequency range this does not seem to be the case though and resistances in both regions are around the same order of magnitude.

Another possibility is that the observed resistance appears only in the impedance measurement and is not part of the active cell resistance during cycling. This explanation is only valid if the cell characteristics change between the potentiostatic condition of the impedance measurement and the dynamic condition during active charge and discharge. If the cell conditions are not different the DC resistance must be a summation of all resistances measured in the impedance. For LTO this might be possible because of the relaxation of the phase composition into a solid solution depending on the kinetic conditions but for LNMO there is no readily apparent explanation why both kinetic states should be vastly different regarding their resistive behavior.

13.6 Lithium dendrite growth in the solid electrolyte

Aside from direct cell failure due to film delamination and shortcircuiting another observed effect was the gradual cell failure of cells apparent within the first one to two cycles. In those cases the cycling proceeded normally with the cell entering the expected charge plateaus in the cycle but subsequently proceeded to show a decline in cell voltage despite a positive charge current being applied. Fig. 61 depicts the charge profile of such a cell. The initial cell potential is similar to previously shown cells at around 3.0 V and in the first few minutes of charge the cell reaches the 4.0 V plateau. The plateau itself shows and unstable voltage behavior and exhibits multiple small drops in voltage. After about 0.5 h the voltage in the system starts to drop with further cycling time while the same positive current of 35 µA/cm^2 is applied. This can only mean that an internal shortcircuit has occurred that now discharges the cell internally with a discharge current greater than 35 µA/cm^2. The following cell discharge exhibits voltage plateaus that are as shown by Mancini *et al.*[88] typical for further lithium insertion into the spinel. The exact potential position of these plateaus in this specific case is difficult to discuss because the net discharge current that arises from the internal short circuit is unknown and therefore the expected overpotential cannot be judged.

While an internal short circuit in this type of cell can have multiple reason further data strongly suggests that the reason is mots likely lithium dendrite growth in the solid electrolyte. The short circuit does not exist at the start of the cell life and only develops once cell cycling begins. This allows the exclusion of most explanations based on inherent cell defects or mechanical damages to the cell. Furthermore the value of the net discharge

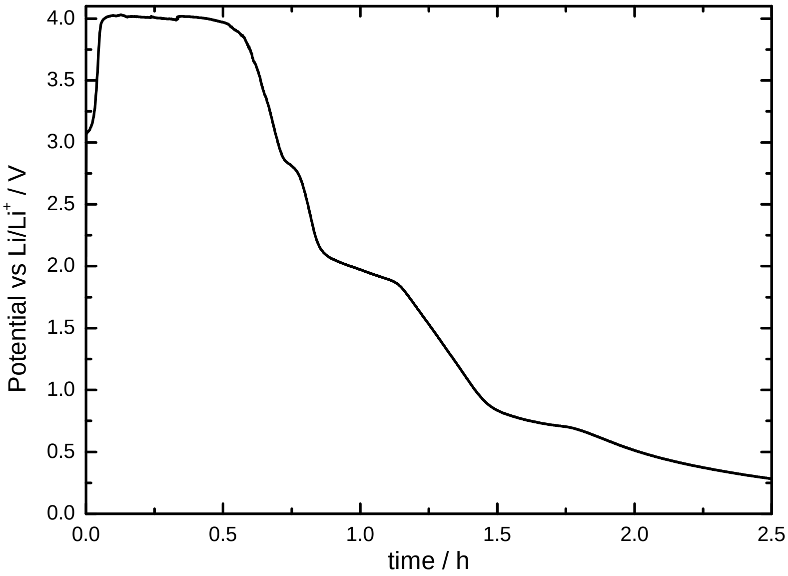

Figure 61: Voltage profile versus time for a failed LNMO solid state cell cycled at 35 µA/cm^2.

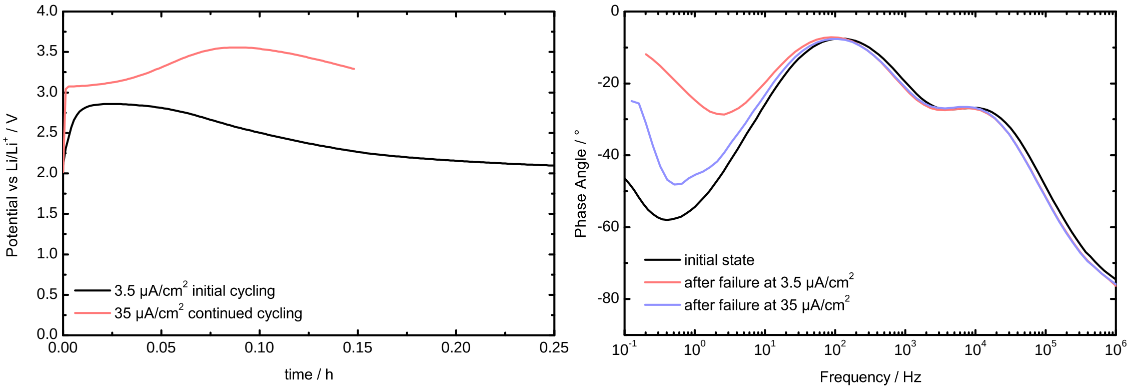

Figure 62: Voltage profile of a LNMO failed solid state cell with two different charge currents as well as the phase angle of the impedance for the initial cell state and states after cell failure at each applied charge current.

current rises with prolonged cell life, meaning the resistance of the short circuit drops. In fig. 61 this is identifiable because before the cell voltage actually drops there are already signs of instability inside the cell system due to the unstable voltage plateau. The net discharge current in this region is still smaller than the applied charge current causing the cell to still exhibit positive current flow. This can further be exemplified by fig. 62. Here the voltage profile is depicted for two different charge currents. The initial charge current of 3.5 µA/cm^2 was applied until cell failure was observed (drop in voltage). Afterward the charge current was raised to 35 µA/cm^2 and a second voltage profile was measured. As can be seen for the higher current the previously failed cell again starts to charge and address the expected voltage plateaus. Only after further cycling does the cell fail again because the net discharge current now also exceeds the newly applied current. Also depicted in the figure is the phase angle of the impedance for measurements of the initial cell (before cycling), the cell after the failure at low current and after the failure at high current. Immediately apparent is that at no point does the cell exhibit signs of complete cell short circuit. For a complete cell failure it would be expected that only a small ohmic resistance is measured. This is often the case if mechanical short circuits occur for example due to film delamination. Instead the impedance data is largely identical for the three compared states. The main difference exhibited is expressed in the resistance of the low frequency process. This change is difficult to interpret because the nature of the process is unknown. It could simply be related to the changing state of charge due to the lithium insertion into the system or could be an effect of the dropping cell potential and the corresponding reduction in length for space charge layers at the cathode interface. The voltage range observed in these measurements is outside of the voltage range typically measured for functioning cells.

The fact that the short circuit does not appear as ohmic resistance and seemingly has little effect on the overall impedance state of the cell can have two reasons. One reason is that the formed dendrites still have a comparatively low net charge transport, meaning their resistance is quite high. In this case since they essentially offer a parallel charge transport path to the expected battery processes they are not visible in the impedance because only the path of least resistance is measured. Another possible explanation is that dendrites are destroyed during the impedance measurement since the potentials applied might cause high current flow through the dendrite, especially at high frequencies, leading to he destruction of the dendrite. Judging the current flow through the dendrite during the impedance measurement is difficult. In the high frequency region currents measured in the high frequency range are in the region of several µA/cm^2 but these currents are partly capacitive. It seems unlikely that these currents are high enough to destroy the formed dendrites. In any case the observed phenomenon of gradual cell failure can only be explained by dendrite formation. This is somewhat surprising since the suppression of dendrite formation was always a strong argument for the use of solid electrolytes.

In this case dendrites were only observed for the LNMO system and not for the LTO system in the measured timespan which can possibly be explained by the LNMO samples being deposited on polished stainless steel substrates. These substrates exhibit a significantly rougher surface due to the limitations of the polishing setup and also some macroscopic defects. The local electric fields can therefore be higher further facilitating dendritic growth in the measured timespan. Furthermore, interface defects arising from this roughness are assumed to be a significant factor in lithium dendrite formation.[136] The higher cell potential of the LNMO cells is expected to produce a higher voltage drop at the interface between LNMO and the electrolyte, but not necessarily across the solid electrolyte or at the lithium/electrolyte interface.

14 Conclusion

In this thesis two functioning model-type systems of all-solid-state batteries have been prepared. The LTO/“LiPON”/Li system as well as the LNMO/“LiPON”/Li system provide rather different challenges for preparation and analysis of battery cells.
The LTO system can be easily fabricated and shows consistent and stable battery behavior under most circumstances. The analysis of the system through impedance spectroscopy is rather complicated due to multiple details that comprise the impedance spectrum of the system. A large part of the overall battery behavior in this case can be attributed to the two-phase nature of the material and the large difference in material properties of these two phases as well as to the mechanics of phase transition. During the thesis data suggesting a solid solution phase transition has been found based on the change of resistive behavior and activation energies of the electrode materials during cycling. The resistive and capacitive behavior of the thin film could be explained at all states of charge using this solid solution phase transition mechanism. Additionally, processes formerly considered less important have been revealed to play a significant role in the cell behavior. The electronic contact properties of the LTO phase were shown to be limiting in contact to poor electronic conductors or semiconductors as well as for very thin LTO layers. It was shown that the contact properties are still relevant even in contact to metallic conductors but are not easily visible in that case. The contact phenomena were discussed in regard to the band distortion and space charge layer formation at the interface.

For the “LiPON” solid electrolyte the formation of a degradation phase in direct contact with lithium has been shown through impedance spectroscopy verifying results obtained in the literature by XPS.[28] The interphase formed has been shown to be less conductive than the solid electrolyte and considering the conductivity difference should be relevant in the impedance data for electrolyte thicknesses up to approx. 10 µm, which is the common range of thickness for “LiPON” in solid-state cells. The existence of this degradation phase is rarely discussed in literature published before the start of this thesis and commonly does not appear in the discussion of impedance data. Processing steps and general workflow that is necessary to characterize an unknown system through impedance spectroscopy were given in detail in order to showcase the problems that can occur with this method if erroneous assumptions are made and not verified.

For the LNMO thin film system the fabricated solid state cells were much less consistent and stable. Main problems of the LNMO battery preparation have been connected with the material and mechanical properties of the LNMO phase during deposition and further processing. The general behavior of the systems seems to be mainly governed by a) the phase composition of the material and subsequently the amount of Mn^{3+} in the phase and b) the preparation method of the thin film. Clear differences in electrochemical behavior have been shown between the preparation via PLD or post annealed PLD and spin coating with the spin coated films generally performing better. The charge transfer resistance often described in the literature to be limiting has been modified by various coatings but beneficial results were always overshadowed by the much better performance of the spin coated thin films. Furthermore, first cycle anomalies in the cycling profiles suggest either a lithium enrichment of the material which might possibly occur due to “LiPON” deposition or the formation of a cathode SEI layer similar to the “LiPON” degradation already mentioned.

A more detailed evaluation of the impedance data for LNMO cells was hindered by the poor mechanical stability of the thin films on most substrates and the tendency of lithium dendrite formation on stainless steel substrates which are also rarely discussed in the literature for solid electrolytes due to the assumption that the solid phase suppresses dendrite growth which is still often assumed despite being shown in the past to be incorrect. For thin films this issue has probably been avoided in the past due to the smooth surfaces and reduced interface defects facilitating less dendrite nucleation and growth.

15 Outlook

For the LTO system the proposed model of phase transition and equivalent circuit largely explains the measured data and behavior. Still, the mechanism of phase change and the specifics of the formed domains remain unproven. As already mentioned in the text high resolution synchrotron measurements of active battery cells could aid in discerning between the rock salt, spinel and solid solution LTO phases. The requirement for this would be an *in situ* battery setup in a synchrotron environment. Neutron diffraction is likely impossible to perform on such a system since the active phase is buried beneath other cell components and other techniques to produce samples (like FIB cuts) would not produce enough measurable material. Due to the optical properties of the LTO material the phase change might also be accessible with optical measurements granted an equally specific setup would be required to observe the parameter change in a thin film. The data collected so far reinforce the trend already observed in the literature that LTO and “LiPON” have only minor charge transfer resistances. The data also shows that the internal resistance of LTO is a major contributor to the overall resistance of solid state cells, especially towards the fully discharged state. For thin film batteries especially since it is difficult to introduce conductive agents, this can be a major flaw of the material in practical application. Since part of the limitation is also caused by low ionic conductivity introducing conductive aids is not only difficult but impossible. If the material is to be used in practice these problems will have to be overcome by cell design and for example 3D architecture or cell stacking which in turn could cause other interface processes described in this thesis to become problematic.

Considering the results of the impedance analysis shown in this thesis it is clear that solid state systems can introduce a lot of problems that are typically less important or not discussed for liquid systems. The detailed description of microscopic steps in the solid state system is therefore mandatory in understanding cell behavior and improving cell limitations. This is especially true when discussing the second material targeted in this thesis, the LNMO cathode. For this material improvement of cell behavior has been shown empirically due to the way the thin film is produced. Favorable effects of coatings have been shown for PLD thin films but the fact that these effects are overshadowed by effects of the deposition method, as shown here and in the work of Li *et al.*,[51] clearly show that the underlying effects of these empirically observed trends is not yet understood. For LNMO a redesign of the existing cell system and setup is necessary since the material properties are not well suited to produce stable and reliable systems under the current constraints. To better compare the impact of deposition methods other possible methods like sputter deposition (magnetron or ion beam) or atomic layer depositions will have to be compared in an equivalent setup that allows the separation of specific cell processes and hopefully the monitoring of these processes in dependence of different changes to the cell. Impedance spectroscopy will be an important tool for this in the future.

In terms of viability of the material in all-solid-state batteries it is still not clear what the limitations of the material in certain setups are. This thesis and the work of Li *et al.* suggest that the interface with “LiPON” might be less of an issue as expected if the system is prepared carefully, but this only means that the limitations that exist in the work of others are not sufficiently understood. The work of Li *et al.* shows that it is possible to produce cells with long term stable cycling yet even in their work questions regarding the phase composition of the material as well as first cycle anomalies remain. This is in direct contrast to the LTO material that at this point is rather well understood and the limitations it provides can be circumvented by purposeful cell design and setup. LNMO has yet to reach this point and currently relies mostly on empirical research which produces the large differences in observed behavior as exemplified by Li *et al.*[51] as well as Yada *et al.*[40] that are present in the literature today. This thesis serves to focus the attention to formerly rarely discussed effects specific to solid state systems and opens up several perspectives on previously more narrowly discussed problems.

16 References

[1] J. G. Kim, B. Son, S. Mukherjee, N. Schuppert, A. Bates, O. Kwon, M. J. Choi, H. Y. Chung, S. Park, A review of lithium and non-lithium based solid state batteries, Journal of Power Sources 282 (2015) 299–322.

[2] L. Chen, L. L. Shaw, Recent advances in lithium–sulfur batteries, Journal of Power Sources 267 (2014) 770–783.

[3] J. Bates, N. Dudney, G. Gruzalski, R. Zuhr, A. Choudhury, C. Luck, J. Robertson, Electrical properties of amorphous lithium electrolyte thin films, Solid State Ionics 53–56, Part 1 (1992) 647–654.

[4] M. M. Thackeray, ZA, J. B. Goodenough, GB2, United States Patent: 4507371 - Solid state cell wherein an anode, solid electrolyte and cathode each comprise a cubic-close-packed framework structure (Mar. 1985).

[5] J. M. Tarascon, E. Wang, F. K. Shokoohi, W. R. McKinnon, S. Colson, The Spinel Phase of $LiMn_2O_4$ as a Cathode in Secondary Lithium Cells, Journal of The Electrochemical Society 138 (10) (1991) 2859–2864.

[6] T. Ohzuku, A. Ueda, N. Yamamoto, Zero-Strain Insertion Material of Li [Li1/3Ti5/3]O4 for Rechargeable Lithium Cells, Journal of The Electrochemical Society 142 (5) (1995) 1431–1435.

[7] T. Ohzuku, M. Kitagawa, T. Hirai, Electrochemistry of Manganese Dioxide in Lithium Nonaqueous Cell III . X-Ray Diffractional Study on the Reduction of Spinel-Related Manganese Dioxide, Journal of The Electrochemical Society 137 (3) (1990) 769–775.

[8] E. Ferg, R. J. Gummow, A. d. Kock, M. M. Thackeray, Spinel Anodes for Lithium-Ion Batteries, Journal of The Electrochemical Society 141 (11) (1994) L147–L150.

[9] A. Deschanvres, B. Raveau, Z. Sekkal, Mise en evidence et etude cristallographique d'une nouvelle solution solide de type spinelle $Li_{1+x}Ti_{2-x}O_4$ $0 < x < 0{,}333$, Materials Research Bulletin 6 (8) (1971) 699–704.

[10] D. C. Johnston, Superconducting and normal state properties of $Li_{1+x}Ti_{2-x}O_4$ spinel compounds. I. Preparation, crystallography, superconducting properties, electrical resistivity, dielectric behavior, and magnetic susceptibility, Journal of Low Temperature Physics 25 (1-2) (1976) 145–175.

[11] K. M. Colbow, J. R. Dahn, R. R. Haering, Structure and electrochemistry of the spinel oxides $LiTi_2O_4$ and $Li_{43}Ti_{53}O_4$, Journal of Power Sources 26 (3) (1989) 397–402.

[12] S. Scharner, W. Weppner, P. Schmid-Beurmann, Evidence of Two-Phase Formation upon Lithium Insertion into the $Li_{1.33}Ti_{1.67}O_4$ Spinel, Journal of The Electrochemical Society 146 (3) (1999) 857–861.

[13] M. Wagemaker, D. R. Simon, E. M. Kelder, J. Schoonman, C. Ringpfeil, U. Haake, D. Lützenkirchen-Hecht, R. Frahm, F. M. Mulder, A Kinetic Two-Phase and Equilibrium Solid Solution in Spinel $Li_{4+x}Ti_5O_{12}$, Advanced Materials 18 (23) (2006) 3169–3173.

[14] M. Wagemaker, E. R. H. van Eck, A. P. M. Kentgens, F. M. Mulder, Li-Ion Diffusion in the Equilibrium Nanomorphology of Spinel $Li_{4+x}Ti_5O_{12}$, The Journal of Physical Chemistry B 113 (1) (2009) 224–230.

[15] D. Li, P. He, H. Li, H. Zhou, An unsymmetrical lithium-ion pathway between charge and discharge processes in a two-phase stage of $Li_4Ti_5O_{12}$, Physical Chemistry Chemical Physics 14 (25) (2012) 9086–9091.

[16] D. J. Crain, J. P. Zheng, D. Roy, Electrochemical examination of core–shell mediated Li+ transport in $Li_4Ti_5O_{12}$ anodes of lithium ion batteries, Solid State Ionics 240 (2013) 10–18.

[17] Y.-R. Zhu, L.-C. Yin, T.-F. Yi, H. Liu, Y. Xie, R.-S. Zhu, Electrochemical performance and lithium-ion intercalation kinetics of submicron-sized $Li_4Ti_5O_{12}$ anode material, Journal of Alloys and Compounds 547 (2013) 107–112.

[18] N. Takami, K. Hoshina, H. Inagaki, Lithium Diffusion in $Li_{4/3}Ti_{5/3}O_4$ Particles during Insertion and Extraction, Journal of The Electrochemical Society 158 (6) (2011) A725–A730.

[19] Y. H. Rho, K. Kanamura, Li+ ion diffusion in $Li_4Ti_5O_{12}$ thin film electrode prepared by PVP sol–gel method, Journal of Solid State Chemistry 177 (6) (2004) 2094–2100.

[20] F. Wunde, F. Berkemeier, G. Schmitz, Lithium diffusion in sputter-deposited $Li_4Ti_5O_{12}$ thin films, Journal of Power Sources 215 (2012) 109–115.

[21] Y. Iriyama, D. Shimizu, T. Abe, M. Sodoh, Z. Ogumi, Fast and Stable Charge Transfer Reaction at the $Li_{4/3}Ti_{5/3}O_4$/Lithium Phosphorus Oxynitride (LIPON) Interface and its Application to All-Solid-State Thin Film Batteries, ECS Transactions 16 (26) (2009) 45–52.

[22] H. Nakazawa, K. Sano, M. Baba, N. Kumagai, Stability of Thin-Film Lithium-Ion Rechargeable Batteries Fabricated by Sputtering Method without Heating, Journal of The Electrochemical Society 162 (3) (2015) A392–A397.

[23] J. Ma, C. Wang, S. Wroblewski, Kinetic characteristics of mixed conductive electrodes for lithium ion batteries, Journal of Power Sources 164 (2) (2007) 849–856.

[24] J. Deng, Z. Lu, I. Belharouak, K. Amine, C. Chung, Preparation and electrochemical properties of $Li_4Ti_5O_{12}$ thin film electrodes by pulsed laser deposition, Journal of Power Sources 193 (2) (2009) 816–821.

[25] J. Deng, Z. Lu, C. Y. Chung, X. Han, Z. Wang, H. Zhou, Electrochemical performance and kinetic behavior of lithium ion in $Li_4Ti_5O_{12}$ thin film electrodes, Applied Surface Science 314 (2014) 936–941.

[26] S. Larfaillou, D. Guy-Bouyssou, F. le Cras, S. Franger, Comprehensive characterization of all-solid-state thin films commercial microbatteries by Electrochemical Impedance Spectroscopy, Journal of Power Sources 319 (2016) 139–146.

[27] X. Yu, J. B. Bates, G. E. Jellison, F. X. Hart, A Stable Thin-Film Lithium Electrolyte: Lithium Phosphorus Oxynitride, Journal of The Electrochemical Society 144 (2) (1997) 524–532.

[28] A. Schwöbel, R. Hausbrand, W. Jaegermann, Interface reactions between LiPON and lithium studied by in-situ X-ray photoemission, Solid State Ionics 273 (2015) 51–54.

[29] A. Schwöbel, W. Jaegermann, R. Hausbrand, Interfacial energy level alignment and energy level diagrams for all-solid Li-ion cells: Impact of Li-ion transfer and double layer formation, Solid State Ionics 288 (2016) 224–228.

[30] S. Sicolo, K. Albe, First-principles calculations on structure and properties of amorphous $Li_5P_4O_8N_3$ (LiPON), Journal of Power Sources 331 (2016) 382–390.

[31] S. Sicolo, M. Fingerle, R. Hausbrand, K. Albe, Interfacial instability of amorphous LiPON against lithium: A combined Density Functional Theory and spectroscopic study, Journal of Power Sources 354 (2017) 124–133.

[32] Y. Iriyama, T. Kako, C. Yada, T. Abe, Z. Ogumi, Charge transfer reaction at the lithium phosphorus oxynitride glass electrolyte/lithium cobalt oxide thin film interface, Solid State Ionics 176 (31–34) (2005) 2371–2376.

[33] F. Sagane, K.-i. Ikeda, K. Okita, H. Sano, H. Sakaebe, Y. Iriyama, Effects of current densities on the lithium plating morphology at a lithium phosphorus oxynitride glass electrolyte/copper thin film interface, Journal of Power Sources 233 (2013) 34–42.

[34] Y. Iriyama, K. Nishimoto, C. Yada, T. Abe, Z. Ogumi, K. Kikuchi, Charge-Transfer Reaction at the Lithium Phosphorus Oxynitride Glass Electrolyte/Lithium Man-

ganese Oxide Thin-Film Interface and Its Stability on Cycling, Journal of The Electrochemical Society 153 (5) (2006) A821–A825.

[35] W. C. West, Z. D. Hood, S. P. Adhikari, C. Liang, A. Lachgar, M. Motoyama, Y. Iriyama, Reduction of charge-transfer resistance at the solid electrolyte – electrode interface by pulsed laser deposition of films from a crystalline Li_2PO_2N source, Journal of Power Sources 312 (2016) 116–122.

[36] A. Eftekhari, Fabrication of 5 V lithium rechargeable micro-battery, Journal of Power Sources 132 (1–2) (2004) 240–243.

[37] M. Gellert, K. I. Gries, J. Zakel, S. Kranz, S. Bradler, E. Hornberger, S. Müller, C. Yada, F. Rosciano, K. Volz, B. Roling, Charge Transfer across the Interface between $LiNi_{0.5}Mn_{1.5}O_4$ High-Voltage Cathode Films and Solid Electrolyte Films, Journal of The Electrochemical Society 162 (4) (2015) A754–A759.

[38] D. Santhanagopalan, D. Qian, T. McGilvray, Z. Wang, F. Wang, F. Camino, J. Graetz, N. Dudney, Y. S. Meng, Interface Limited Lithium Transport in Solid-State Batteries, The Journal of Physical Chemistry Letters (2013) 298–303.

[39] S. Braun, C. Yada, A. Latz, Thermodynamically Consistent Model for Space-Charge-Layer Formation in a Solid Electrolyte, The Journal of Physical Chemistry C 119 (39) (2015) 22281–22288.

[40] C. Yada, A. Ohmori, K. Ide, H. Yamasaki, T. Kato, T. Saito, F. Sagane, Y. Iriyama, Dielectric Modification of 5V-Class Cathodes for High-Voltage All-Solid-State Lithium Batteries, Advanced Energy Materials 4 (9) (2014) 1614–6840.

[41] K. Yamamoto, Y. Iriyama, T. Asaka, T. Hirayama, H. Fujita, C. A. J. Fisher, K. Nonaka, Y. Sugita, Z. Ogumi, Dynamic Visualization of the Electric Potential in an All-Solid-State Rechargeable Lithium Battery, Angewandte Chemie International Edition 49 (26) (2010) 4414–4417.

[42] K. Yamamoto, Y. Iriyama, T. Asaka, T. Hirayama, H. Fujita, K. Nonaka, K. Miyahara, Y. Sugita, Z. Ogumi, Direct observation of lithium-ion movement around an in-situ-formed-negative-electrode/solid-state-electrolyte interface during initial charge–discharge reaction, Electrochemistry Communications 20 (2012) 113–116.

[43] M. Landstorfer, S. Funken, T. Jacob, An advanced model framework for solid electrolyte intercalation batteries, Physical Chemistry Chemical Physics 13 (28) (2011) 12817–12825.

[44] J. Bates, N. Dudney, B. Neudecker, A. Ueda, C. Evans, Thin-film lithium and lithium-ion batteries, Solid State Ionics 135 (1–4) (2000) 33–45.

[45] R. J. Gummow, A. de Kock, M. M. Thackeray, Improved capacity retention in rechargeable 4 V lithium/lithium-manganese oxide (spinel) cells, Solid State Ionics 69 (1) (1994) 59–67.

[46] T. Eriksson, A. M. Andersson, A. G. Bishop, C. Gejke, T. Gustafsson, J. O. Thomas, Surface Analysis of $LiMn_2O_4$ Electrodes in Carbonate-Based Electrolytes, Journal of The Electrochemical Society 149 (1) (2002) A69–A78.

[47] J. C. Hunter, Preparation of a new crystal form of manganese dioxide: λ-MnO_2, Journal of Solid State Chemistry 39 (2) (1981) 142–147.

[48] J. Vetter, P. Novák, M. R. Wagner, C. Veit, K. C. Möller, J. O. Besenhard, M. Winter, M. Wohlfahrt-Mehrens, C. Vogler, A. Hammouche, Ageing mechanisms in lithium-ion batteries, Journal of Power Sources 147 (1) (2005) 269–281.

[49] L. Yang, B. Ravdel, B. L. Lucht, Electrolyte Reactions with the Surface of High Voltage $LiNi_{0.5}Mn_{1.5}O_4$ Cathodes for Lithium-Ion Batteries, Electrochemical and Solid-State Letters 13 (8) (2010) A95–A97.

[50] M. Falk, Investigation of surface film formation on $LiNi_{0.5}Mn_{1.5}O_4$ cathodes in carbonate based liquid electrolytes using the secondary ion mass spectrometry, Ph.D. thesis, Justus-Liebig-Universität, Gießen (May 2014).

[51] J. Li, C. Ma, M. Chi, C. Liang, N. J. Dudney, Solid Electrolyte: the Key for High-Voltage Lithium Batteries, Advanced Energy Materials 5 (4) (2015) 1401408.

[52] K. Thai, E. Lee, Effects of Mechanical Strain on Ionic Conductivity in the Interface between LiPON and Ni-Mn Spinel, Journal of The Electrochemical Society 164 (4) (2017) A594–A599.

[53] A. Schlifke, Synthese und Charakterisierung ternaerer und Quarternaerer mesoporoeser Metalloxide, Diplomarbeit, Universität Hamburg, Hamburg (2010).

[54] M. Gellert, K. I. Gries, J. Zakel, A. Ott, S. Spannenberger, C. Yada, F. Rosciano, K. Volz, B. Roling, $LiNi_{0.5}Mn_{1.5}O_4$ Thin-Film Cathodes on Gold-Coated Stainless Steel Substrates: Formation of Interlayers and Electrochemical Properties, Electrochimica Acta 133 (2014) 146–152.

[55] J. Mosa, J. Vélez, J. Reinosa, M. Aparicio, A. Yamaguchi, K. Tadanaga, M. Tatsumisago, $Li_4Ti_5O_{12}$ thin-film electrodes by sol–gel for lithium-ion microbatteries, Journal of Power Sources 244 (2013) 482–487.

[56] J. Mosa, J. Vélez, I. Lorite, N. Arconada, M. Aparicio, Film-shaped sol–gel $Li_4Ti_5O_{12}$ electrode for lithium-ion microbatteries, Journal of Power Sources 205 (2012) 491–494.

[57] M. Hirayama, K. Kim, T. Toujigamori, W. Cho, R. Kanno, Epitaxial growth and electrochemical properties of $Li_4Ti_5O_{12}$ thin-film lithium battery anodes, Dalton Transactions 40 (12) (2011) 2882–2887.

[58] P. Schichtel, M. Geiß, T. Leichtweiß, J. Sann, D. A. Weber, J. Janek, On the impedance and phase transition of thin film all-solid-state batteries based on the $Li_4Ti_5O_{12}$ system, Journal of Power Sources 360 (2017) 593–604.

[59] V. Weber, T. Laino, A. Curioni, T. Eckl, C. Engel, J. Kasemchainan, N. Salingue, Computational Study of Lithium Titanate as a Possible Cathode Material for Solid-State Lithium–Sulfur Batteries, The Journal of Physical Chemistry C 119 (18) (2015) 9681–9691.

[60] S. Huang, Z. Wen, X. Zhu, Z. Lin, Effects of dopant on the electrochemical performance of $Li_4Ti_5O_{12}$ as electrode material for lithium ion batteries, Journal of Power Sources 165 (1) (2007) 408–412.

[61] S. Huang, Z. Wen, X. Zhu, Z. Gu, Preparation and electrochemical performance of Ag doped $Li_4Ti_5O_{12}$, Electrochemistry Communications 6 (11) (2004) 1093–1097.

[62] P. P. Prosini, R. Mancini, L. Petrucci, V. Contini, P. Villano, $Li_4Ti_5O_{12}$ as anode in all-solid-state, plastic, lithium-ion batteries for low-power applications, Solid State Ionics 144 (1–2) (2001) 185–192.

[63] I. A. Leonidov, O. N. Leonidova, L. A. Perelyaeva, R. F. Samigullina, S. A. Kovyazina, M. V. Patrakeev, Structure, ionic conduction, and phase transformations in lithium titanate $Li_4Ti_5O_{12}$, Physics of the Solid State 45 (11) (2003) 2183–2188.

[64] J. Wolfenstine, J. L. Allen, Electrical conductivity and charge compensation in Ta doped $Li_4Ti_5O_{12}$, Journal of Power Sources 180 (1) (2008) 582–585.

[65] J. Ma, P. Hu, G. Cui, L. Chen, Surface and Interface Issues in Spinel $LiNi_{0.5}Mn_{1.5}O_4$: Insights into a Potential Cathode Material for High Energy Density Lithium Ion Batteries, Chemistry of Materials 28 (11) (2016) 3578–3606.

[66] C. Y. Ouyang, Z. Y. Zhong, M. S. Lei, Ab initio studies of structural and electronic properties of Li4Ti5O12 spinel, Electrochemistry Communications 9 (5) (2007) 1107–1112.

[67] D. Liu, C. Ouyang, J. Shu, J. Jiang, Z. Wang, L. Chen, Theoretical study of cation doping effect on the electronic conductivity of $Li_4Ti_5O_{12}$, physica status solidi (b) 243 (8) (2006) 1835–1841.

[68] H. Liu, G. Wen, S. Bi, P. Gao, Enhanced rate performance of nanosized $Li_4Ti_5O_{12}$/graphene composites as anode material by a solid state-assembly method, Electrochimica Acta 171 (2015) 114–120.

[69] P.-E. Lippens, M. Womes, P. Kubiak, J.-C. Jumas, J. Olivier-Fourcade, Electronic structure of the spinel $Li_4Ti_5O_{12}$ studied by ab initio calculations and X-ray absorption spectroscopy, Solid State Sciences 6 (2) (2004) 161–166.

[70] P.-c. Tsai, W.-D. Hsu, S.-k. Lin, Atomistic Structure and Ab Initio Electrochemical Properties of $Li_4Ti_5O_{12}$ Defect Spinel for Li Ion Batteries, Journal of The Electrochemical Society 161 (3) (2014) A439–A444.

[71] K. Wu, J. Yang, X.-Y. Qiu, J.-M. Xu, Q.-Q. Zhang, J. Jin, Q.-C. Zhuang, Study of spinel $Li_4Ti_5O_{12}$ electrode reaction mechanism by electrochemical impedance spectroscopy, Electrochimica Acta 108 (2013) 841–851.

[72] P. Kubiak, A. Garcia, M. Womes, L. Aldon, J. Olivier-Fourcade, P.-E. Lippens, J.-C. Jumas, Phase transition in the spinel $Li_4Ti_5O_{12}$ induced by lithium insertion: Influence of the substitutions Ti/V, Ti/Mn, Ti/Fe, Journal of Power Sources 119–121 (2003) 626–630.

[73] W. Schmidt, P. Bottke, M. Sternad, P. Gollob, V. Hennige, M. Wilkening, Small Change—Great Effect: Steep Increase of Li Ion Dynamics in $Li_4Ti_5O_{12}$ at the Early Stages of Chemical Li Insertion, Chemistry of Materials.

[74] M. Kitta, T. Akita, S. Tanaka, M. Kohyama, Two-phase separation in a lithiated spinel $Li_4Ti_5O_{12}$ crystal as confirmed by electron energy-loss spectroscopy, Journal of Power Sources 257 (2014) 120–125.

[75] L. Guohua, H. Ikuta, T. Uchida, M. Wakihara, The Spinel Phases $LiM_yMn_{2-y}O_4$ (M = Co, Cr, Ni) as the Cathode for Rechargeable Lithium Batteries, Journal of The Electrochemical Society 143 (1) (1996) 178–182.

[76] R. Santhanam, B. Rambabu, Research progress in high voltage spinel $LiNi_{0.5}Mn_{1.5}O_4$ material, Journal of Power Sources 195 (17) (2010) 5442–5451.

[77] A. de Kock, M. H. Rossouw, L. A. de Picciotto, M. M. Thackeray, W. I. F. David, R. M. Ibberson, Defect spinels in the system Li_2O.yMnO2 (y>2.5): A neutron-diffraction study and electrochemical characterization of $Li_2Mn_4O_9$, Materials Research Bulletin 25 (5) (1990) 657–664.

[78] L. Z. Zhao, Y. W. Chen, G. R. Wang, Raman spectra study of orthorhombic $LiMnO_2$, Solid State Ionics 181 (31–32) (2010) 1399–1402.

[79] J. Fischer, K. Chang, J. Ye, S. Ulrich, C. Ziebert, D. Music, B. Hallstedt, H. J. Seifert, Structural transformation of sputtered o-$LiMnO_2$ thin-film cathodes induced by electrochemical cycling, Thin Solid Films 549 (2013) 263–267.

[80] J. Fischer, C. Adelhelm, T. Bergfeldt, K. Chang, C. Ziebert, H. Leiste, M. Stüber, S. Ulrich, D. Music, B. Hallstedt, H. J. Seifert, Development of thin film cathodes for lithium-ion batteries in the material system Li–Mn–O by r.f. magnetron sputtering, Thin Solid Films 528 (2013) 217–223.

[81] J.-H. Kim, S.-T. Myung, C. S. Yoon, S. G. Kang, Y.-K. Sun, Comparative Study of $LiNi_{0.5}Mn_{1.5}O_{4-\delta}$ and $LiNi_{0.5}Mn_{1.5}O_4$ Cathodes Having Two Crystallographic Structures: *Fd-3m* and $P4_{3}32$, Chemistry of Materials 16 (5) (2004) 906–914.

[82] L. Wang, H. Li, X. Huang, E. Baudrin, A comparative study of *Fd-3m* and $P4_{3}32$ “$LiNi_{0.5}Mn_{1.5}O_4$”, Solid State Ionics 193 (1) (2011) 32–38.

[83] X. Feng, C. Shen, X. Fang, C. Chen, Nonstoichiometric $Li_{1\acute{s}x}$ $Ni_{0.5}Mn_{1.5}O_4$ with different structures and electrochemical properties, Chinese Science Bulletin 57 (32) (2012) 4176–4180.

[84] K. Hoshina, K. Yoshima, M. Kotobuki, K. Kanamura, Fabrication of $LiNi_{0.5}Mn_{1.5}O_4$ thin film cathode by PVP sol–gel process and its application of all-solid-state lithium ion batteries using $Li_{1+x}Al_xTi_{2-x}(PO_4)_3$ solid electrolyte, Solid State Ionics 209–210 (2012) 30–35.

[85] L. Baggetto, R. R. Unocic, N. J. Dudney, G. M. Veith, Fabrication and characterization of Li–Mn–Ni–O sputtered thin film high voltage cathodes for Li-ion batteries, Journal of Power Sources 211 (2012) 108–118.

[86] L. Baggetto, N. J. Dudney, G. M. Veith, Surface chemistry of metal oxide coated lithium manganese nickel oxide thin film cathodes studied by XPS, Electrochimica Acta 90 (2013) 135–147.

[87] Y. Kim, N. J. Dudney, M. Chi, S. K. Martha, J. Nanda, G. M. Veith, C. Liang, A Perspective on Coatings to Stabilize High-Voltage Cathodes: $LiMn_{1.5}Ni_{0.5}O_4$ with Sub-Nanometer Lipon Cycled with $LiPF_6$ Electrolyte, Journal of The Electrochemical Society 160 (5) (2013) A3113–A3125.

[88] M. Mancini, P. Axmann, G. Gabrielli, M. Kinyanjui, U. Kaiser, M. Wohlfahrt-Mehrens, A High-Voltage and High-Capacity $Li_{1+x}Ni_{0.5}Mn_{1.5}O_4$ Cathode Material: From Synthesis to Full Lithium-Ion Cells, ChemSusChem 9 (14) (2016) 1843–1849.

[89] A. Lasia, Electrochemical Impedance Spectroscopy and its Applications, Springer, 2014, google-Books-ID: lWEgBAAAQBAJ.

[90] J. O. Bockris, A. K. N. Reddy, M. E. Gamboa-Aldeco, Modern Electrochemistry 2A: Fundamentals of Electrodics, Springer Science & Business Media, 2001, google-Books-ID: utDyTYpimkUC.

[91] V. F. Lvovich, Impedance Spectroscopy: Applications to Electrochemical and Dielectric Phenomena, John Wiley & Sons, 2015, google-Books-ID: FGFcCwAAQBAJ.

[92] E. Barsoukov, J. R. Macdonald, Impedance Spectroscopy: Theory, Experiment, and Applications, John Wiley & Sons, 2005, google-Books-ID: 8hNkOWO_DLwC.

[93] C. H. Hsu, F. Mansfeld, Technical Note: Concerning the Conversion of the Constant Phase Element Parameter Y_0 into a Capacitance, CORROSION 57 (9) (2001) 747–748.

[94] J. A. Mergos, C. T. Dervos, Structural and dielectric properties of Li_2O-doped TiO_2, Materials Characterization 60 (8) (2009) 848–857.

[95] K. Kim, T. Toujigamori, K. Suzuki, S. Taminato, K. Tamura, J. Mizuki, M. Hirayama, R. Kanno, Characterization of Nano-Sized Epitaxial $Li_4Ti_5O_{12}$(110) Film Electrode for Lithium Batteries, Electrochemistry 80 (10) (2012) 800–803.

[96] A. Kumatani, T. Ohsawa, R. Shimizu, Y. Takagi, S. Shiraki, T. Hitosugi, Growth processes of lithium titanate thin films deposited by using pulsed laser deposition, Applied Physics Letters 101 (12) (2012) 123103.

[97] A. V. Knyazev, N. N. Smirnova, M. Mączka, S. S. Knyazeva, I. A. Letyanina, Thermodynamic and spectroscopic properties of spinel with the formula $Li_{4/3}Ti_{5/3}O_4$, Thermochimica Acta 559 (2013) 40–45.

[98] L. Aldon, P. Kubiak, M. Womes, J. C. Jumas, J. Olivier-Fourcade, J. L. Tirado, J. I. Corredor, C. Pérez Vicente, Chemical and Electrochemical Li-Insertion into the $Li_4Ti_5O_{12}$ Spinel, Chemistry of Materials 16 (26) (2004) 5721–5725.

[99] W. C. Dunlap, R. L. Watters, Direct Measurement of the Dielectric Constants of Silicon and Germanium, Physical Review 92 (6) (1953) 1396–1397.

[100] D. R. Lide, CRC Handbook of Chemistry and Physics, 85th Edition, CRC Press, 2004, google-Books-ID: WDll8hA006AC.

[101] Y. Gao, Z. Wang, L. Chen, Workfunction, a new viewpoint to understand the electrolyte/electrode interface reaction, Journal of Materials Chemistry A 3 (46) (2015) 23420–23425.

[102] L. Le Van-Jodin, F. Ducroquet, F. Sabary, I. Chevalier, Dielectric properties, conductivity and Li+ ion motion in LiPON thin films, Solid State Ionics 253 (2013) 151–156.

[103] Z. Hu, D. Li, K. Xie, Influence of radio frequency power on structure and ionic conductivity of LiPON thin films, Bulletin of Materials Science 31 (4) (2008) 681–686.

[104] G. Li, M. Li, L. Dong, X. Li, D. Li, Low energy ion beam assisted deposition of controllable solid state electrolyte LiPON with increased mechanical properties and ionic conductivity, International Journal of Hydrogen Energy 39 (30) (2014) 17466–17472.

[105] Y. Su, J. Falgenhauer, A. Polity, T. Leichtweiß, A. Kronenberger, J. Obel, S. Zhou, D. Schlettwein, J. Janek, B. K. Meyer, LiPON thin films with high nitrogen content for application in lithium batteries and electrochromic devices prepared by RF magnetron sputtering, Solid State Ionics 282 (2015) 63–69.

[106] K. F. Chiu, C. C. Chen, K. M. Lin, H. C. Lin, C. C. Lo, W. H. Ho, C. S. Jiang, Modification of sputter deposited solid-state electrolyte thin films, Vacuum 84 (11) (2010) 1296–1301.

[107] K.-F. Chiu, C. C. Chen, K. M. Lin, C. C. Lo, H. C. Lin, W.-H. Ho, C. S. Jiang, Lithium phosphorus oxynitride solid-state thin-film electrolyte deposited and modified by bias sputtering and low temperature annealing, Journal of Vacuum Science & Technology A 28 (4) (2010) 568–572.

[108] S. Jacke, J. Song, L. Dimesso, J. Brötz, D. Becker, W. Jaegermann, Temperature dependent phosphorous oxynitride growth for all-solid-state batteries, Journal of Power Sources 196 (16) (2011) 6911–6914.

[109] M. Ganesan, M. V. T. Dhananjeyan, K. B. Sarangapani, N. G. Renganathan, Solid state rapid quenching method to synthesize micron size $Li_4Ti_5O_{12}$, Journal of Electroceramics 18 (3-4) (2007) 329–337.

[110] M. Ganesan, $Li_4Ti_{2.5}Cr_{2.5}O_{12}$ as anode material for lithium battery, Ionics 14 (5) (2007) 395–401.

[111] S. Wenzel, S. Randau, T. Leichtweiß, D. A. Weber, J. Sann, W. G. Zeier, J. Janek, Direct Observation of the Interfacial Instability of the Fast Ionic Conductor $Li_{10}GeP_2S_{12}$ at the Lithium Metal Anode, Chemistry of Materials 28 (7) (2016) 2400–2407.

[112] S. Wenzel, D. A. Weber, T. Leichtweiss, M. R. Busche, J. Sann, J. Janek, Interphase formation and degradation of charge transfer kinetics between a lithium metal anode and highly crystalline $Li_7P_3S_{11}$ solid electrolyte, Solid State Ionics 286 (2016) 24–33.

[113] A. Kulshreshtha, P. Singh, K. K. Sarkar, Applications of the ion-dependent quantum dielectric model for binary solids, Physical Review B 25 (12) (1982) 7852–7855.

[114] U. v. Alpen, A. Rabenau, G. H. Talat, Ionic conductivity in Li_3N single crystals, Applied Physics Letters 30 (12) (1977) 621–623.

[115] T. Lapp, S. Skaarup, A. Hooper, Ionic conductivity of pure and doped Li_3N, Solid State Ionics 11 (2) (1983) 97–103.

[116] W. Li, G. Wu, C. M. Araújo, R. H. Scheicher, A. Blomqvist, R. Ahuja, Z. Xiong, Y. Feng, P. Chen, Li+ ion conductivity and diffusion mechanism in α-Li_3N and β-Li_3N, Energy & Environmental Science 3 (10) (2010) 1524–1530.

[117] J. Wahl, U. Holland, Local ionic motion in the superionic conductor Li_3N, Solid State Communications 27 (3) (1978) 237–241.

[118] G. Nazri, Preparation, structure and ionic conductivity of lithium phosphide, Solid State Ionics 34 (1) (1989) 97–102.

[119] R. M. Biefeld, R. T. Johnson, Ionic Conductivity of Li_2O - Based Mixed Oxides and the Effects of Moisture and LiOH on Their Electrical and Structural Properties, Journal of The Electrochemical Society 126 (1) (1979) 1–6.

[120] W. Schnick, J. Luecke, Lithium ion conductivity of $LiPN_2$ and Li_7PN_4, Solid State Ionics 38 (3) (1990) 271–273.

[121] Y. Zhu, X. He, Y. Mo, Strategies Based on Nitride Materials Chemistry to Stabilize Li Metal Anode, Advanced Science (2017) 1600517.

[122] R. F. Pierret, Advanced Semiconductor Fundamentals, Prentice Hall, 2003, google-Books-ID: d2hrQgAACAAJ.

[123] F. J. Morin, J. P. Maita, Electrical Properties of Silicon Containing Arsenic and Boron, Physical Review 96 (1) (1954) 28–35.

[124] J. M. Cherlow, R. L. Aggarwal, B. Lax, Raman Scattering and Photoluminescence in Boron-Doped and Arsenic-Doped Silicon, Physical Review B 7 (10) (1973) 4547–4560.

[125] M. Wilkening, W. Iwaniak, J. Heine, V. Epp, A. Kleinert, M. Behrens, G. Nuspl, W. Bensch, P. Heitjans, Microscopic Li self-diffusion parameters in the lithiated anode material $Li_{4+x}Ti_5O_{12}$ (0 <= x <= 3) measured by ^{7}Li solid state NMR, Physical Chemistry Chemical Physics 9 (47) (2007) 6199–6202.

[126] M. Wilkening, R. Amade, W. Iwaniak, P. Heitjans, Ultraslow Li diffusion in spinel-type structured $Li_4Ti_5O_{12}$ — A comparison of results from solid state NMR and impedance spectroscopy, Physical Chemistry Chemical Physics 9 (10) (2007) 1239–1246.

[127] H. Hain, M. Scheuermann, R. Heinzmann, L. Wünsche, H. Hahn, S. Indris, Study of Local Structure and Li Dynamics in $Li_{4+x}Ti_5O_{12}$ (0<= x <=5) Using ^{6}Li and ^{7}Li NMR Spectroscopy, Zeitschrift für anorganische und allgemeine Chemie 638 (10) (2012) 1581–1581.

[128] B. Ziebarth, M. Klinsmann, T. Eckl, C. Elsässer, Lithium diffusion in the spinel phase $Li_4Ti_5O_{12}$ and in the rocksalt phase $Li_7Ti_5O_{12}$ of lithium titanate from first principles, Physical Review B 89 (17) (2014) 174301.

[129] Y. C. Chen, C. Y. Ouyang, L. J. Song, Z. L. Sun, Lithium ion diffusion in $Li_{4+x}Ti_5O_{12}$: From ab initio studies, Electrochimica Acta 56 (17) (2011) 6084–6088.

[130] Y. Wang, G. Yang, Q. Peng, P. X. Lu, Excellent Electrochemical Performance and Thermal Stability of $LiNi_{0.5}Mn_{1.5}O_4$ Thin-Film Cathode Prepared by Pulsed Laser Deposition, Advanced Materials Research 853 (2013) 83–89.

[131] Y. Wang, G. Yang, Z. Yang, L. Zhang, M. Fu, H. Long, Z. Li, Y. Huang, P. Lu, High power and capacity of $LiNi_{0.5}Mn_{1.5}O_4$ thin films cathodes prepared by pulsed laser deposition, Electrochimica Acta 102 (2013) 416–422.

[132] J. Yang, X. Zhang, Z. Zhu, F. Cheng, J. Chen, Ordered spinel $LiNi_{0.5}Mn_{1.5}O_4$ nanorods for high-rate lithium-ion batteries, Journal of Electroanalytical Chemistry 688 (2013) 113–117.

[133] C. M. Julien, F. Gendron, A. Amdouni, M. Massot, Lattice vibrations of materials for lithium rechargeable batteries. VI: Ordered spinels, Materials Science and Engineering: B 130 (1–3) (2006) 41–48.

[134] M. G. Lazarraga, L. Pascual, H. Gadjov, D. Kovacheva, K. Petrov, J. M. Amarilla, R. M. Rojas, M. A. Martin-Luengo, J. M. Rojo, Nanosize $LiNi_{textity}Mn_{2-y}O_4$ (0 < y <= 0.5) spinels synthesized by a sucrose -aided combustion method. Characterization and electrochemical performance, Journal of Materials Chemistry 14 (10) (2004) 1640–1647.

[135] J. Pröll, P. G. Weidler, R. Kohler, A. Mangang, S. Heißler, H. J. Seifert, W. Pfleging, Comparative studies of laser annealing technique and furnace annealing by X-ray diffraction and Raman analysis of lithium manganese oxide thin films for lithium-ion batteries, Thin Solid Films 531 (2013) 160–171.

[136] L. Porz, T. Swamy, B. W. Sheldon, D. Rettenwander, T. Frömling, H. L. Thaman, S. Berendts, R. Uecker, W. C. Carter, Y.-M. Chiang, Mechanism of Lithium Metal Penetration through Inorganic Solid Electrolytes, Advanced Energy Materials (2017) 1701003.